2019-01-01

Mineral Exploration Investigation In The Northern Sierra Madre Occidental, Mexico

Labdan Nijr Alqahtani
University of Texas at El Paso

MINERAL EXPLORATION INVESTIGATION IN THE NORTHERN

SIERRA MADRE OCCIDENTAL, MEXICO

LABDAN ALQAHTANI

Doctoral Program in Geological Science

APPROVED:

Philip Goodell, Ph.D., Chair

Jose Hurtado, Ph.D.

AlDouri Raed, Ph.D.

Jason Ricketts, Ph.D.

Benjamin Brunner, Ph.D.

Stephen L. Crites, Jr., Ph.D.
Dean of the Graduate School

MINERAL EXPLORATION INVESTIGATION IN THE NORTHERN SIERRA MADRE OCCIDENTAL, MEXICO

by

LABDAN NIJR ALQAHTANI, MS

DISSERTATION

Presented to the Faculty of the Graduate School of

The University of Texas at El Paso

in Partial Fulfillment

of the Requirements

for the Degree of

DOCTOR OF PHILOSOPHY

Department of Geological Sciences

THE UNIVERSITY OF TEXAS AT EL PASO

December 2019

ACKNOWLEDGEMENTS

First, I would like to thank the member of my dissertation committee: Dr. Philip C. Goodell, Dr. Jose Hurtado, Dr. Jason Ricketts, Dr. Raed Aldouri, and Dr. Benjamin Brunner. Their helpful comments, suggestion and attitude have made this final product a much better research study.

I especially thank Dr. Goodell for his teaching, valid assessment of the scientific material presented in this work, and constructive comments. Dr. Goodell devoted a great deal of his personal time in order to help me focus entirely on my work in the last four years.

I want to thank the government of Saudi Arabia via the King Abdullah Scholarship Program for supporting me during the four years, I needed to complete this academic program and for financing this research project.

Lastly and most importantly, I would like to thank my parents, my wife, my brothers, and my sisters for their endless support and constant encouragement, has had great importance in the production of this dissertation.

TABLE OF CONTENTS

LIST OF TABLES

LIST OF FIGURES

CHAPTER 1: EXPLORATION POTENTIAL IN THE SIERRA MADRE OCCIDENTAL, CHIHUAHUA, MEXICO RESULTING FROM APPLICATION OF REMOTE SENSING AND GIS TO GOLD AND SILVER HOSTED STRUCTURES

ABSTRACT

The Sierra Madre region is rich in mineralized deposits, but it is hard to access because of the rugged terrain. Remote sensing and GIS can help in mineral exploration and regional structural analysis. The purpose of this project is to study linear, curvilinear, arcuate, and circular features in the Sierra Madre Occidental of Mexico in order to improve exploration possibility. It is of great interest to know the relationship between lineament intersections, caldera features because of the location of potential mineral occurrences. In this study, 4,445 lineaments were mapped manually using directional filters applied to satellite images. A total of 26,031 lineaments were extracted automatically with the line module of PCI Geomatica based on automatic detection algorithms (canny algorithms). The remote sensing analysis successfully identified 34 first-order lineaments (FOL) with lengths > 15 km. The FOL help to identify horsts, grabens, and strike-slip faults. The contrast in results between FOL and third-order (TOL) (less than 3 km) is interpreted to represent predominately early versus late tectonic events. The remote sensing analysis identified 17 new previously unknown calderas. Mineral occurrences and mines are generally but not exclusively associated with caldera rims and internal fractures and faults. A positive correlation exists between FOL and mineral occurrences. These results can be useful for future mineral exploration.

1. INTRODUCTION

Trends of regional mineralization are controlled by structural lineaments (Sellepack and Goodell, 1996; Goodell et al.1997; Chernicoff et al., 2002; Abdullah et al. 2013). Identifying these lineaments is a part of the establishment metallogenic belts, their geologic history, and the discovery of exploration targets. Lineament analysis is the study of lineaments and linear patterns, including their geometry, kinematics, and dynamics. It is applied to mineral exploration to define the most favorable locations for mineral concentrations associated with tectonic environments (Katz, 1982).

The development of the airplane provided aerial photographs to geologists, and, similarly, earth orbiting satellites provided a different scale from which to view the earth, and a flurry of satellite mapping took place and continues. Lineaments became a crucial component of regional exploration for some companies, particularly as new parts of the world became accessible to exploration. Many mineral deposits were realized to occur nearby lineament intersections and lineament analysis has been valued by some researchers (e.g., Mayo, 1958; Heyl, 1972; Marshall, 1979; O' Driscoll 1981; Acharya et al., 2007; Abdullah et al., 2013) but has been questioned by others (e.g., Guilluly 1976; Kutina, 1980). Repeated lineaments patterns in rocks of every age suggest that some lineaments are manifestations of deep crustal features (Podwysocki and Earle, 1976).

2. OBJECTIVES

The aim of this study is to do a regional structural analysis of linear, curvilinear, arcuate, and circular features in the study area (Figure 1). Independent data exists that shows the locations of mines and mineral occurrences in the region. It is interesting to know the relationship between lineament intersections, caldera features, and the location of potential mineral occurrences. This knowledge will guide future mineral exploration.

3. STUDY AREA

The study area is located in the northern part of the Sierra Madre Occidental about 125 km west of Chihuahua City, Chihuahua, Mexico and 400 km southwest of El Paso, Texas (Figure 1). The study area extends 270 km from north to south and 164 km from east to west edge, covering an area of 44,116 km2. The area was chosen because of the potential mineralization and it is an isolated area where remote sensing is most effective.

4. BACKGROUND

In western North America, tectonism and volcanism during the late Cretaceous to early Cenozoic are associated with subduction of the Farallon plate which led to the opening of the Gulf of California and initiation of the Baja rift (McDowell and Clabaugh, 1979; Atwater, 1988; Aguirre-Dıaz and McDowell, 1991; Aguirre-Dıaz and Labarthe-Hernandez, 2003; Swanson et al., 2006). It was during this time that the Sierra Madre Occidental (SMO) was formed.

The SMO is considered one of the largest siliceous igneous provinces (SLIP) in the world (Bryan et al., 2008; Cather et al., 2009; Jicha et al., 2009). It spans an area from just south of the border between Arizona, USA and Sonora, Mexico, to the area of Guadalajara, in west-central Mexico, 1,800 km to the south. The SMO varies in elevation from 200 m above sea level (asl) to a maximum of about 3,000 m asl. The core of the SMO is reported to be relatively unextended in comparison to the surrounding Late Oligocene to Miocene extensional belts of the southern Basin and Range to the east and the Gulf of California extensional province to the west (Nieto-Samaniego et al., 1999; Henry and Aranda-Gómez, 2000) (Figure 2).

The SMO is composed of volcanic rocks which overly a Precambrian through Jurassic age basement complex. It is one of the significant accumulations of unmetamorphosed andesite and dacite in the world. It is also one of the essential metallogenic

provinces of gold- and silver-bearing epithermal deposits in Mexico (Clark et al., 1982; Ferrari et al., 2007; Bryan et al., 2008; Cather et al., 2009; Jicha et al., 2009; Murray et al. 2013).

4.1. Geology

The older Lower Volcanic Series (LVS) and the younger Upper Volcanic Series (UVS) are the rock units which constitute most of the surface of the SMO, although a few small windows exist showing older rocks (Mc Dowell and Clabaugh, 1979).

The LVS is an andesitic suite of rocks formed above a subduction zone during the Laramide, (Ferrari et al., 2000). In the study area, the Laramide had two regional pulses of ages the first at 80 Ma, and the second at 60-45 Ma (Aguirre-Díaz and McDowell, 1991; Ferrari et al., 2007).

The UVS comprises rhyolitic ash-flow tuffs issued from large calderas. They were emplaced during two pulses, one in the Oligocene (ca. 32-28 Ma) and the other in the Early Miocene (ca. 24–20 Ma) (Ferrari et al., 2007). The UVS was associated with lateral faulting and regional extension (McDowell and Keizer, 1977; McDowell and Clabaugh, 1979; Aguirre- Díaz and McDowell, 1991, 1993; Staude and Barton, 2001; Ferrari et al., 2002, 2007).

Ten calderas have previously been found in this area and during these investigations in the SMO, a new variant of a caldera has been described, a caldera graben (Aguirre-Diaz et al., 2008). The transition from compression to extension is controversial. The 'ignimbrite flare-up' appears to be the earliest part of post-transition volcanism.

4.2. Mineralization

Mineralization is superimposed on the rocks of the SMO as (1) Laramide-aged porphyry Cu, Cu-Au, and Cu-Mo in the LVS; (2) skarns associated with the Laramide porphyry episode; and (3) epithermal precious metal deposits associated with lateral and

listric faults hosted in both the LVS and UVS. The epithermal deposits, known collectively as the Northern Sierra Madre Precious Metal Belt (NSMPMB) (Wisser, 1966; Clark et al., 1982), constitute one of the larger precious metal mineral belts of the world. Mineralization ages in the NSMPMG range from Eocene to Oligocene (Clark et al., 1982; Staude, 1995; Sellepack, 1997; Staude and Barton, 2001; Camprubí et al., 2003). Two discrete periods of mineralization are proposed (Ferrari et al., 2002, 2007).

The older period is related to the magmatic event that originated the LVC during compressional regime. The younger period is related to formation of the UVS during the Oligocene and Early Miocene (Ferrari et al., 2002, 2007).

5. DATA

Four different types of data are used in this project (Table 1).

5.1. Landsat 8

Four Landsat 8 scenes (LC08_L1TP_033041_20130606_20170310_01_T1), (LC08_L1TP_033040_20130606_20170310_01_T1), (LC08_L1TP_034040_20130528_20180131_01_T1) and (LC08_L1TP_034041_20131222_20170308_01_T1) were required to cover the entire study area (Figure1).They downloaded from the United States Geological Survey (USGS) website (http://glovis.usgs.gov/).

5.2. SRTM 1 Arc-Second Global

Digital Elevation model data offer worldwide coverage of void filled data at a resolution of 1 arc-second (30 meters) and provide open distribution of this high-resolution global data set. The DEM data were obtained from the USGS Earth Explorer website. (http://earthexplorer.usgs.gov/)

5.3. Mineral Resources Data System (MRDS)

MRDS (https://mrdata.usgs.gov/mrds/) shapefile compiles data from reports describing metallic and nonmetallic mineral resources throughout the world (Figure 3).

5.4. The Major Gold/Silver Systems (Mines) in the study area

A summary of the geological characteristics of 10 deposits is presented here. The data is taken from Manriques (2005) or the company websites (Table 5 and Figure 3).

5.4.1. Dolores

Dolores is a gold-silver mine which covers an area of 4.8 km². It is a low-sulfidation system .The northwest trending structural grain in Dolores is a zone of anastomosing faults in which latitic intrusions and mineralization were emplaced. Overbay et al. (2001) place Dolores within a 100-km diameter elliptical feature they interpret to be a caldera. However, the work presented here is in disagreement with Overbay et al. (2001) since no caldera of this size was found in this location.

5.4.2. Mulatos

The Mulatos district covers an area of 400 km² in which several dacitic to rhyodacitic domes and coeval high sulphidation type mineralization is found (Palmer, 1883; Wisser, 1966; Clark et al., 1982).

5.4.3. Pinos Altos

The Pinos Altos district covers an area of 30 km² including numerous veins with Au ± Ag mineralization. The mine is situated within regional west-northwest trending lineaments. The Pinos Altos district is located at the northeastern margin of a subcircular feature, which Bockoven (1980) proposed to be a caldera. Ocampo by Swanson and McDowell (1984) refer to it as the Ocampo caldera (see below). However, it is possible that the arcuate lineament defining the rim could instead be caused by series of liner structures having slightly different strike direction.

5.4.4. Ocampo

The Ocampo district is a low-sulfidation system made up of several Ag-Au veins and stock-works covering an area of about 24 km². The Ocampo district is located at the center of the Ocampo caldera proposed by Bockoven (1980). The local structures are dominated by two principal trends described by Byington and Bybee (2000). One consists of northwest-trending faults, and another of a west-northwest coeval system; the latter is the NE which contains chiefly of north-trending structures intersected by NW-trending faults.

5.4.5. Los Jarros

Los Jarros is located on the southeast margin of the Ocampo caldera. North-northwest-trending faults are the most common in the area, but an east-northeast-trending fault system paralleling the horst is also important.

5.4.6. Palmarejo

Based on satellite imagery, Laurent (2004) suggested that Palmarejo is situated on the south-western flank of a small caldera. Locally, the structural pattern is dominated by northwest- and west-northwest-trending faults. According to Corbett (2004), the west-northwest-striking faults may have become dilated and mineralized during strike-slip movement. This north-northwest system shows later reactivation and some related north-trending splays (Beckton, 2004). Work in progress interprets a large caldera — graben, a nested caldera, and a smaller caldera within it (Goodell et. al.).

5.4.7. Cerro Colorado

Cerro Colorado is within a zone dominated by ENE lineaments which could represent strike-slip faults (Galván, 2005). No active mine is present here.

5.4.8. Satevo

The town occupies what was along gossan formed over a porphery Cu-Au deposit. Artisanal mining of gold from quartz veins takes place in the river. The polymetallic veins

marginal to this suspected porphyry system are described. Satevo is located in the west-central part of a large circular feature, approximately 42 km in diameter (Islas and Gastélum, 1988; Querol and Mendoza, 1996) which contains several epithermal and porphyry-type alteration systems and minor circular structures associated with northwest-trending lineaments. Satevo has been proposed to be located on the northern margin of the Cuenca de Oro pull-apart basin (L14) (Feinstein, 2007). No active mine is present here.

5.4.9. El Sauzal

El Sauzal is located at the intersection of L11, L13, L14, and L15 (Figure 5) at the northern margin of a pull-apart basin called Cuenca de Oro (Goodell and Sellepack, 1996; Goodell et al., 1997; Feinstein, 2007). Two billion dollars worth of gold was extracted between 1997 and 2015 (Gold corp.).

5.4.10. Batopilas

This district is located in southwestern Chihuahua. The native silver in calcite mineralization and age are anomalous (Wilkerson et al., 1988). The porphyry copper deposits (Corralitos, Tres Hermanos, and Satevo) are within Batopilas district. Batopilas was discovered in 1632 and has had many operating mines, but none are operating today (Gonzales, 1956). The Batopilas lineament strikes north-south and extends 66 km (Galván, 2005).

6. PROCESSING AND METHOD

ArcMap, ENVI, PCI Geomatica, and RockWorks 16 are the software packages which were used in this project. All images were projected into the WGS 84 UTM zone 12N projection.

The following workflow was performed:

1. Visual extraction of lineaments: Lineaments were observed and manually digitized from the Landsat 8 imagery using directional filters to enhance the edge of the image.

This was done with ENVI software. For each input Landsat scene, four image products were derived from the application of directional filters (N-S, E-W, NE-SW, and NW-SE) (Sedrette and Rebaï, 2016). These filters increase contrast in the image and allow the mapping of more lineaments in ArcGIS 10.5.1 (Figure 4).

2. Automatic extraction of lineaments: Various computer-aided methods exist for lineament extraction using contrast detection algorithms (Abdullah et al., 2010). The LINE module of PCI Geomatica Version 8.2 was performed to automatically extract lineaments. The software records the polylines in vector segments by using six parameters (RADI, GTHR, LTHR, FTHR, ATHR and DTHR) (Sedrette and Rebaï., 2016).
3. Density analysis: Density analysis mapping was applied to the map of automatically extracted lineaments using the Spatial Analyst tool in ArcGIS 10.5.1. The purpose of the lineament density analysis is to calculate the frequency of lineaments per unit area (Greenbaum, 1985; Zakir et al., 1999). Then a map showing concentrations of the lineaments around each grid cell within the study area was created.
4. Orientation analysis: RockWorks16 Software was used to show the azimuthal data for (Rose diagrams) both the manually-extracted and the automatically-extracted lineaments (Karnieli et al., 1996).
5. Topographic analysis: DEM was used in ArcGIS to make elevation profiles to show the topographic changes of calderas boundaries and series of horst and graben.

7. RESULTS

7.1. Visual Extraction of Lineaments

A total of 4,445 lineaments were mapped with the manual method. They are subdivided into first order (greater than 15 km), second order (from 14 to 3 km), and third order (less than 3 km) (Galvan, 2005) (Figure 5).

7.1.1. First Order Lineaments (FOL)

There are 34 FOL in the area of interest (Figure 1). Their lengths range from 15 km to 87 km (Table 2; Figure 6A). The area of interest is further subdivided into north, central, and south sections, and these will be discussed separately below. The result of the rose diagrams suggests that the main trends of the lineaments are 330-340, 350-360, and, less frequently, 040-050 (Figure 6B).

In the northern region, lineaments L1, L2, L3, L4, and L18 all strike northwest. L5 strikes east-west and intersects L2 at southern end of L2. In the center region, L6 is tangent to the western border of the Ocampo caldera. L7 has a northeast strike, which is parallel to the Otero River, which itself is tangent to the Palmarejo caldera (S2). In the southern region, L8 has a southeast strike that is parallel to the Chinipas River.

An area of particular importance in the southern region is the triangle defined by L11, the Urique Lineament, L12, and L13. A rhombic shape called the Cuenca de Oro (Feinstein, 2007) is also present in the southern region, which is defined by L14 in the north, L15 in the west, L16 (the Sinforosa lineament) in the south, and L17 in the east (Figure 6A). The Sinforosa lineament extends over 100 km southeast and is occupied by Sinforosa River within a canyon nearly 1,000 meters deep.

7.1.2. Second Order Lineaments (SOL)

The SOL (14 to 3 km in length) consists of 337 lineaments (Figure 7A). The mean direction of the SOL is 300 - 310 and less frequently 040-060 (Figure 7B).

7.1.3. Third Order Lineaments (TOL)

TOL lineaments are those that are less than 3 km in length. There are 4,073 TOL lineaments (Figure 8A). Seventy percent of this group strikes northeast. The mean direction is 060-080, with a less frequent 300-310 trend (Figure 8B).

7.2. Automatic Extraction of Lineaments

A total of 26,031 lineaments were automatically extracted from the Landsat 8 image (Figure 9A). More than 70% of the population of the automatically-extracted lineaments strikes northeast. The mean direction is 040-070, with a less frequent 270–280 trend (Figure 9B). The density map (Figure 10) shows that automatically-extracted lineaments are highly concentrated in the southeast, the northwest, and the west, with decreases in density in the northeast and southwest regions.

7.3. Circles and Arcs

7.3.1. Known Calderas

In the area of interest there are 10 reported calderas that have been identified by previous workers by preliminary field mapping (Swanson and McDowell, 1984; Wark et al., 1990; Ferrari et al., 2007; Murry et al., 2013) (Table 3; Figure 11). Several of these calderas are known only from remote sensing observations. In the north region of the study area, the Corralitos caldera (Co) is present between two large lineaments, L3 and L4, which strike northwest and are tangent to the northeast and southwest rims of the calderea. Las Varas caldera (V) is 12.5 km in diameter, and it is located inside one of the biggest potential calderas discovered in this study North 3(N3).

N3 has a tangent lineament on the northeast border. Ocampo caldera (O) is the biggest caldera in the study area, and it contains several mines, including Ocampo, Pinos Altos, and Moris. The Ocampo caldera shares a tangent lineament, L5, with the Tómochic caldera (To) to the east. El Comanche (C), Manzanita (Ma), and San Juanito (SJ) calderas have shared boundaries. These calderas are in a cluster along with the Tómochic caldera to the north and the C7 potential caldera (see below) to the south (Figure 12). In the center part of the study area is the Copper Canyon caldera (CC) that is crossed by the L10 lineament. Center Known caldera (CK) has a tangent lineament on its southern border (Figure 13). In the southern part

of the study area, South Known caldera (SK) has several tilted blocks between parallel fractures (Figure 14).

7.3.2. New Potential Calderas

The Landsat 8 satellite image and the DEM of the study area are used to identify specific geological characteristics related to caldera structures, including caldera rims and floors, ring faults, circular or elliptical shapes, domal features, radial fractures, and tangents. Several techniques are used to map potential calderas. Sometimes, the caldera rim is not evident, changing the magnification in both images been investigation the Landsat image and the base map of ArcMap that can give a better visual result to find the rim of the caldera.

A total of seventeen previously-unknown, potential calderas have been found (Table 4), varying in size from large (46 km), to small (7.5 km) varying in diameter size.

In the northern region, there are four calderas (Figure 12): North 1 (N1), North 2 (N2), North 3 (N3), and North 4 (N4). N1, in the far northwest, is one of the smallest potential calderas 8.5 Km. N2 has a tangent lineament (L2) on its western border and has a coincident border with N3 to the south. N3 is the largest new potential caldera 46 Km. It has two NW striking tangent lineaments, L2 along the western rim and L3 along the eastern rim. The center of L2 is also cut by prominent northwest-trending lineaments. N4 caldera is located west of the Chihuahua-Sonora border and west of N3. It has three tangents, L2 on the east, L6 on the southwest, and L18 on the west (Figure 12).

In the center region, six potential calderas are identified (Figure 13): Center 1 (C1) to Center 7 (C7). C1 lies on the Chihuahua-Sonora border and is one of the smallest calderas, with a diameter of 9 km. C2 is located in close to the western edge of the study area. It is cut by two, long, north-south striking, radial fractures. C3 has a tangent lineament, L6, on its eastern border. C4 and C5 are small potential calderas which have radial fractures inside and outside their borders. C6 could be part of the cluster of calderas with C4 and C5. C7 has

radial fractures inside, outside, and across its rim. It belongs to a cluster of previously-known calderas in the north (C, Ma, SJ, and To) (Figure 13).

In the southern region, six potential calderas are identified (Figure 14): South 1 (S1) to South (S6). S2 has two tangent lineaments, L7 on the northwest rim and L9 on the west rim. S2 is crosscut by lineament L8. S3 and S4 are having a common border, and they are both inside S2 caldera. Lineament L10 is tangent to the northwest rim of S5, and lineament L11 is tangent to the west rim of S5. Lastly, S6 is a large circular potential caldera with a diameter of 32 km (Figure 14).

7.4. Result of Mineral Resources Data System (MRDS)

One hundred and eighty prospects and mines with data from the MRDS are in the area of interest. They are located in three states, 157 in Chihuahua, 20 in Sonora, and 3 in Sinaloa (Figure 3). All the locations are gold and silver mines or prospects which are often associated with copper, zinc, lead, molybdenum, antimony, iron, manganese, and tungsten. To examine how accurate these data are, we compared the location point of the USGS shape file data with the known mine location (SEDAR). The distance between the USGS location and the known location is a measure of quality control of the USGS data (Table 4). The results show that the USGS data is located on the mines or close by, less than1.5 km distance as measure here.

8. DISCUSSION

8.1. Lineaments

FOL lineaments are generally oriented NNW-SSE which follows the dominant structural grain in the northern of Sierra Madre Occidental (King, 1939; Wisser, 1966; Stock and Hodges, 1989; Horner and Enríquez, 1999; Staude, 1993a; Lee et al., 1996; Staude and Barton., 2001) (Figure 6A). TOL and the automatically-extracted lineaments both strike NNE which can be related to late extension in the Sierra Madre Occidental (Bagby, 1979; Cameron et al., 1989; Wark et al., 1990; González León et al., 2000, Swanson et al., 2006; McDowell.,

2007; Ferrari et al., 2007, Bryan et al., 2008). The rose diagram of the TOL is similar to that of the automatically-extracted lineaments (Figure 7B and Figure 8B). However, automatic lineaments extraction will include roads, but manually extraction chooses to avoid them (El-Sawy et al., 2016). However, the automatic lineament only accepts lineaments less than 3 km (Figure 8A). The FOL in the northern region strike NW-SE (L1, L2, L3, and L4) might be the boundaries of grabens (narrow and deep), and the horsts (wide and high elevations). The elevation profile shows progressively decreasing elevation from east to west (Figure15). The southeast region, where L14, L15, L16, and L17 are present, is the Cuenca de Oro pull part basin in southwestern Chihuahua (Sellepack, 1997; Goodell, 1995; McDonough, 2005; Feinstein, 2007) (Figure 16D).

L 16 is the Sinforosa lineament which has a length of over 100 km. It may be a terrane boundary or a strike-slip fault (McDonough, 2004; Feinstein, 2007) (Figure 16D). In the northeast and southeast portion of the Palmarejo Caldera (S2), there are curvilinear features outside the caldera boundary which are tilted in similar fashion. These are interpreted to result from extension adjacent to a large strike-skip fault (Figures 16A and 16B). These may be accommodation or transfer zones (Faulds and Stewart, 1998), which are the adjustments of surficial material to extensional regimes, and different behaviors, are illustrated abundantly. The fracture density map (Figure 10) can help to identify fractures zones in the area of study (Figure 1).

8.2. Circles

Seventeen new potential calderas are described in this project (Figure 10; Table 3). These potential calderas could be part of the estimated to exist 200 to 400 calderas (Steven and Lipman., 1976; McDowell and Clabaugh., 1979; Aguirre- Díaz, et al., 2003).

N3 is described here as a resurgent caldera. The northwest trending family of fractures is in the center of the caldera and interpreted to be associated with resurgent

doming. The shape of the caldera is a circle, similar to the 1.25 Ma Valles caldera (Smith and Bailey, 1968; Phillips, 2004) (Figure 12).

8.3. Tangents

Tangents are important structural features. Tangents are important in connecting structural elements and have significant properties themselves. They may connect other lineaments or calderas, and they may be portions of grabens.

8.4 Mineral Occurrences

The mineral occurrences in this region have good relations with FOL and SOL; however, it shows the opposite with TOL (Figure 5). Minerals occurrences can be found at or near the intersections between lineaments in this region. Examples include the intersection between L2 and L5 and the triangle formed by L11, L12, and L13 (Figure 16C). Additionally, mineral occurrences appear on lineaments such as L2 and L6 (Figure 6A). There are several prospects and mines inside the pull-part basin between L14, L15, L16, and L17 (King, 1939; Wisser, 1966; Clark et al., 1988; Wilkerson et al., 1988; Goodell, 1995; Smith et al., 1996; Sellepack, 1997; McDonough, 2005; Galvan, 2005; Figure 16D).

Mineralization can be found inside calderas (N3, C3, S1, S2, S3, and S6). Mineral occurrences or mines are also present near the boundaries of numerous other potential calderas (N2, N3, N4, C1, C3, S1, S2, S3, S4, S5, and S6) (Swanson and McDowell, 1984; Wark et al., 1990). On the other hand, there are some potential calderas which have no relation with mineral occurrences (N1, C2, C4, C5, and C6) (Figure 17; Table 7). The northeastern part of the study area shows no mineral occurrence or mines (Figure 17).

All of the major mineral deposits (Figure 17) have structural features associated with the mineralization. The Dolores, Pinos Altos, Ocampo, Los Jarros, and Palmarejo mines are associated with northwest-trending lineaments. Some of mineral deposits are present on both north-northwest-trending lineaments and calderas, e.g., Palmarejo, Pinos Altos, and Ocampo.

Mineral deposits can be associated with both east-northeast- and north-northwest-trending lineaments, e.g., Los Jarros. El Sauzal occurs at the intersection between several lineaments (L11, L13, L14, and L15). Lastly, mineralization can occur when there is a fractured zone such as at Satevo. This result can support our findings for the lineaments and circles that were mentioned in the previous results.

9. CONCLUSION

This study demonstrates an efficient way for extracting and analyzing geological features over a large (270 km ×165 km), rugged (200 m to 2000 m elevation), remote area. Based on Figure 4, the area affected by the extension which means that the results do not agree with idea of the core of SMO is relatively not extended (Figure 2). Remote sensing has successfully helped to identify 17 previously-unknown calderas and verify 10 previously-known ones, although the results call into question one previously documented caldera (SK). Remote sensing has successfully identified 34 FOL, which can help identify horsts, grabens, and potential strike-slip faults. Contrast in results between FOL and TOL are interpreted to represent predominately early versus late tectonic event. Rose diagrams for manually-extracted and automatically-extracted TOL are almost the same. Mineral occurrences and mines are generally, but not exclusively, associated with caldera rims and internal fractures and faults. A positive correlation exists between FOL and mineral occurrences. These results can be helpful for mineral exploration.

REFERENCES

Abdullah, A., Akhir, J.M., and Abdullah, I. 2010. Automatic Mapping of Lineaments Using Shaded Relief Images Derived from Digital Elevation Model (DEMs) in the Maran-Sungai Lembing Area, Malaysia: Electronic Journal of Geotechnical Engineering, v.15, p. 949-957.

Abdullah, A., Nassr, S., and Ghaleeb, A. 2013. Landsat ETM-7 for Lineament Mapping using Automatic Extraction Technique in the SW part of Taiz area, Yemen: Global Journals Inc. (USA) v. 13, p. 34-38

Acharya, T., Basumallik, S., and Paul, S.K. 2007. Comparative analysis of lineaments and fractures in Precambrian crystalline rocks using remote sensing and field technique: A case study in and around Balarampur, Purulia District, West Bengal, India; Abstract, Proc: International Conference on Precambrian Sedimentation and Tectonics and Second GPSS Meeting, 10–12 December 2007, IIT Bombay, Mumbai, p. 68–69.

Agnico Eagle., Pinos Altos, Website: https://www.agnicoeagle.com/English/operations-and-development-projects/operations/Pinos-Altos

Aguirre-Díaz, G.J., and McDowell, F.W. 1991 The volcanic section at Nazas, Durango, Mexico, and the possibility of widespread Eocene volcanism within the Sierra Madre Occidental: Jour- nal of Geophysical Research, v. 96, p. 13373–13388.

Aguirre-Díaz, G.J., Labarthe, H.G., Tristan, G.M., Nieto, O.J., and Gutierrez, P.I. 2008 The Ignimbrite Flare-up and Graben Calderas of the Sierra Madre Occidental, Mexico: Developments in Volcanology, v.19, p. 143-180.

Aguirre-Díaz. G.J., and Labarthe, H. G. 2003. Fissure ignimbrites: fissure source origin for voluminous ignimbrites of the Sierra Madre Occidental and its relationship with Basin and Range faulting: Geology, 31, 773–776.

Alamos Gold, Mulatos, Website: www.alamosgold.com/mines-and-projects/producing-mine/mulatos-mine-mexico/.

Atwater, T., and Stock, J.M. 1988 Pacific-North America plate tectonics of the Neogene southwestern United States: An update: International Geology Review, v. 40, p. 375–402.

Bagby, W. 1979 Geology, Geochemistry, and Geochronology of the Batopilas Quadrangle Sierra Madre Occidental Mexico: Unpublished Ph.D. Thesis, Santa Cruz, The University of Cali- fornia Santa Cruz, 271 p, 1 map.

Beckton, J.M., 2004, Resource report — Palmarejo, June 2004: Internal report of Planet Gold, SA de CV., 47 p.

Bockoven, N.T. 1980 Reconnaissance Geology of the Yecora-Ocampo Area, Sonora and Chihuahua, Mexico: unpublished Ph. D. Thesis, Austin, the University of Texas, p. 185-197.

Bryan, S.E., Ferrari, L., Reiners, P.W., Allen, C.M., Petrone, C.M., Rosique, A.R., and Camp- bell, I.H., 2008, New Insight into Crustal Contributions to Large-volume Rhyolite Genenration in the Mid Tertiary Sierra Madre Occidental Province, Mexico, Revealed by U-Pb Geochronology: Journal of Petrology, v. 49, p. 47-77.

Byington, C.B., and Bybee, R.W. 2000. An integrated structural analysis and target identifica- tion of the Ocampo gold-silver project, Chihuahua, Mexico. Millennium Mining Associates: For Gammon Lake Resources, Inc., internal unpublished report.

Cameron, K., Nimz, G., Kuentz, D., Niemeyer, S., and Gunn, S. 1989. Southern Cordilleran basaltic andesite suite, southern Chihuahua, Mexico: A link between Tertiary continental arc and flood basalt magmatism in North America: Journal of Geophysical Research, v. 94, p. 7817-7840.

Camprubí, A., Ferrari, L., Cosca, M.A., Cardellach, E., and Canals, A. 2003. Ages of Epithermal Deposits in Mexico: Regional Significance and Links with the Evolution of Tertiary Volcanism: Economic Geology; v. 98, p. 1029-1037.

Cather, S.M., Dunbar, N.W., McDowell, F.W., McIntosh, W.C., and Scholle, P. A. 2009. Climate forcing by iron fertilization from repeated ignimbrite eruptions: The icehouse–silicic large igneous province (SLIP) hypothesis. v. 5, no. 3, p. 315–324.

Chernicoff, C.J., Richards, J.P., and Zappettini, E.O. 2002. Crustal lineament control on magmatism and mineralization in northwestern Argentina: geological, geophysical, and remote sensing evidence: Ore Geology Reviews, v.21, p. 127–155.

Clark, K.F., Foster, C.T., and Damon, P.E. 1982. Cenozoic mineral deposits and subduction-related magmatic arcs in Mexico: Geological Society of America Bulletin, v. 93, p. 533-544.

Coeur Mining Inc., Palmarejo, Website: www.coeur.com/operations/mines/palmarejo-mexico

Corbett, G. 2004. Comments on Palmarejo, El Realito and Yecora Exploration Projects, Northern Mexico, private report for Planet Gold SA de CV., p. 37.

El-Sawy, E.K., Ibrahim, M.I., El-Bastawesy, M.A., and El-Saud, W.A. 2016. Automated, manual lineaments extraction and geospatial analysis for Cairo-Suez district (Northeastern Cairo- Egypt), using remote sensing and GIS: International Journal of Innovative Science, Engineering & Technology, v. 3, p. 491-500.

Faulds, J.E., and Varga, R.J. 1998. The role of accommodation zones and transfer zones in the regional segmentation of extended terranes: Geological Society of America Special paper 323.

Feinstein, M.N. 2007. Contributions to the Geology of the Cuenca de Oro: Chihuahua, Mexico: Unpublished M. Sc. thesis, El Paso, University of Texas at El Paso, 642 p., 42 maps.

Ferrari, L., and Valencia-Moreno, M. 2007. Magmatism and tectonics of the Sierra Madre Occidental and its relation with the evolution of the western margin of North America, in Alaniz- Álvarez, S.A., and Nieto-Samaniego, Á.F., eds., Geology of México: Celebrating the Centenary of the Geological Society of México: Geological Society of America Special Paper 422, p. 1–39. \

Ferrari, L., López-Martínez, M., and Rosas-Elguera, J. 2002. Ignimbrite flare- up and de-formation in the southern Sierra Madre Occidental, western Mexico—implications for the late subduction history of the Farallon Plate: Tectonics, v. 21, doi: 10.1029/2001TC001302.

Ferrari, L., Pasquarè, G., Venegas, S., and Romero, F. 2000.Geology of the Western Mexican Volcanic Belt and Adjacent Sierra Madre Occidental and Jalisco Block, in Delgado-Granados, H., Aguirre-Díaz, G.J., and Stock, J.M., eds., Cenozoic Tectonics and Volcanism of Mexico: Geological Society of America Special Paper 334, p. 65–84.

Galvan-Gutierrez, V.H. 2005. Regional and local patterns of mineralization of the lower Batopilas and Urique rivers in Sierra Madre of Chihuahua, Mexico: Unpublished M. Sc. thesis, El Paso, University of Texas at El Paso, 116 p.

Gold Corp Inc., El Sauzal, Website: www.goldcorp.com/English/portfolio/closed-sites/el-sauzal/default.aspx

González Reyna J. 1956. Memoria Geológico Minera del Estado de Chihuahua, XX Congreso Geológico Internacional, p. 98- 101.

Gonzalez-Leon, C.M., McIntosh, W.C., Lozano-Santacruz, R., Valencia-Moreno, M., Amaya Martinez, R., and Rodríguez-Castañeda, J.L. 2000. Cretaceous and Tertiary sedimentary, mag- matic, and tectonic evolution of north-central Sonora (Arizpe and Bacanuchi quadrangles), north- west Mexico: Geological Society of America Bulletin, v. 112, p. 600 – 610.

Goodell, P., and Sellepack, S. 1996. Analysis of lineaments in southwestern Chihuahua, Mex- ico: Mesozoic lateral movement: Geological Society of America Abstracts with programs 1996 Annual Meeting, p. A-190.

Goodell, P.C. 1995. Porphyry copper deposits along the Batopilas lineament, Chihuahua Mex- ico. Pierce, F.W., eds., Copper Deposits of the North American Cordillera: Arizona Geological Society Digest, p. 554.

Greenbaum, D. 1985. Review of remote sensing applications to groundwater exploration in basement and regolith: British Geological Survey Rep OD, v. 85/8, p. 36.

Guilluly, J., 1976, Lineaments–ineffective guides to ore deposits: Economic Geology, v. 71, no. 8, p. 1507-1514.

Henry, C., and Aranda-Gómez, J.J. 2000. Plate interactions control middle-late Miocene, proto-Gulf and Basin and Range extension in the southern Basin and Range: Tectonophysics, v. 318, p. 1–26.

Heyl, A.V. 1972. The 38th Parallel Lineament and Its Relationship to Ore Deposits. Economic Geology, v. 67, p. 879-894.

Horner, J.T., and Enríquez, E. 1999. Epithermal precious metal mineralization in a strike-slip corridor: The San Dimas district, Durango, Mexico: Economic Geology, v. 94, p. 1375–1380.

Islas, J., and Gastélum, G., 1988, Informe de la primer etapa de exploración del área Satevó, unpublished internal report; Compañía Fresnillo SA de CV.

Jicha, B.R., Scholl, D.W., and Rea, D.K. 2009. Circum- Pacific arc flare-ups and global cool- ing near the Eocene-Oligocene boundary: Geology, v. 37, p. 303– 306.

Karnieli, A., Meisels, A., Fisher, L., and Arkin, Y. 1996. Automatic extraction of geologi- cal linear features from digital remote sensing data using a Hough Transform, Photogrammetric Engineering & Remote Sensing, v. 62, p. 525–531.

Katz, M. 1982. Lineament analysis of Landsat imagery applied to mineral exploration. In Mineral exploration techniques in tropical forest areas. Edited by Lamining. D.I.C and Gibbs, A.K. Hiden Wealth , p.157-166.

King, R.E.1939. Geological Reconnaissance in Northern Sierra Madre Occidental of Mexico: Geological Society of America Bulletin, v. 50, n. 11, p. 1625-1722.

Kutina, J.1980. Are lineaments ineffective guides to ore deposits? : Global Tectonics and Metallogeny, p. 200–205.

Laming, D.J.C., and Gibbs, A.K., eds., Hidden Wealth: mineral exploration techniques in tropical forest areas: Geosciences in International Development, AGID Report, n.7; p. 157-166

Laurent, I. 2004. Palmarejo/Trogan Project: Annual technical report, 1st July 2003 – 30th June 2004, internal report of Planet Gold SA de CV., 118 p.

Lee, J., Miller, M.M., Crippen, R., Hacker, B., and Vazquez, J.L. 1996. Middle Miocene extension in the gulf extensional province, Baja California: Evidence from the southern Sierra Juarez: Geological Society of America Bulletin, v. 108, p. 505–525.

Manriquez, R. 2005. Characteristics of Epithermal Gold Deposits in the North of the Sierra Madre Occidental, Mexico: Unpublished M. Sc. thesis, El Paso, University of Texas at El Paso. 328p.103p.

Marshall, B. 1979. Lineament - Ore Association, Economic Geology, v. 74, p. 942-946.
Mayo, E.B., 1958, Lineaments Tectonic and some ores district of the southwest: AIME Trans, p. 1169-1175.

McDonough, C.C. 2005. Characterization of the La Reforma Mini Basin and Range Province, and constraining the nature of the Seri-Tahue Terrane Boundary, Tasajeras Quadrangle, northwest- ern Mexico: Unpublished M.Sc. thesis, El Paso, University of Texas at El Paso 4 p.

McDowell, F.W., 2007, Geologic transect across the northern Sierra Madre Occidental volcanic field, Chihuahua and Sonora, Mexico: Geological Society of America Digital Map and Chart Series 6, p.70.

McDowell, F.W., and Clabaugh, S.E., 1979, Ignimbrites of the Sierra Madre Occidental and their relation to the tectonic history of western Mexico, Geological Society of Amerce, Special Paper 180, p. 113 – 124,.

McDowell, F.W., Roldán-Quintana, J., and Amaya-Martínez, R. 1997. Interrelationships of sedimentary and volcanic deposits associated with Tertiary extension in Sonora, Mexico: Geological Society of America Bulletin; v.109; no. 10; p. 1349-1360.

Minera Frisco, Ocampo, Website: www.minerafrisco.com.mx/Paginas/EN/our_bussines/mini ng_units/OCAMPO.aspx

Murray, B., Busby, C., Ferrari, L., Solari, L. 2013. Synvolcanic crustal extension during the mid-Cenezoic ignimbrite flare-up in the northern Sierra Madre Occidental, Mexico: Evidence from the Guazapares Mining District region, western Chihuahua, Geosphere, v. 9, n. 5, p. 1-35.

Nieto-Samaniego, Á.F., Ferrari, L., Alaniz-Álvarez, S.A., Labarthe-Hernández, G., and Rosas Elguera, J. 1999.Variation of Cenozoic extension and volcanism across the southern Sierra Madre Occidental volcanic province, Mexico: Geological Society of America Bulletin, v. 111, p. 347–363.

O'Driscoll, E.S.T. and Campbell, I.B. 1997. Mineral deposits related to Australian continental ring and rift structures with some terrestrial and planetary analogies: Global Tectonics and Metallogeny, v. 6, p. 83-101.

Overbay, W.J., Page, T.C., Krasowski, D.J., Bailey, M.H., and Matthews, T.C. 2001. Geology, structural setting, and mineralization of the Dolores District, Chihuahua, Mexico; in Albinson, T., and Nelson, C.E. eds.: Society of Economic Geologists Special Publication, n. 8, p. 71-85.

Palmer, H.N., 1883, Mulatos mining camp: Unpublished report, 15 p.

Pan American Silver Corp, Dolores, Website: www.panamericansilver.com/operations/advanced-stage/Dolores/.

PCI,. 2009. Geomatica Version 10.3 Users Manual: PCI Geomatics Enterprises, Inc., Ontario, Canada, accessed September 29, 2011, at http://www.pcigeomatics.com/.

Podwysocki, M. H., & Earle, L. 1979. Proceedings of the Second International Conference on Basement Tectonics: Basement Tectonics Committee, 595 Pages.

Querol, F., and Mendoza, H. 1996. Description and geologic model of the Satevo area, Municipality of Batopilas, state of Chihuahua, Mexico. In Goodell, P.C., Reyes C, I.A., Reyes C, M., and Carreon M, P.J. eds, Conferencia Internacional de Mineria, VI Excursion Geologica al Cenozoico de Chihuahua: El Paso Geological Society, p. 259-272.

Rasmussen, H., Nasi, C., Molina, C., and Holbach. 2014. Geology and Exploration History of the Palmarejo Silver and Gold District, Chihuahua, Mexico. In Gastelum M., G., editor: Gold and Silver Mines of the Sierra Madre Occidental, Mexico: Society of Economic Geologists Guidebook Series v. 42, p. 37-48.

Sedrette, S., and Rebaï, N. 2016. Automatic extraction of lineaments from Landsat Etm+ images and their structural interpretation: Case Study in Nefza region (North West of Tunisia) : Journal of Research in Environmental and Earth Sciences, v. 4, p.139–145.

Sellepack, S., Goodell, P. and Charest, A. 1996. A preliminary report on a disseminated gold prospect, Sausal, Chihuahua, México; in Grassroots Exploration in the Batopilas Region, Chi- huahua: Conf. Internac. de Mineriá, Chihuahua, p. 231-236.

Smith, R.D., Cameron, K.L., McDowell, F.W., Niemeyer, S., and Sampson, D.E. 1996. Generation of voluminous silicic magmas and formation of mid-Cenozoic crust beneath north- central Mexico—evidence from ignimbrites, associated lavas, deep crustal granulites, and man- tle pyroxenites: Contributions to Mineralogy and Petrology, v. 123, p. 375–389, doi: 10.1007/s004100050163.

Smith, R.L., and Bailey, R.A. 1968. Resurgent cauldrons, in Coats, R.R., et al., eds., Studies in volcanology: Geological Society of America Memoir 116, p. 613–622.

Staude, J-M.G. 1993. Gold, silver, and base metal epithermal mineral deposits around the Gulf of California, Mexico—Relationship between mineralization and major structures: U.S. Ge- ological Survey Bulletin 2039, p. 69–78.

Staude, J-M.G. 1995. Epithermal mineralization in the Sierra Madre Occidental, and the Met- allogeny of northwestern Mexico: Unpublished Ph.D. dissertation, Tucson, University of Arizona, 248 p.

Staude, J-M.G., and Barton, M.D. 2001. Jurassic to Holocene Tectonics, Magmatism, and Metallogeny of Northwestern Mexico: Geological Society of America Bulletin; v. 113; no. 10; p. 1357-1374.

Steven, T.A., and Lipman, P.W. 1976. Calderas of the San Juan volcanic field, southwestern Colorado: U.S. Geological Survey Professional Paper 958, 35 p.

Steven, T.A., Lipman, P.W., Hail, W.J., Jr., Barker, Fred, and Luedke, R.G. 1974. Geologic map of the Durango quadrangle, southwestern Colorado: U.S. Geological Survey Miscellaneous Investigations Series Map 1-764, scale 1:250,000.

Stock, J.M., and Hodges, K.V., 1989, Pre-Pliocene extension around the Gulf of California and the transfer of Baja California to the Pacific plate: Tectonics, v. 8, p. 99–115.

Swanson, E.R., and McDowell, F.W. 1984. Calderas of the Sierra Madre Occidental volcanic field western Mexico: Journal of Geophysics Research, v. 89, no. B10, p. 8787-8799.

Swanson, E.R., Kempter, K.A., McDowell, F.W., McIntosh, W.C. 2006. Major ignimbrites and volcanic centers of the Copper Canyon area: A view into the core of Mexico's Sierra Madre Occidental: Geosphere, v.2, no. 3, p. 125-141

Wark, D.A., Kempter, K.A., and McDowell, F.W. 1990. Evolution of waning, subduction related magmatism, northern Sierra Madre Occidental, Mexico: Geological Society of America Bulletin, v. 102, p. 1555-1564.

Wisser, E.D. 1966. The Epithermal Precious Metal Province of Northwest Mexico: Nevada Bureau of Mines, Report 13, pt. C, p.63-92.

Wlkerson, G., Deng, Q, Llavona, R., and Goodell, P. 1988. Batopilas Mining District, Chihuahua, Mexico: Economic Geology; vol. 83; p. 1721-1738.

Zakir, F., Qari, M., and Mostfa, M. 1999. A new optimizing technique for preparing lineament density maps: International Journal of Remote Sensing, v. 20, p.1073–1085.

Table 1: Table 1 Data used for this project.

Data	Manually extracted	Automatic extracted	Circle	Density map	Rose diagram	Profile elevation
Landsat 8	**X**	**X**	**X**	**X**	**X**	
DEM			**X**			**X**
Mineral Occurrences	**X**		**X**	**X**		
Major mines	**X**		**X**			

Table 2: First Order Lineaments (see Figure 5).

Lineament	Location	Length (km)	Strike	Mineral Occurrences
L1	108°47'25.556"W, 29°6'20.965"N	34	Northwest–southeast	
L2	108°36'37.542"W, 28°58'50.078"N	89	Northwest–southeast	Huizopa, Las Animas, and Milagros prospects. And Moris mine
L3	108°5'40.106"W, 28°53'40.726"N	65	Northwest–southeast	
L4	107°45'34.731"W, 28°55'7.183"N	76	Northwest–southeast	
L5	108°2'57.497"W, 28°21'7.108"N	46	East-west	Concheno, Cubiro, El Madrono, and Santa Brigida prospects
L6	108°28'30.698"W, 28°3'53.841"N	50	Northwest–southeast	Cerro Amarillo, Santa Maria, Moris mines
L 7	108°17'57.232"W, 27°46'58.09"N	51	Northeast-southwest	Agua Caliente mine, Guadalupe Victoria, Guasisa, Pariachi, and San Rafael De Orivo
L8	108°30'19.729"W, 27°20'22.33"N	27	Northwest–southeast	La Millonaria mine, and Los Plantanos
L9	108°15'33.708"W, 27°18'12.282"N	28	North-south	Tarahumara
L10	107°45'19.77"W,	51	Northeast–	Los Amoles, and San Miguel prospects

	27°30'44.684"N		southwest	
L11	107°54'27.341"W, 27°14'27.369"N	34	North - south	Cuesta Colorada, El Platano, Guapaliana,
12	107°57'21.661"W, 27°9'48.895"N	18	East- west	Urique District mine, and Cieneguita prospect
L13	107°55'50.805"W ,27°4'8.976"N	23	Northwest – southeast	Sauzal prospect, Piedras Verdes, and Gloria
L14	107°51'31.718"W, 27°1'20.394"N	32	West- east	Tres Hermanos
L15	107°53'23.896"W, 26°59'28.884"N	12	East north – southeast	
L16	107°47'15.885"W, 26°51'24.28"N	54	North west – south east	Jesus Maria, Polanco, Rio Urique
L17	107°31'59.573"W, 26°51'6.687"N	24	East north – southeast	
L18	108°51'22.657"W 28°38'55.455"N	27	North west – south east	
L19	108°13'47.31"W 26°54'13.809"N	29	East west	
L20	108°44'33.414"W 27°6'28.969"N	37	North west – south east	El Toro

Table 3: Previously known calderas.

Number	Caldera Name	Location	Average Diameter (km)	Average West Elevation (m)	Average East Elevation (m)	Mineral Occurrences	Shape	Structures	References
1	Co- Corralito	107°42'52.508"W 28°35'2.526"N	27	1950	2050		circle	There is a radial fracture inside this caldera	Swanson and McDowell, (1984)
2	V - Las Varas	108°13'45.173"W 28°27'45.536"N	12.5	2050	2150	Cinco De Abril, Magistral, and Tutuaca	circle	This caldera contains radial fractures striking northeast, or it may have domal fractures	Wark et al., 91990)
3	O - Ocampo	108°24'38.642"W 28°11'28.406"N	32	900	1900	Boler La prospect, Candamena mine, Cerro Amarillo mine, El Madrono prospect, Jesus Del Monte prospect, La Aurora mine, La Boler prospect, La Plamosa prospect, Ocampo mine, Santa Brigida mine, Santa Maria – Moris mine, and Santa Maria Y Mocte mine	circle	It has two tangent lineaments from the east and west border L2 and L6 respectively, and internal fractures	Swanson and McDowell, (1984)
4	TO -Tómochic	107°56'45.682"W 28°18'37.044"N	21	2300	2000		ellipsoid	L5 is tangent to the northwest border There are some radial fractures WHERE?	Wark et al., (1990)
5	C- El Comanche	107°49'40.04"W 28°15'23.721"N	10	2150	2550		circle	There are radial fractures inside this caldera	Swanson and McDowell, (1984)
6	Ma- Manzanita	107°39'48.511"W 28°14'53.102"N	15	230	2700		circle	There is tangent lineament to the northwest border. Radial fractures appear from the outside of the north and west borders.	Swanson et al., (2006)

								There are several fractures inside striking north-south	
7	SJ - San Juanito	107°51'47.131"W 28°9'46.805"N	14	2450	2350		circle	It has several radial fractures inside. The north and west borders have fractures from the outside	Swanson et al., (2006)
8	CK - Center Known	108°18'35.326"W 27°39'29.164"N	15	1000	2300	Guachajure , Guasisa, San Rafael De Orivo, and Setago prospects	circle	There is tangent lineament to the south border. This has radial fractures in the center that are striking northeast-southwest	Murry et al., (2013)
9	CC - Copper Canyon	107°45'7.486"W 27°35'46.798"N	26	2200	2400	Barranca De Cobre occurance	ellipsoid	Radial fractures	Swanson et al., 2006
10	SK - Southern Known	108°14'35.744"W 27°3'43.34"N	30	800	1800	Balojaque prospect, Churuguayvo prospect , El Refugio mine, El Terrero mine, La Guitarra prospect, La Piramide mine , La Reforma, Lluvia De Oro mine , Ocolomo prospect , San Pablo prospect, Septentrion prospect	circle	Tilted fractures are present	Murry et al., (2013)

Table 4: Potential calderas in the area of interest.

NO.	Circle Name	Location	Average Diameter (km)	Average West Elevation (m)	Average East Elevation (m)	Mineral Occurrences	Shape	Structures
11	N1	108°52'28.061"W 28°58'48.05"N	8.5	1300	1000	No	Elliptical, elongated to the south	There are radial fractures from the west and the northeast side
12	N2	108°26'19.279"W 28°46'1.1"N	17	1850	1500	Huizopa, Milagros, and Moris.	Circle	L2 is tangent on the west border. Radial fractures are present.
13	N3	108°10'56.21"W 28°34'55.483"N	46	2000	1700	La Fortuna, Cinco De Agua Salada, El Letrero, Magistral, and Tutuaca.	Circle	Fracture resurgence is present in the center of the caldera. There is an arc nearby.
14	N4	108°38'26.89"W 28°30'42.709"N	22	1350	1000	El Victor and Mulatos	Circle	There are radial fractures in the center and the northeast side
15	C1	108°50'32.44"W 28°15'34.042"N	9	1800	1900	La Cumbre and El Sauz	Elliptical	There are radial fractures in the center
16	C2	108°59'2.231"W 28°3'56.725"N	13	1650	1500	No	Circle	Graben and radial fractures are present inside the caldera
17	C3	108°38'41.22"W 27°55'39.972"N	32	800	600	La Cienega, Bojoruez, La Dura, El Pilar, El Pino, El Pinto, El Zapote, Los Otates, Pamachi, Sahuayacan , Socorro Toroibo, Sahuayacancito San Jose, La Muelita, and	Oval	L6 is tangent to the west margin. Another SOL is tangent to the north margin.

						El Zorillo		
18	C4	108°11'30.403"W 28°1'27.781"N	8	2450	2000		Circle	Radial fractures are located around the center
19	C5	108°4'38.783"W 27°54'34.173"N	7.5	1500	2250		Elongated to the north	Two TOL are tangent to the west and east borders of the circle
20	C6	107°59'36.912"W 27°47'28.255"N	10	1950	1500	Maguarichic mine, and Santa Marta occurrence	Elongated to the east	Two lineaments are tangent with the north and west border. Radial fractures appear in the center, and on the east border of this caldera. Santa Marta is near the north border
21	C7	107°58'56.983"W 27°47'5.388"N	13	2450	2350		Oval	Radial fractures are inside and from outside the north margin.
22	S1	108°43'10.226"W 27°30'10.712"N	25	800	300	El Limon prospect, El Manto mine, Japon En Mexico mine, San Francisco De Churo prospect, Sara Alicia prospect, and Tetamoa mine.	Circle	Northeast-trending radial fractures inside.
23	S2	108°27'14.968"W 27°20'28.523"N	32	1600	1500	Guadalupe, Zargo , Agua Caliente Sangre Det, Batosegachic , Guazapares , Tarahumara, Septentrion	Circle	L9 is tangent to the east rim. L7 is tangent to the northwest rim. This caldera overlaps with S3 and S4.
24	S3	108°23'11.461"W 27°21'10.432"N	28	1600	1100	Cordon Del, Hierba La, Cerro Santa, Elena, Lobera, Gavaldon, Cerro San, Miguel, Chinipas, El Zapote Del Cura,	Circle	L8 crosses this circle with the northwest rim. Radial fractures are present. This caldera overlaps S2 and S4.

						Gasoriachi, Husuruapa, Justina, Justina Dos, La Currita, La Esperanza, Los Plantanos, Mesa De Zamorano, Reyna De Oro La, Santa Ursula, Sulema, Virginia, La Millonaria, La Patria, Palmarejo, and San Aurelia		
25	S4	108°21'31.679"W 27°14'10.882"N	7 km	600	1450		Circle	Radial fractures are inside. This caldera overlaps with S2 and S3.
26	S5	107°44'11.262"W 27°18'53.524"N	23 km	2300	1500	Los Amoles, San Miguel, Guadalupe, Cororado, and Chipayvo	Circle	L10 is tangent to the northwest rim. L11 is tangent to the west rim. Radial fractures inside.
27	S6	108°29'50.465"W 26°54'54.589"N	32 km	500	300	Algorroba-Pichucate , Maria , and La Verde	Circle	Several northwest-trending radial fractures inside.

Table 5: This table compares observed location of mines on ArcMap image with location given in USGS shape file.

Mine Name	Location from the USGS shapefile data
Ocampo	1.4 km northeast of the mine
Dolores	0.2 km to the southeast of the actual mine
Palmerjo	0.6 km is in the southwest of the mine
Santa Maria	location is in the center of the Santa Maria mine
Mulatos	location is in the center of the mine
El Madrono	location is at the northeast border of the mine

Table 6: Selected local and regional characteristics of the major epithermal precious metal deposits in the northern Sierra Madre.

No.	Site name	Type	Age (Ma)	Other types	Related Rocks	Local Structural Setting	Ore Control	Deposit Styles
1	Dolores	LS	38 - 35 (non-radiometric	Not known	Latite	NW trending extensional faults	Faults and dike contacts	Veins, stockworks and disseminated
2	Mulatos	HS	33 - 25	Base - metal veins	Dacite	NE shear zone with NW extensional faults	Favorable rocks and faults	Disseminated (stratabound and elongated pods)
3	Pinos Altos	LS	Unknown	Not known	Rhyolite	NWW trending extensional faults	Faults	Veins
4	Ocampo	LS	29.2 - 27.8	HS	Hosted by LVS	NW, NWW, N, NNE trending extensional faults	Faults, permeable rocks	Veins and stockworks
5	Los Jarros	HS	Unknown	Base metal veins	Rhyolite and dacite?	Not known	Faults	Veins (ledges) and disseminated
6	Palmarejo	LS	Unknown	Not known	Dioritic and rhyolitic intrusion	NNW strike- slip structures	Faults	Veins and stockworks
7	Cerro Colorado	HS	Unknown	Base metal veins	Dioritic intrusion?	NE left - lateral shear zone	Favorable rocks and faults	Disseminated (stratabound) and hydrothermal breccia
8	Satevo	HS and LS	Unknown	Porphyry	hosted by felsic and andesitic rocks	?	Variable	Disseminated (stratabound) and hydrothermal breccia, also porphyry
9	El Sauzal	HS	31- 29	Base metal veins	Dacite- andesite	NW strike- slip with N and NE extensional faults	Favorable rocks and faults	Disseminated
10	Batopilas	LS	Early - middle Tertiary rocks	Base metal veins	LVS	lineament strikes N-S	faults	Native silver in vein, nearby porphries

Table 6: Continued

No.	Site name	Ore mineralogy	Regional structure	Grades	Company	Total production / reserves	References
1	Dolores	Native gold and silver, silver sulfosalts	Within a caldera	0.58 g/t Au and 11 g/t Ag	Pan American	584,000 oz of Au and 25.4 million oz of Ag (2016)	Overbay et al. (2001)
2	Mulatos	Electrum	Within a caldera	1 g/t of Au	Alamos Gold Inc	1.7 million oz of Au (2016)	Palmer, (1883): Wisser, (1966); Clark et al., (1982)
3	Pinos Altos	Native gold and electrum	NWW faults, caldera rim, graben	12-15 g/t of Au and 80-150 g/t of Ag	Agnico Eagle	221,237 oz Au and 2.7 million oz Ag (2018)	Bockoven, (1980); Swanson and McDowell, (1984)
4	Ocampo	Native gold and silver, silver sulfosalts	Within a caldera, graben	1.46 g/t Au and 61 g/t Ag	Minera Frisco	54,725 oz of Au (up 16.9%) and 2.2456 million oz of Ag (2011)	Bockoven, (1980);Bybee, (2000)
5	Los Jarros	Native gold	Caldera rim, graben	0.58 g/t Au and 11 g/t Ag	Manhattan Minerals Ltd.	Resource of 47 million tons, 0.58 g/t Au and 11 g/t Ag, at a cutoff grade of 0.3 g/t Au. (2011)	Bockoven, (1980)
6	Palmarejo	Electrum, native gold, silver, and silver sulfosaltes	Within a caldera	495,000 oz of Au and 70.15 million ounces of Ag contained in 9.8 million tones	Coeur	122,722 oz Au and 7.5M oz of Ag (2018)	Laurent, (2004); Corbett (2004); Beckton, (2004)
7	Cerro Colorado	Native gold and gold bearing pyrite	NWW regional lineaments	60 g/t of Au			Galván, (2005)
8	Satevo	Native gold, galena, sphalerite, chalcopyrite	NWW regional lineaments.	NA	COFRESA		Islas and Gastélum, (1988); Querol and Mendoza, (1996)
9	El Sauzal	Native gold	Pull- aprt basin	3.34 g/t Au and 3.72 g/t Ag	Gold Corp.		Goodell and Sellepack, (1996); Goodell et al., (1997); Galván,(2005)

10	Batobiles	Native silver	NS lineament				Gonzales, (1956); Cameron and Bagby, (1981); Wilkerson, et al, (1988); Galván, (2005)

Table 7: The relationship between calderas and mineral occurrences.

Known and potential calderas	Mineral occurrences
V - Las Varas	Tutuaca prospect is located 3 km from the northeast border of this caldera, while the Magistral mine is located 3 km from the east rim. Cinco De Abril prospect is 4.5 from the western border.
O - Ocampo	Ocampo, Pinos Altos, and Moris mines and several mineral occurrences.
SJ - San Juanito	La Nortena prospect is present on the north rim of SJ caldera.
CC - Copper Canyon	Barranca De Cobre occurrence is located inside the caldera to the south region.
CK - Central Known	San Rafael De Orivo prospect is in the center of this caldera. Setago occurrence is on the southwest border. Guasisa prospect is 3 km from the west border. Guachajure is 2.5 km from the southwest border.
SK - Southern Known	Several mineralization sites are inside it.
N2	Milagros prospect and Moris mine are about 3 km southwest of N2.
N3	La Fortuna Au and Ag occurrence is 1 km west of the caldera. Cinco De Abril prospect is on the southwest border. In the south border, Agua Salada prospect and El Letrero past producer mine are 2 km average of the distance. Magistral mine and Tutuaca prospect are inside the southern part of the caldera.
N4	El Victor prospect and Mulatos mine are about 7 km to the north.
C1	La Cumbre occurrence 0.3 km to the north. El Sauz prospect is 1.6 km to the south.
C3	Fourteen mines and prospects: La Cienega mine, Bojorquez past producer mine, Castillo, Dura La, El Pilar, El Pino, El Pinto, El Zapote, Los Otates, Pamachi, Sahuayacan, Socorro, Toroibo, Sahuayacancito occurrences. San Jose Del Pinal prospect is located on the south rim. La Muelita prospect is 1.8 km north. El Zorillo occurrence is 2.3 km northwest.
C7	Santa Marta is near the north border. Maguarichic mine is the center of this caldera.

S1	San Rafael De Orivo and Guachajure occurrences are inside the caldera. Guasisa occurrence is 2 km outside the east rim of the caldera.
S2	Agua Caliente occurrence is 1.8 km north. Technique occurrence is inside the caldera, 1.7 km from the north rim. Within 2-3 km of the northeastern rim are the Sangre De Cristo prospect and the Batosegachic former producer mine. Guazapares past producer is inside and near the east border. The southeast border has the Tarahumara occurrence. Septentrion occurrence is south of the caldera.
S3	Four occurrences are outside the east border: Cordon Del Medio, La Hierba, Cerro Santa Elena, and Lobera. Gavaldon is 3 km distance from the south border. 20 mines and prospects are inside the caldera: Cerro San Miguel, Chinipas, El Zapote Del Cura, Gasoriachi, Husuruapa, Justina, Justina Dos, La Currita, La Esperanza, Los Plantanos, Mesa De Zamorano, Reyna De Oro La, Santa Ursula, Sulema, and Virginia prospects, and La Millonaria, La Patria, Palmarejo, San Aurelia past producer mines.
S5	Los Amoles prospect is on the northwest border, and San Miguel prospect is 3 km from the northwest border. Guadalupe Cororado is on the southwest border, and Chipayvo prospect is 1.6 km from the southwest border.
S6	Algorroba-Pichucate past producer mine and Maria prospect are inside this caldera. 1.6 km from the east border is La Verde prospect. Rosario mine is 0.5 from the southeast rim.

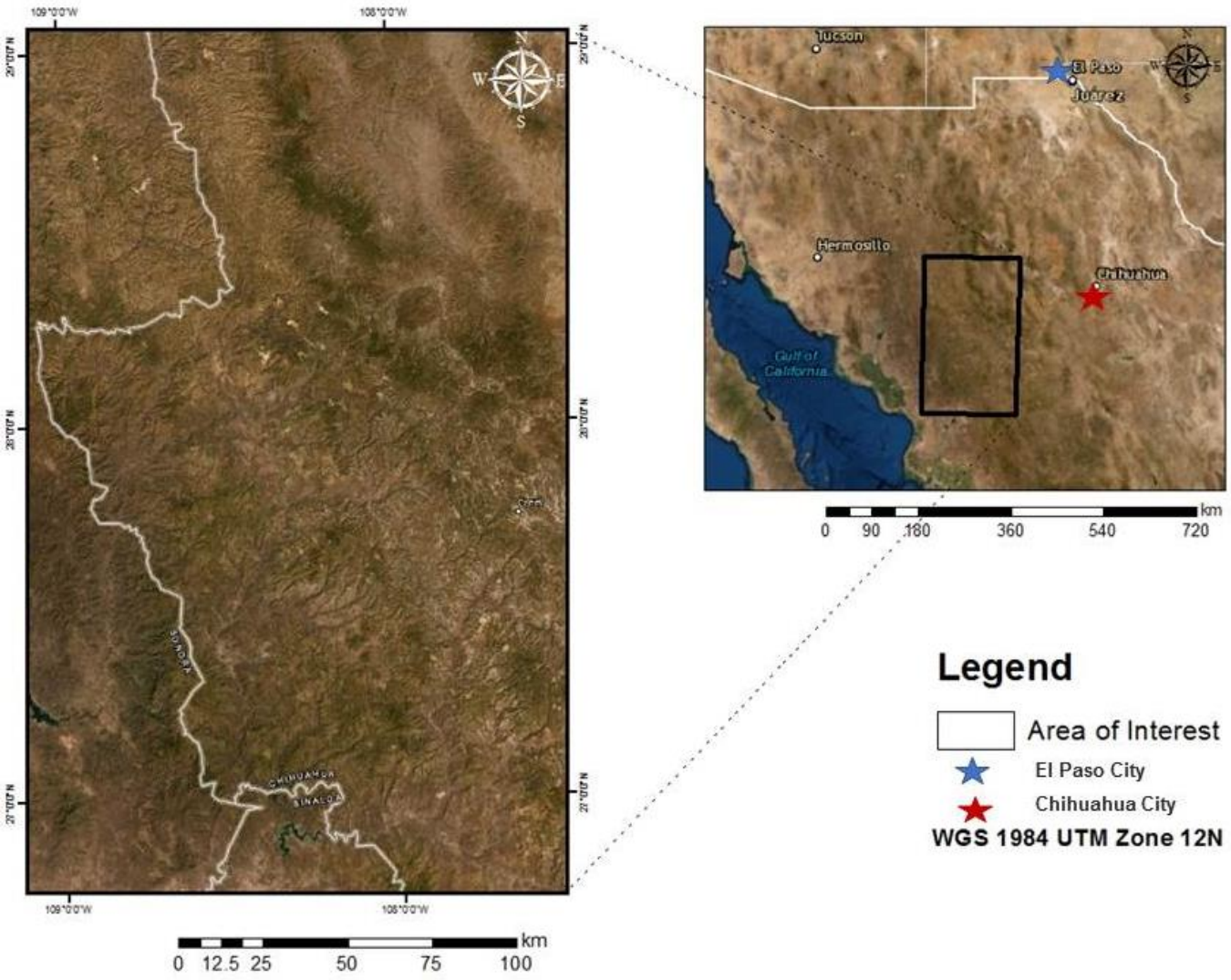

Figure 1: The area of interest (270×164 km).

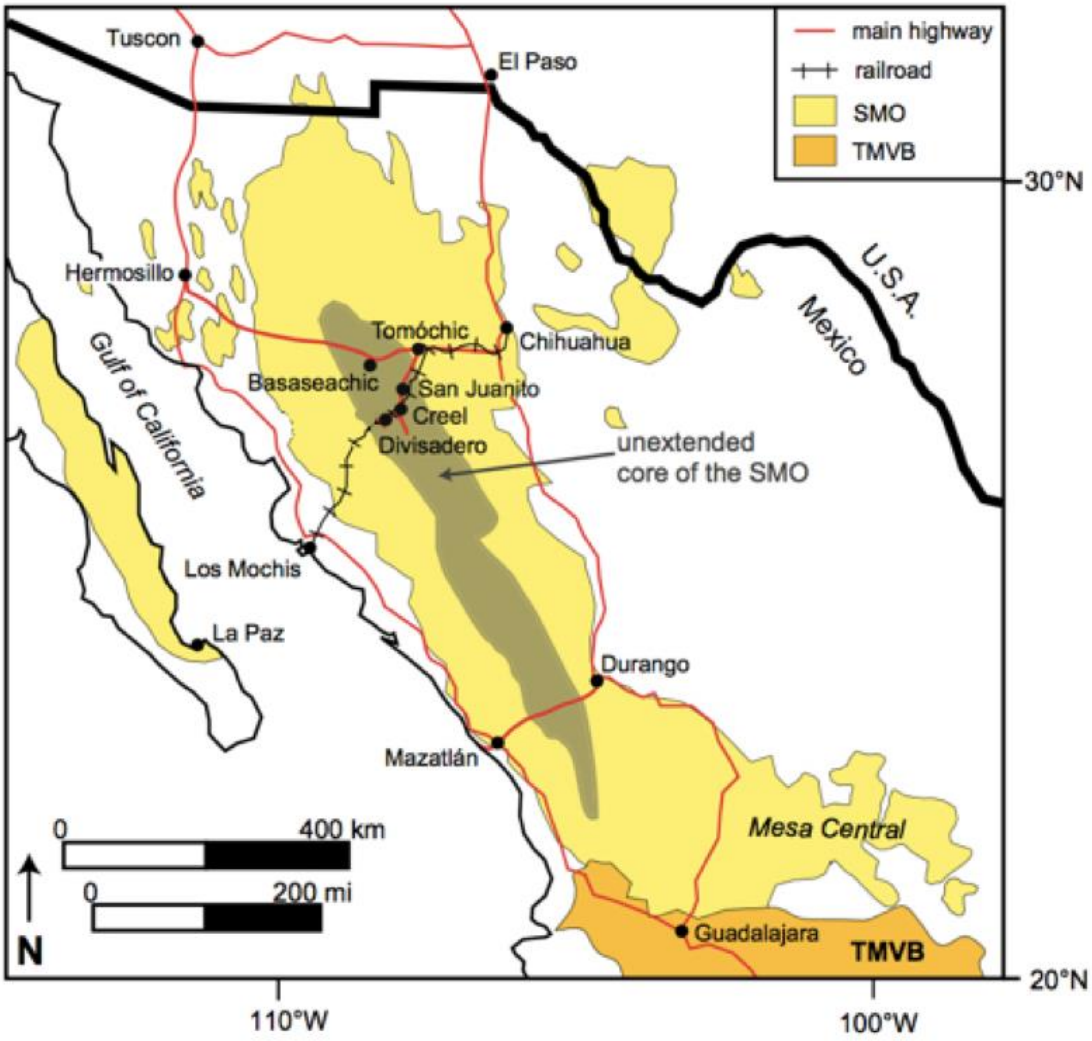

Figure 2: Generalized map of western Mexico showing the extent of the Sierra Madre Occidental dental (SMO) silicic large igneous province and contemporaneous igneous rocks (light yellow) and the relatively un-extended core (dark gray) of the SMO (after Henry and Aranda – Gomez, 2000; Ferrari et al., 2002; Bryan et al., 2008) Modified from Marry et al., (2013).

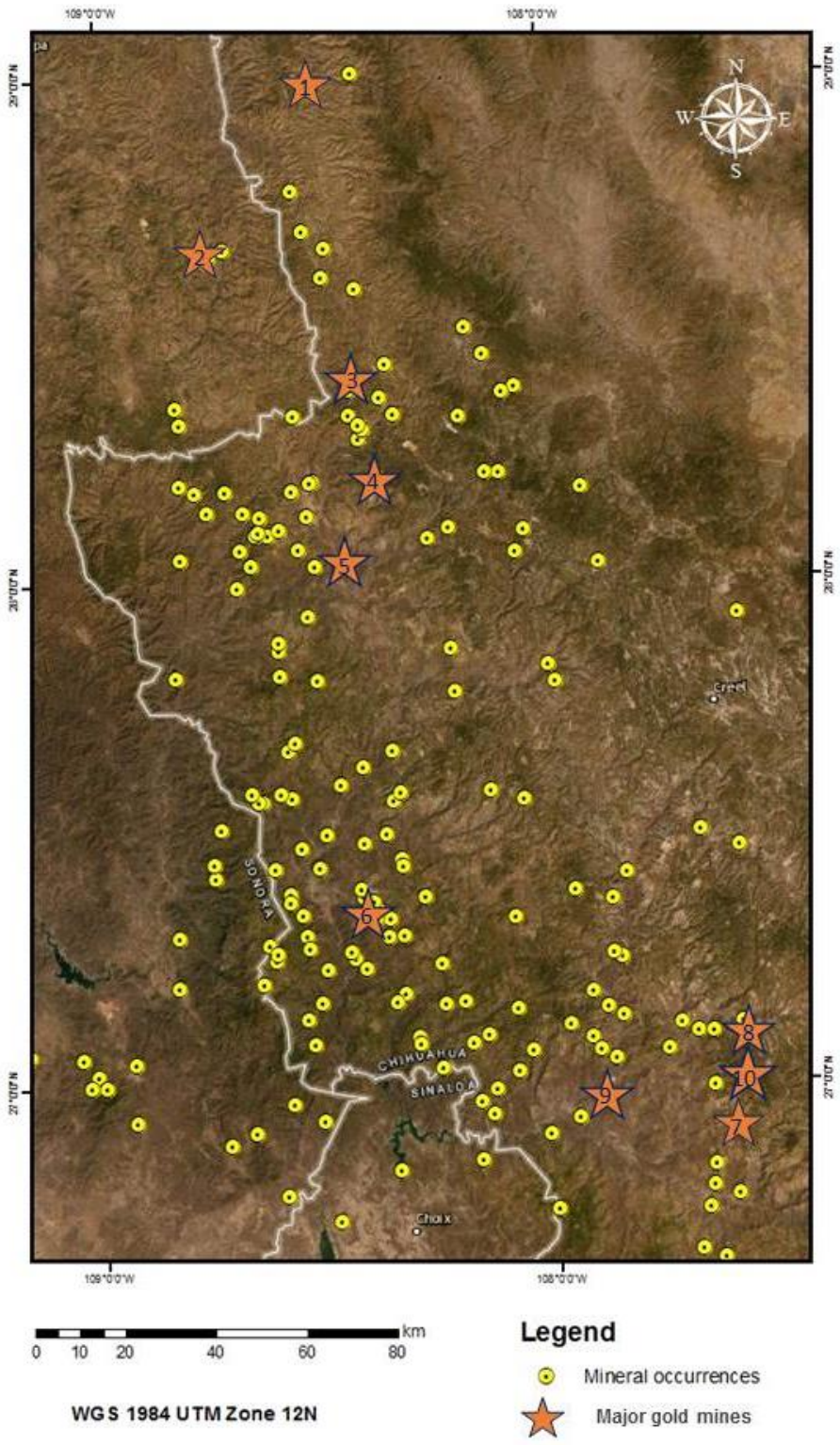

Figure 3: Mineral occurrences and the 10 major gold systems in the study area. Numbers with stars correlate with Table 5.

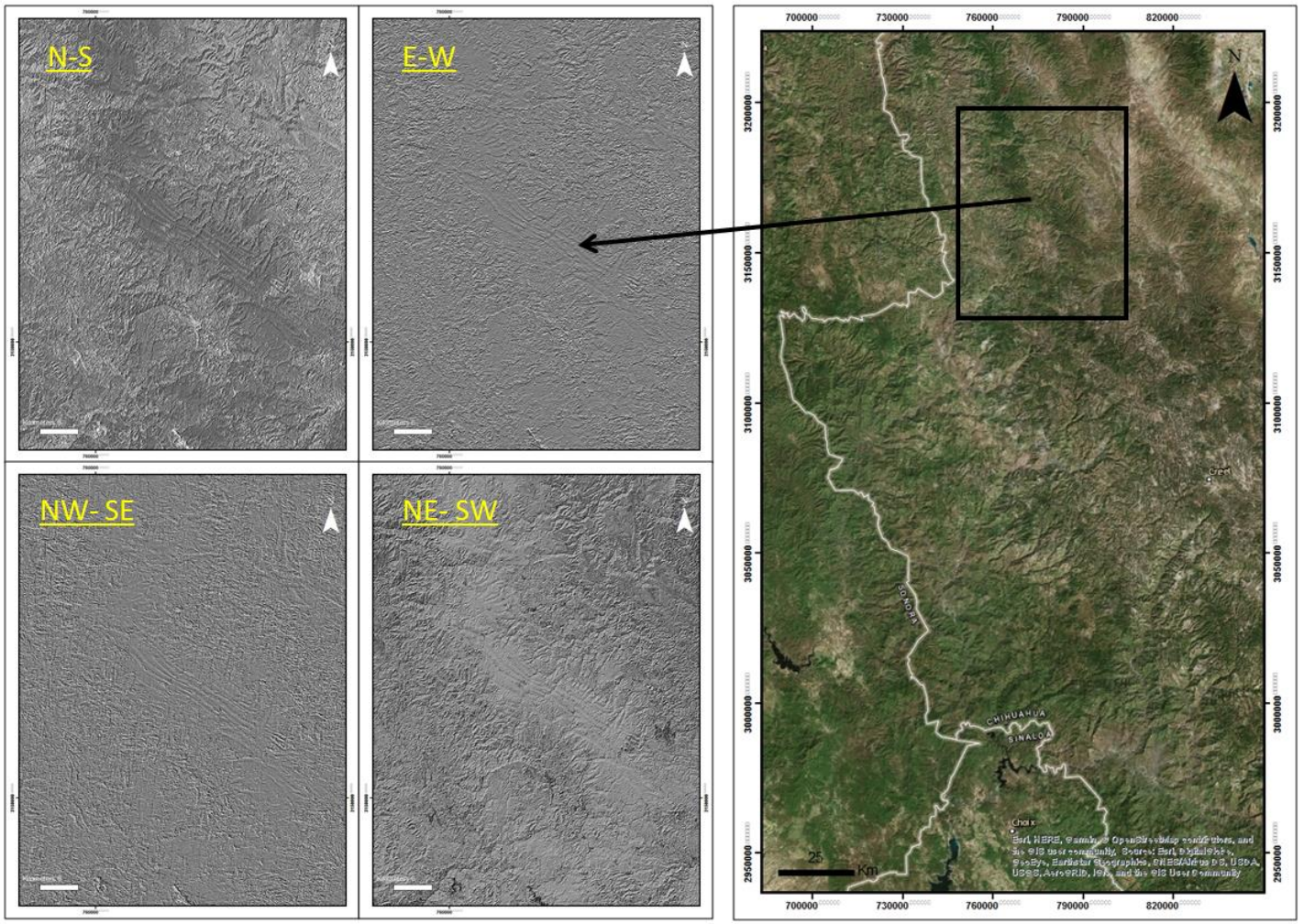

Figure 4: A small area of the Landsat 8 image (far right) with four directional filters (N-S, E-W, NE-SW and NW-SE) applied.

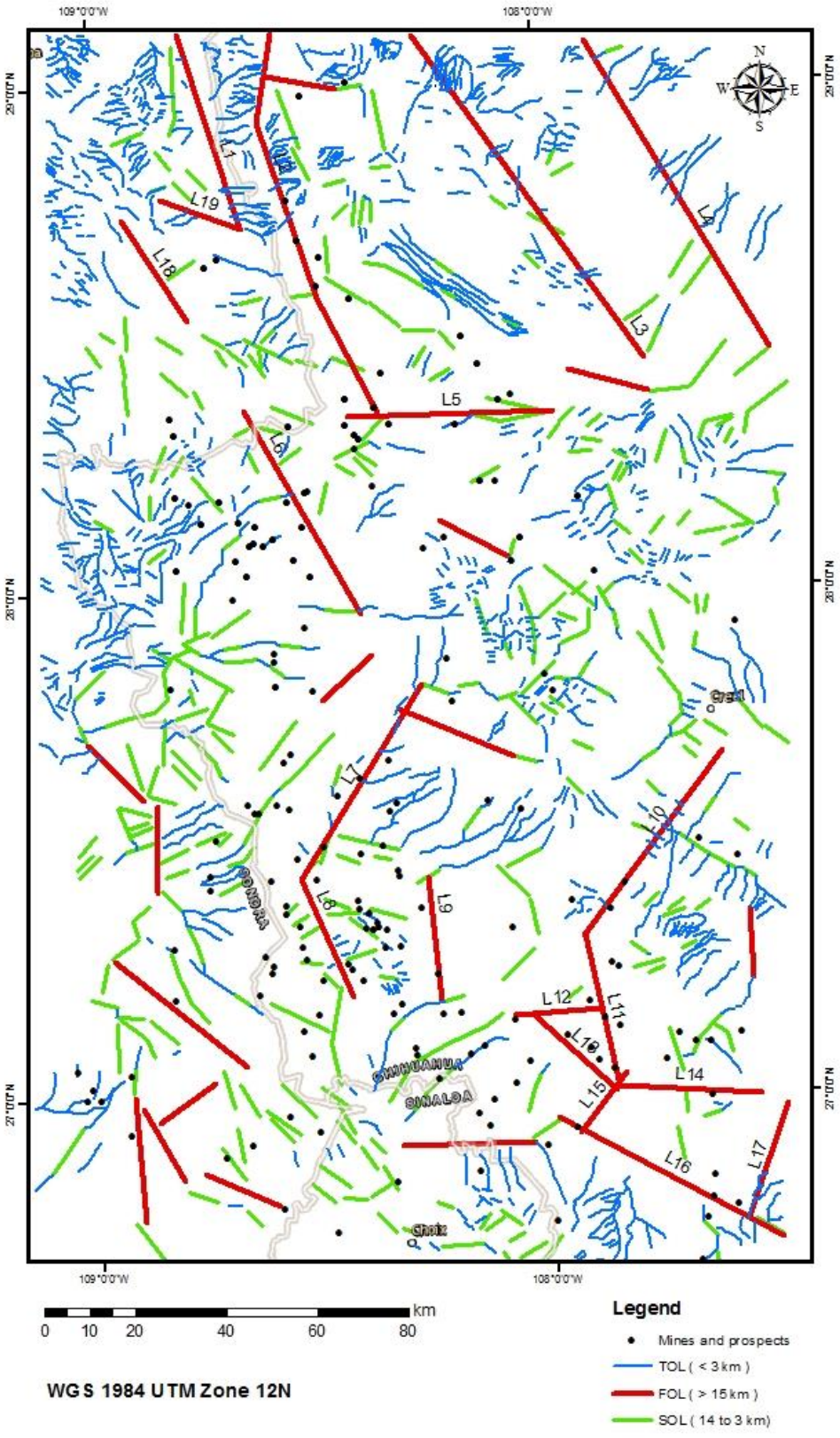

Figure 5: the map shows the Frist Order Lineament (FOL), Second Order Lineament (SOL), Third Order Lineament (TOL) and mines and prospects the area of interest.

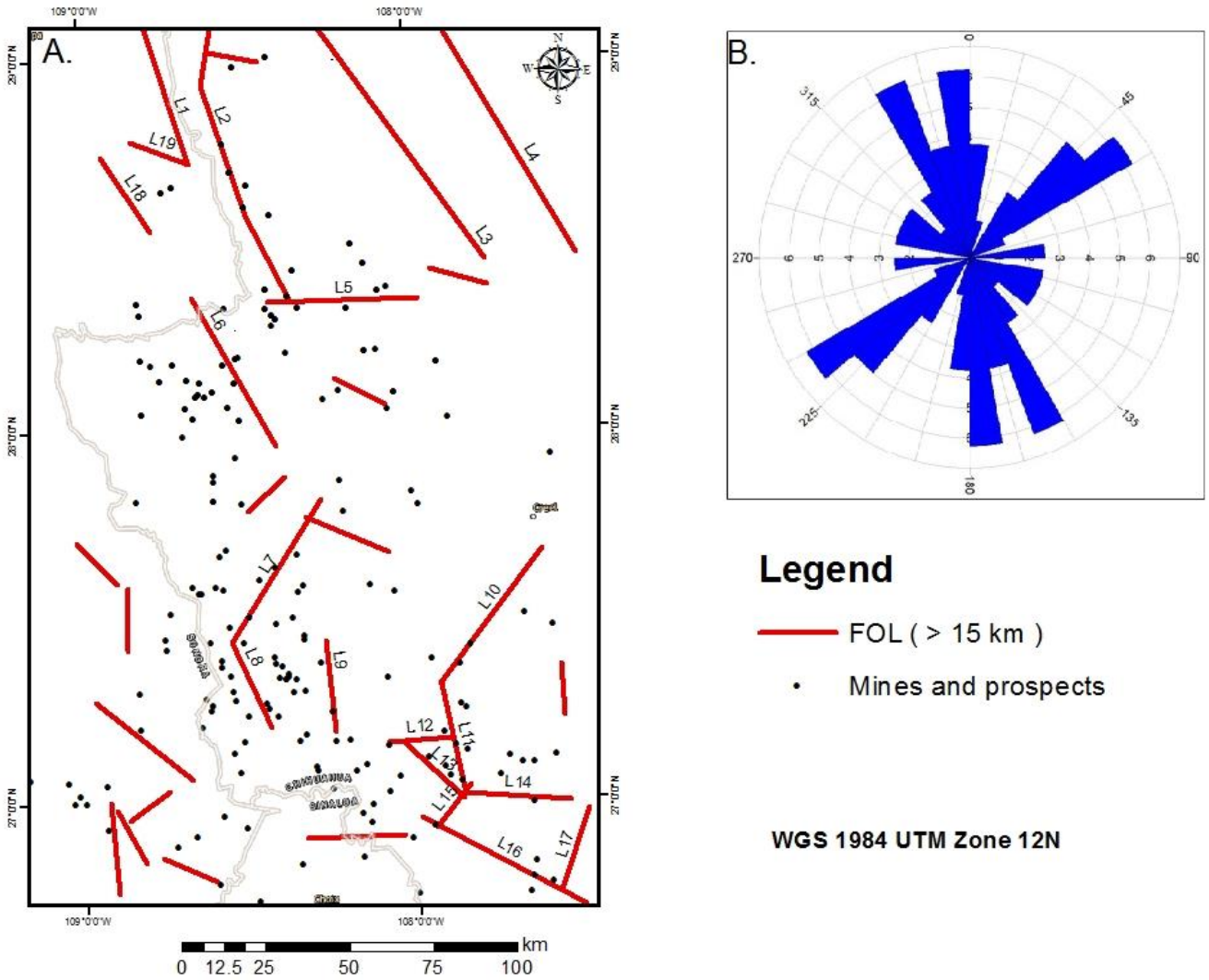

Figure 6: A. It shows the Frist Order Lineament (FOL), labels correlate with Table 1. B. Rose diagram for Frist Order Lineament.

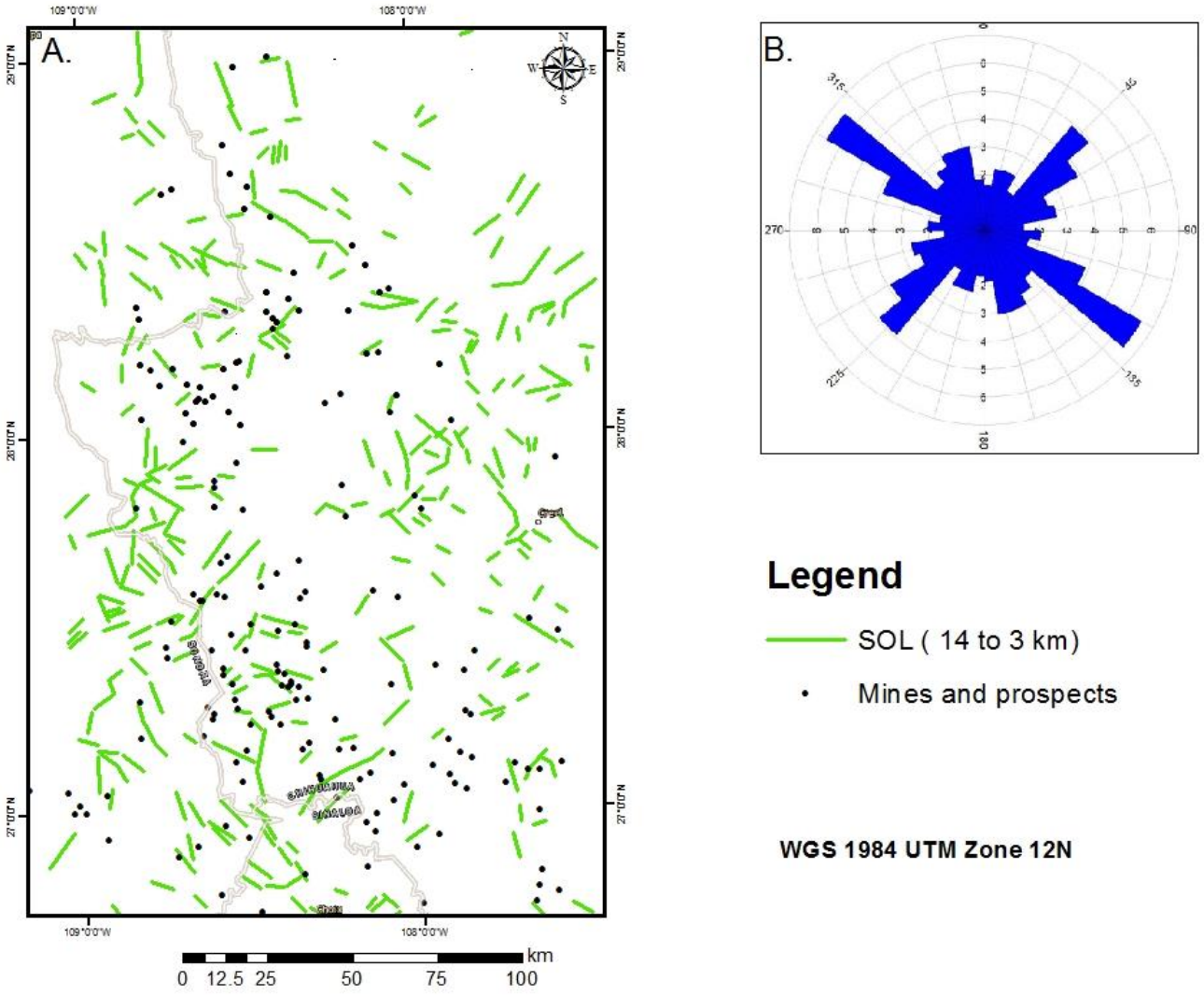

Figure 7: A. This map shows the Second Order Lineaments (SOL). B. Rose diagram for Second Order Lineament.

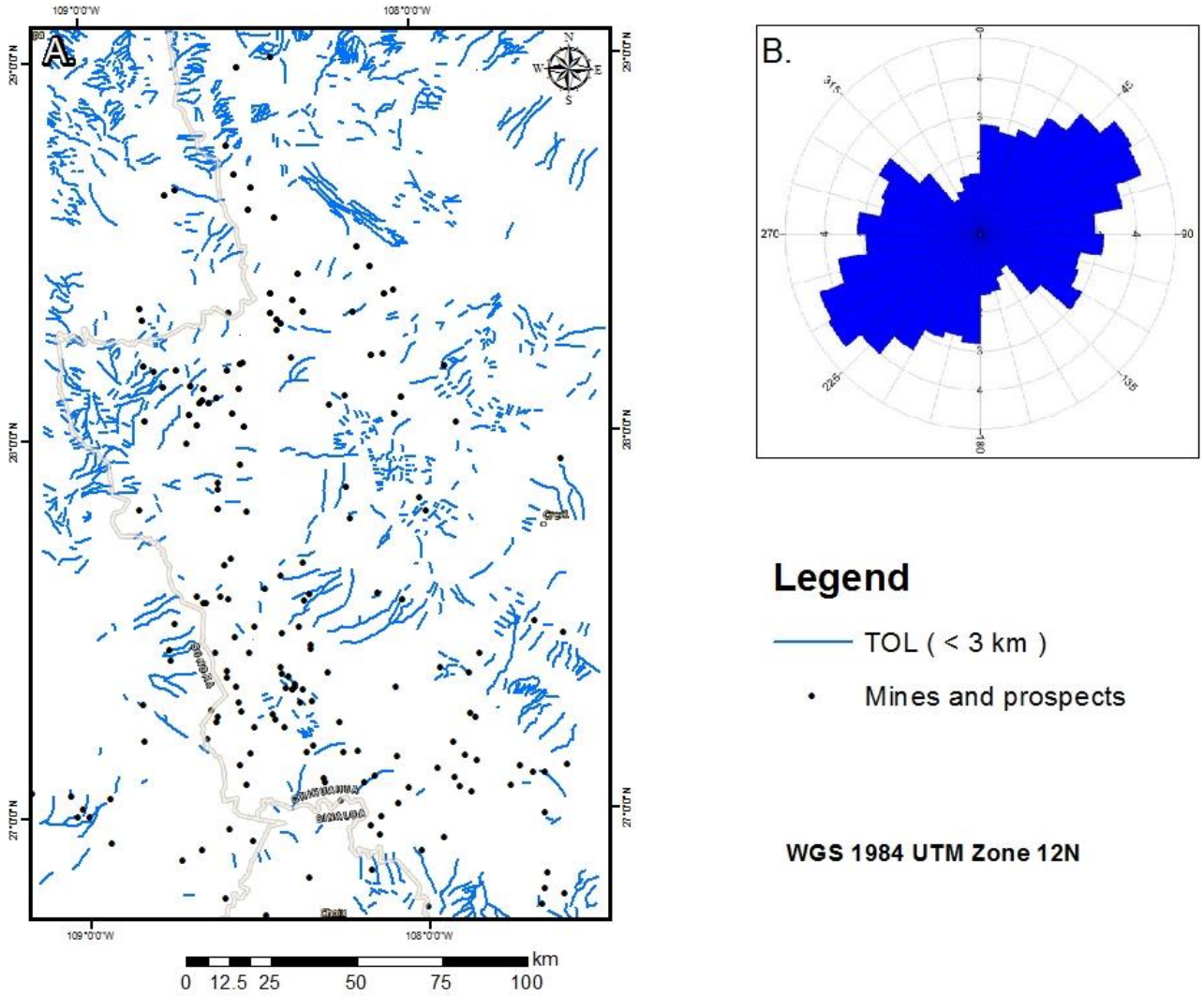

Figure 8: A. This map shows the Third Order Lineaments (TOL) B. Rose diagram for Third Order Lineament

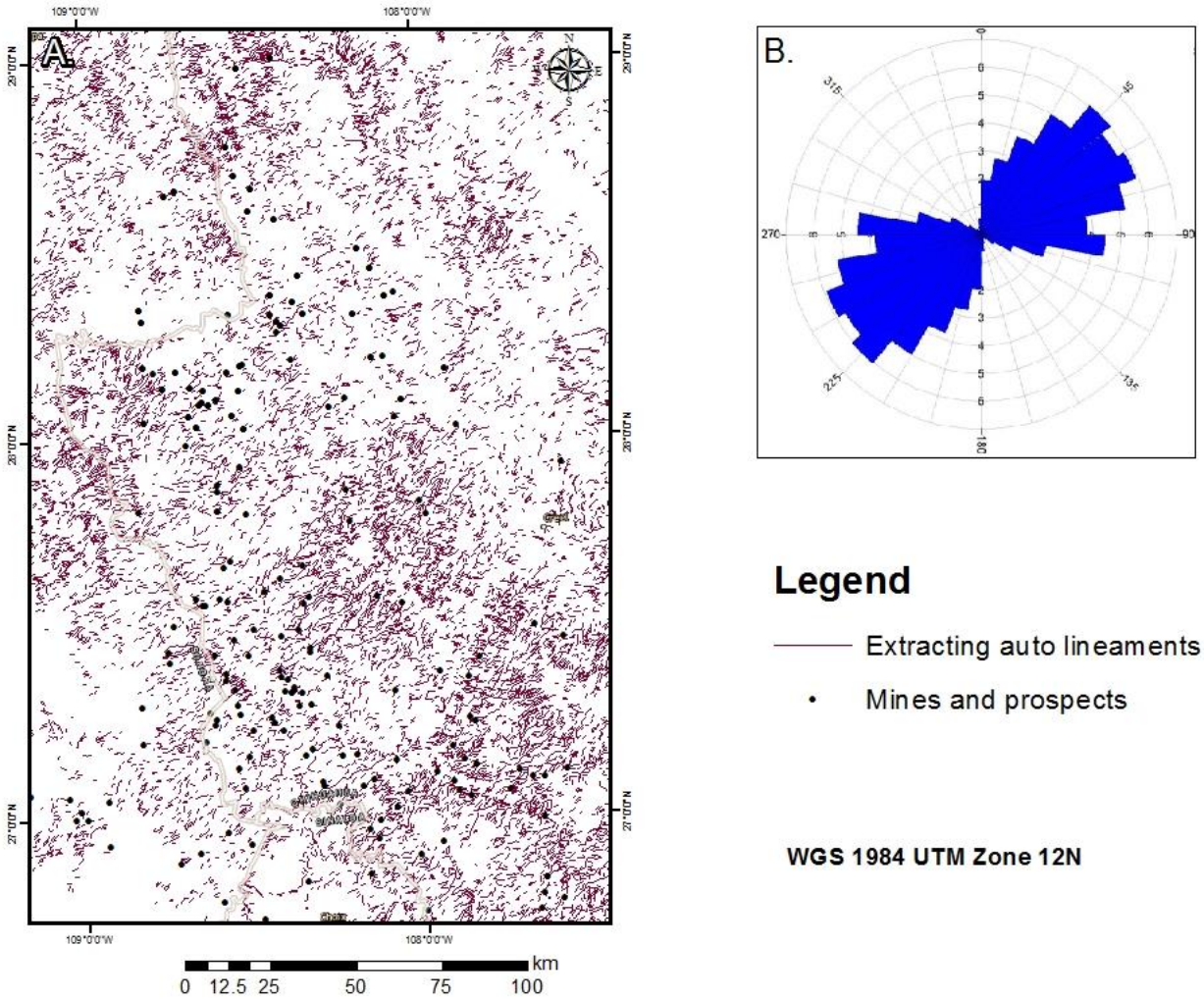

Figure 9: A. This map shows the lineaments automatic extraction in the area of interest which produced by LINE module of PCI Geomatics from Landsat 8. B. Rose diagram for automatic lineaments extracted.

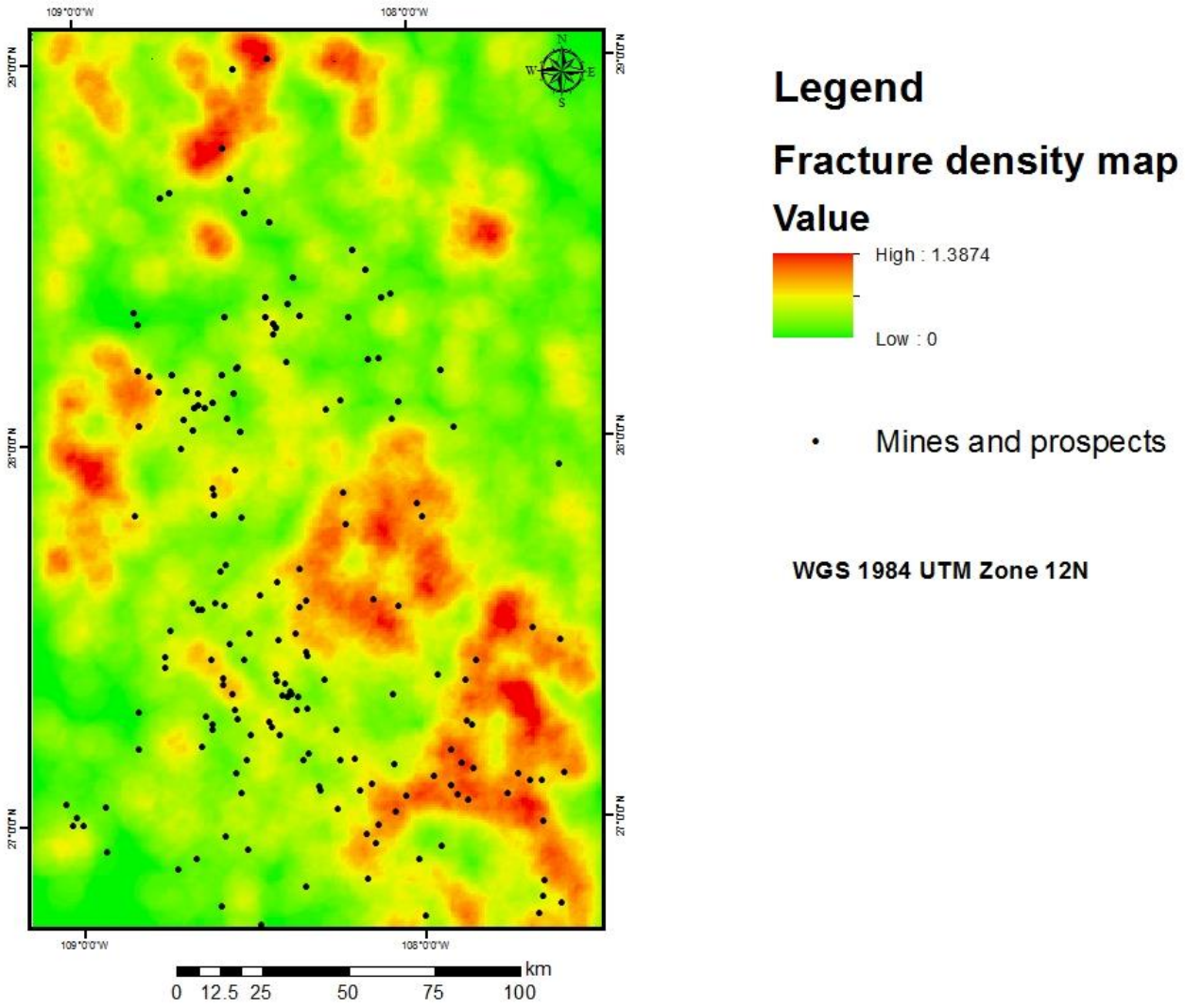

Figure 10: Map of the density of the lineaments in this region the red color shows more lineaments while the dark green shows the less fractures.

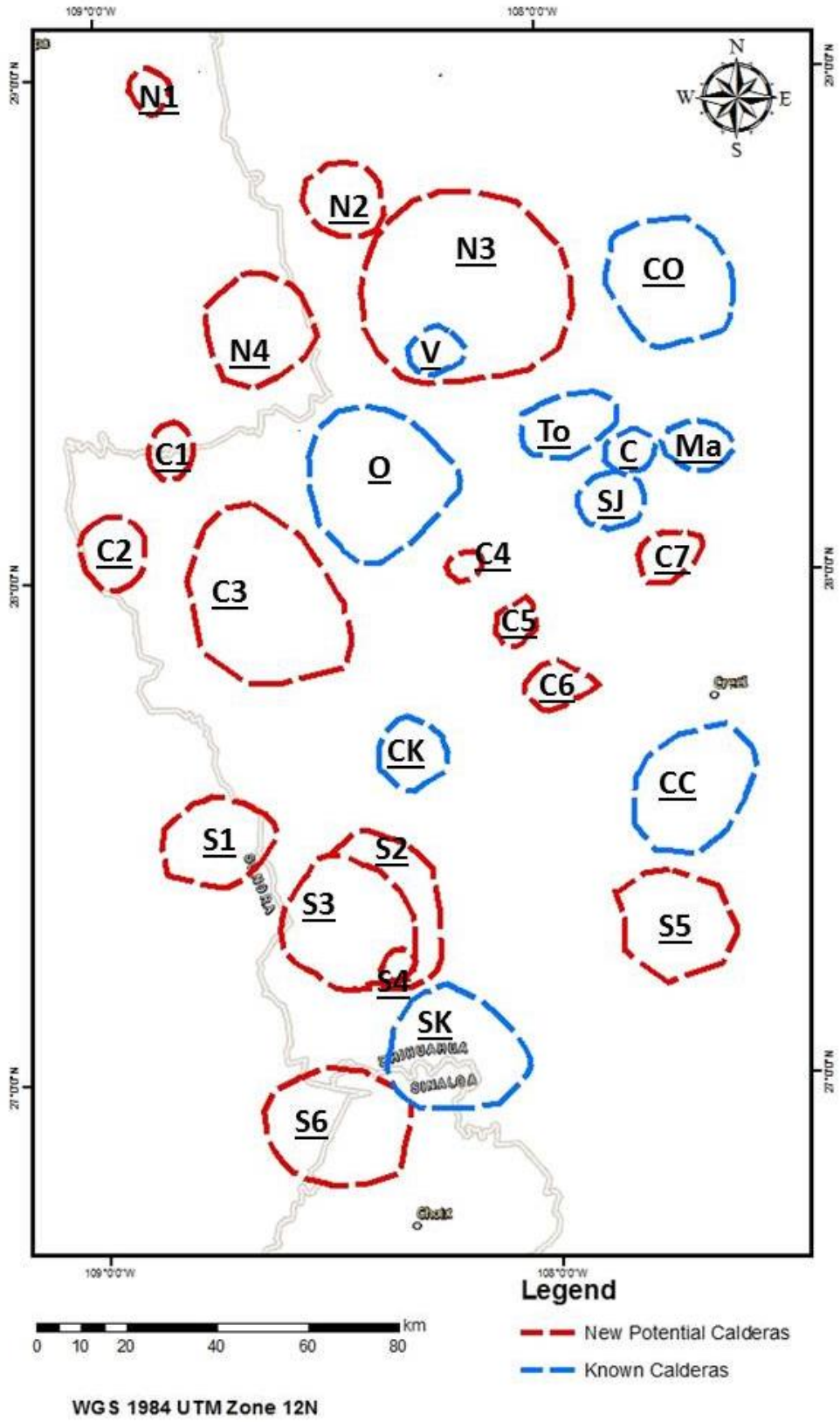

Figure 11: The map shows the knowing calderas from ((Swanson and McDowell, 1984; Wark et al., 1990; Ferrari et al., 2007; Murry et al., 2013) and the new potential calderas, see (Tables 3 and 4) for more details .

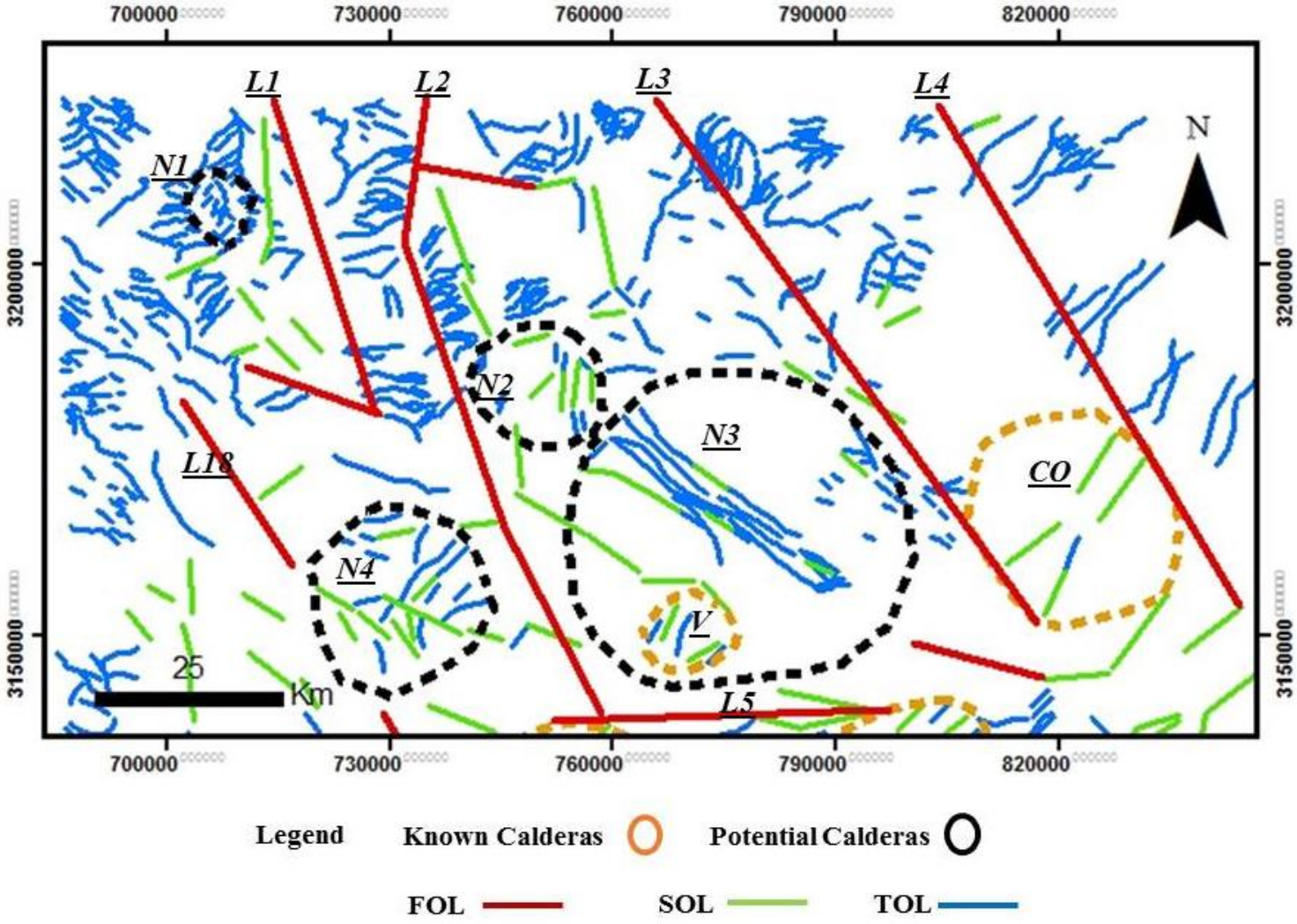

Figure 12: This map shows the north region of the area of interest with known calderas, potential calderas, mineral occurrences, Frist Order Lineament (FOL), Second Order Lineament (SOL), and Third Order Lineament (TOL), see (Tables 3 and 4) for more details.

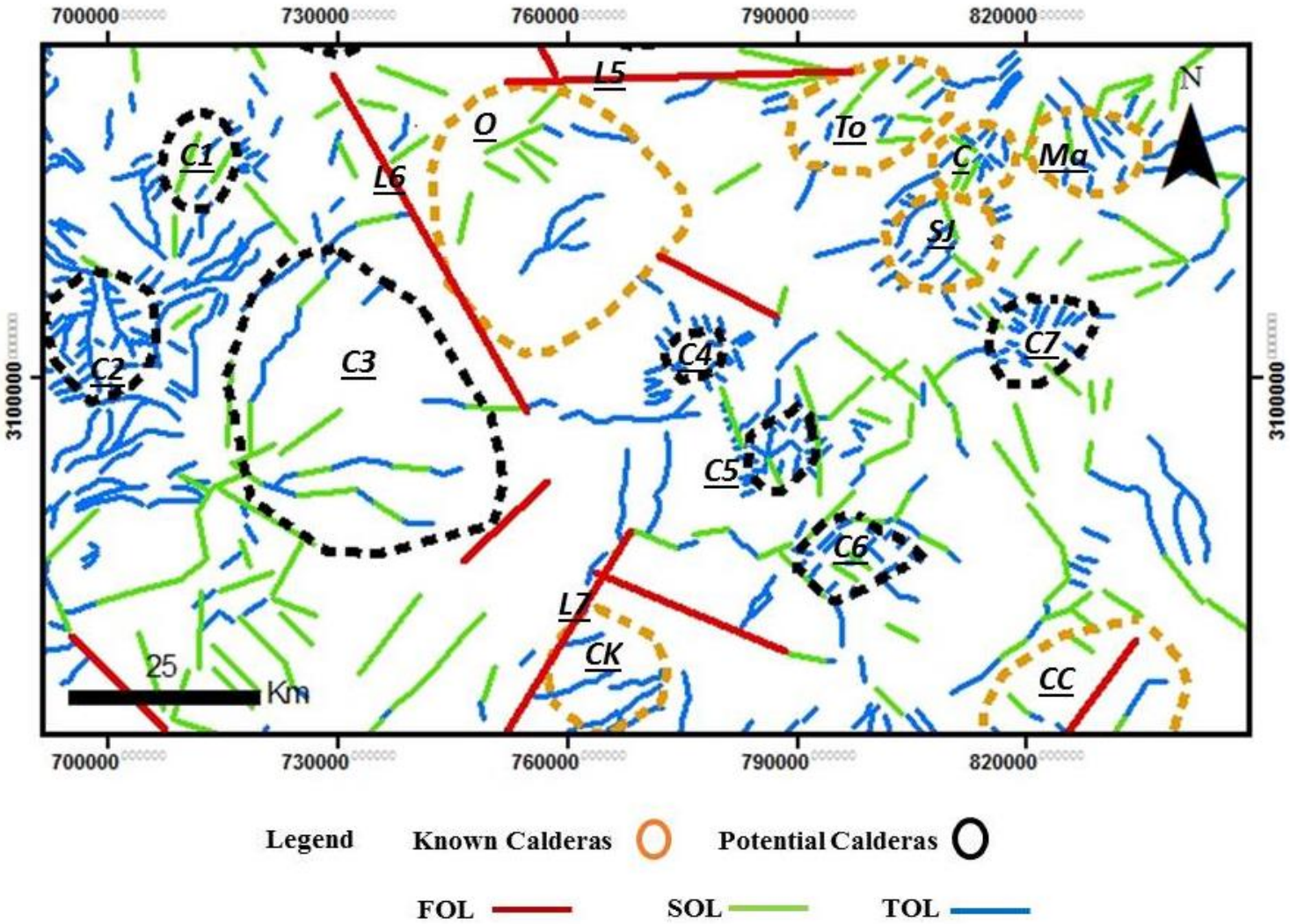

Figure 13: This map shows the center region of the area of interest with known calderas, potential calderas, mineral occurrences, Frist Order Lineament (FOL), Second Order Lineament (SOL), and Third Order Lineament (TOL), see (Tables 3 and 4) for more details.

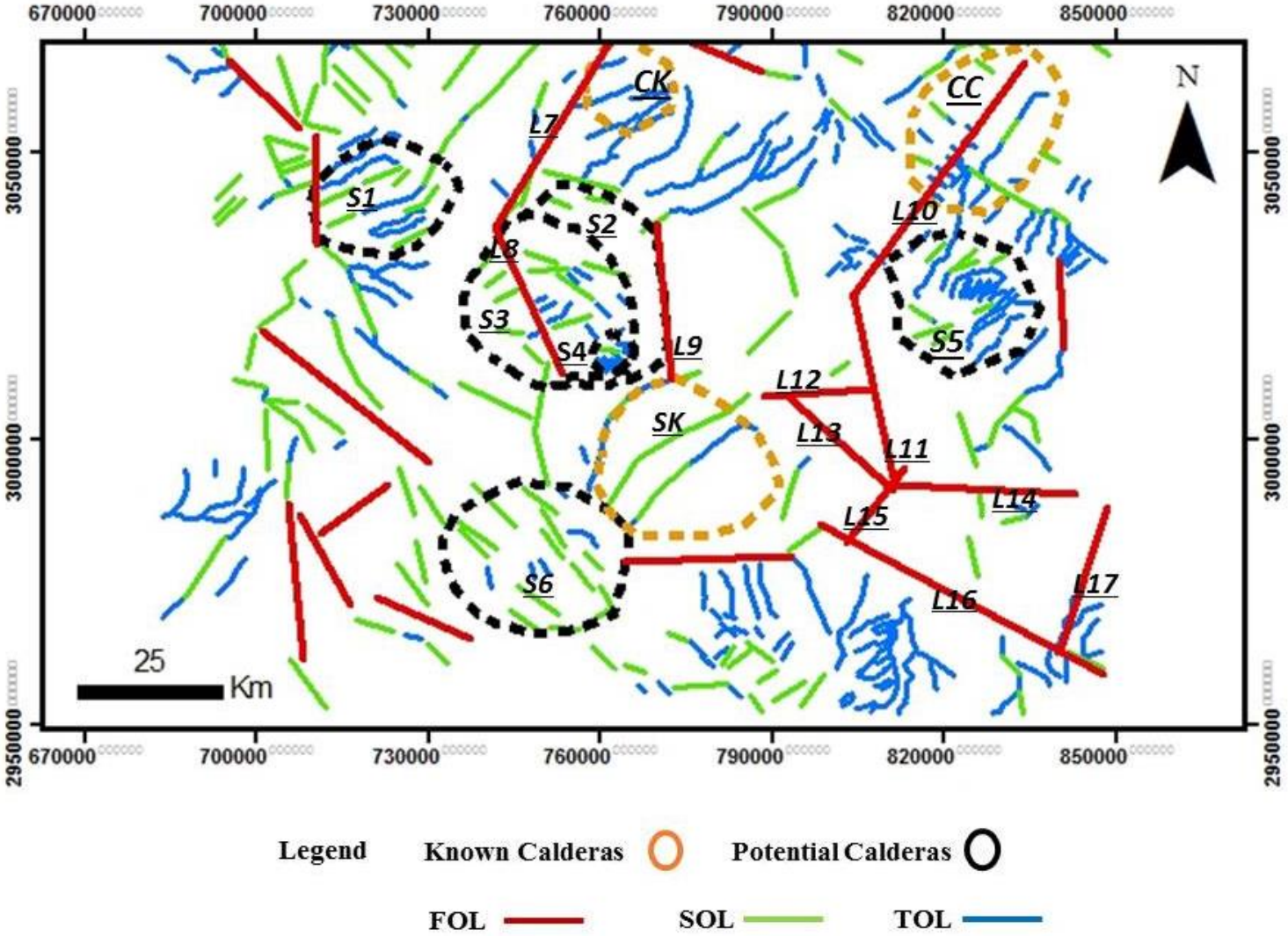

Figure 14: This map shows the south region of the area of interest with known calderas, potential calderas, mineral occurrences, Frist Order Lineament (FOL), Second Order Lineament (SOL), and Third Order Lineament (TOL), see (Tables 3 and 4) for more details.

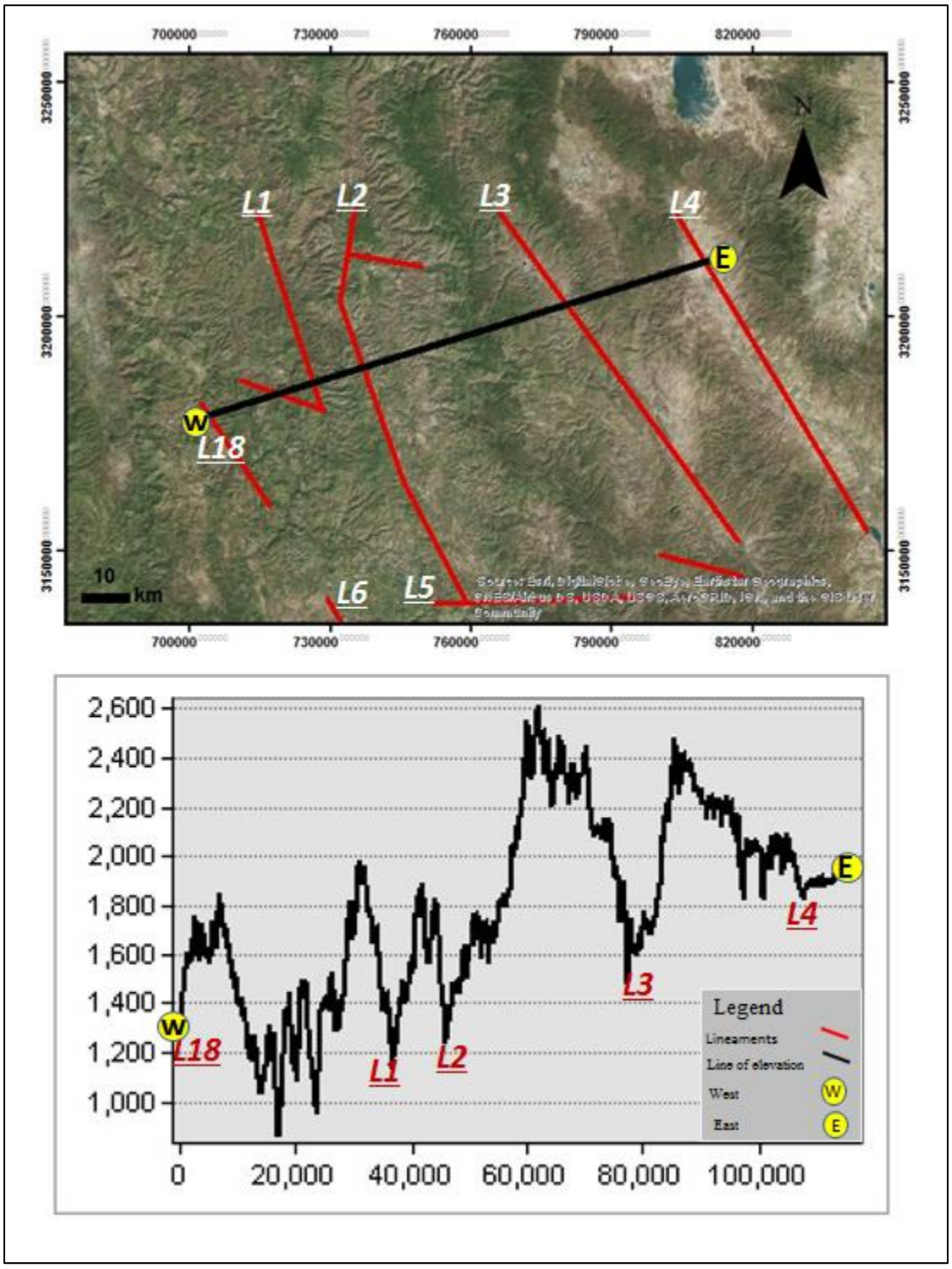

Figure 15: This figure shows the north lineaments in the northern region (L18, L1, L2, L3, and L4) with an elevation profile. The grabens are narrow, except for the one on L4.

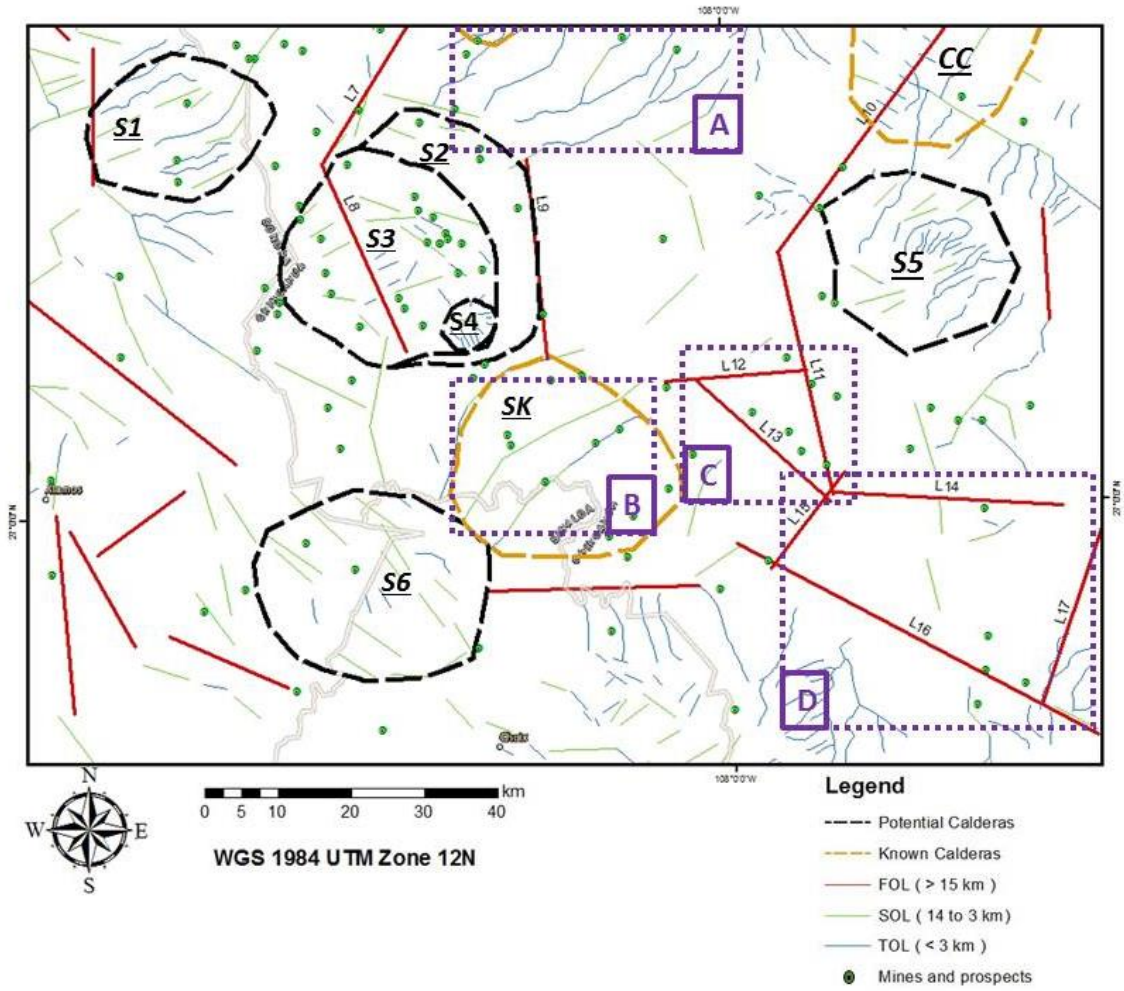

Figure 16: Squares A and B show the lineaments on the north and south of Palmarejo calderas (S3 and S4). Square C shows the interaction lineaments. Square D shows the Cuenca de Oro pull part basin.

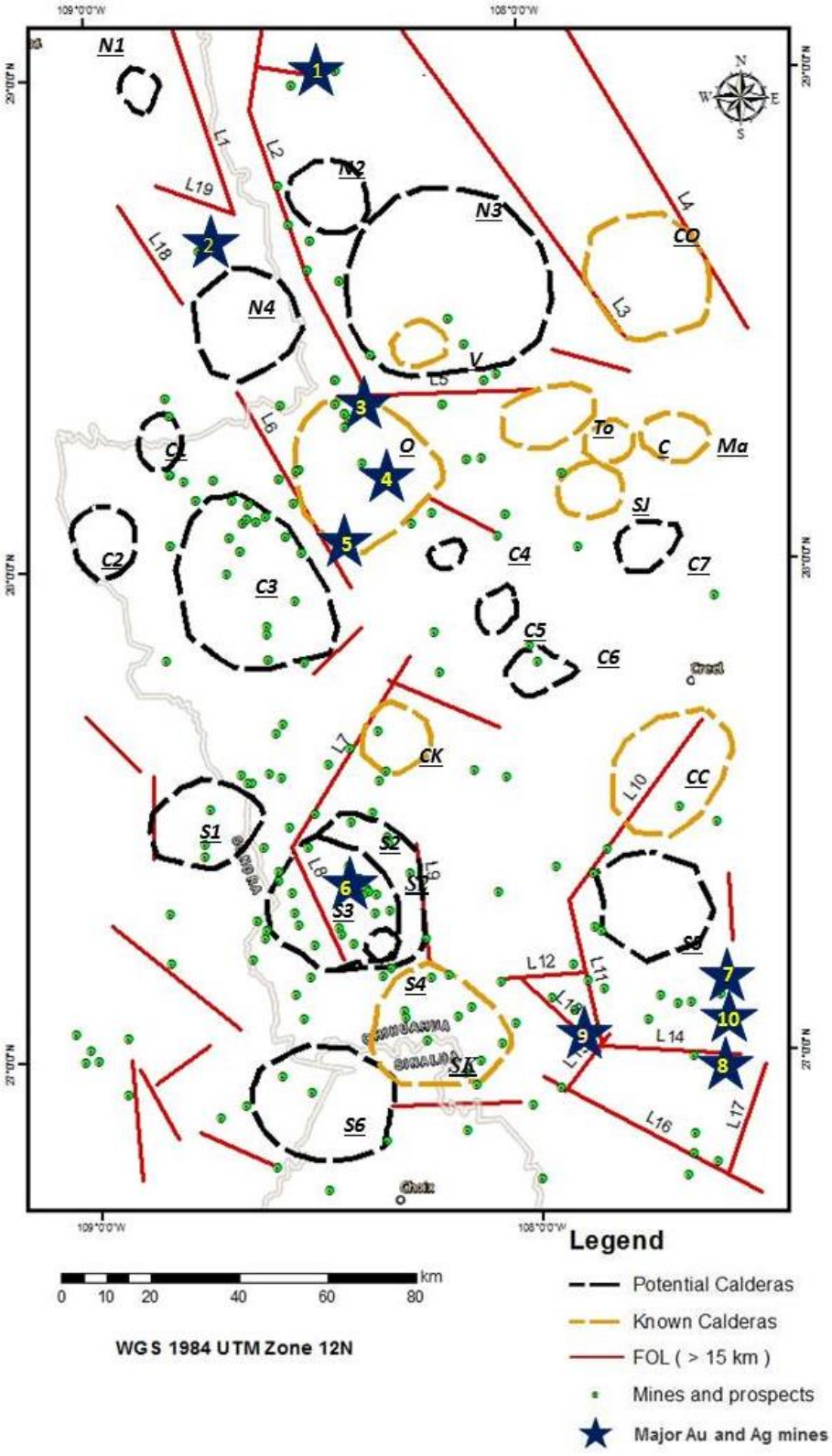

Figure 17: This map shows the major mines and mineral occurrences with First Order Lineament (FOL) and calderas in the area of interest.

CHAPTER 2: TARGETING ALUNITE IN EPITHERMAL AND COPPER PORPHYRY DEPOSITS USING ASTER IMAGERY IN THE NORTHERN SIERRA MADRE OCCIDENTAL, SONORA, MEXICO

ABSTRACT

In this work, a new method is applied to target alunite. This method can help detect gold mineralization in large areas such as the Sierra Madre Occidental where rugged topography has limited access to certain areas. This technique can help to distinguish alunite ($KAl_3(SO_4)_2(OH)_6$) from clays, iron oxides (Fe_2O_3, Fe_3O_4 or FeO[OH] and jarosite ($KFe_3[OH]_6[SO_4]_2$). This technique can be used to discover epithermal and porphyry deposits during regional exploration efforts. This is important for exploration companies since ASTER (Advanced Spaceborne Thermal Emission and Reflection Radiometer) satellite imagery is a cheap and widely available dataset. Several sites in the area of interest have been identified to be good targets for exploration.

1. INTRODUCTION

Multispectral imaging can be an essential resource for preliminary mineral exploration projects because of the advances in remote sensing techniques. Earlier studies have shown the ability to detect hydrothermal clays with multispectral images (Clark et al., 1993; Clark and Swayze, 1996; Rowan and Mars, 2003; Mars and Rowan, 2006). Alunite is a sulfate mineral that is found in the argillic alteration zones of porphyry and epithermal mineralization systems. Because of this, it can be used as a regional proxy to locate potential economic deposits. However, a weakness of most previous studies to map alunite with multispectral remote sensing data (e.g., Clark et al., 1993; Clark and Swayze, 1996; Rowan and Mars, 2003; Mars and Rowan, 2006; Standart, 2014) has been the inability to reliably

distinguish alunite from clays, iron oxides, jarosite, and quartz. The technique presented here can differentiate alunite from these minerals and is shown to be effective in mapping potential alunite in rugged areas such as the Sierra Madre Occidental of Mexico.

2. OBJECTIVE

The objective of this study is to target alunite, which can be a guide to gold mineralization in the northern Sierra Madre Occidental, Chihuahua Mexico.

3. BACKGROUND

3.1. Location

The study area is the northern Sierra Madre Occidental, approximately 55 km west of the Sonora-Chihuahua border and 100 km south of the Arizona-Sonora border (Figure 1). The study area is 120 km × 60 km.

3.2. Geology of the Sierra Madre Occidenta

Sierra Madre Occidental (SMO) was formed because of different magmatic and tectonic episodes during the Cretaceous - Cenozoic times that are associated with the subduction of the Farallon plate beneath the western North American plate, evolving to the opening of the Gulf of California, by the Baja rift (McDowell and Clabaugh, 1979; Atwater, 1988; Aguirre-Dıaz and McDowell, 1991; Aguirre-Dıaz and Labarthe-Hernandez, 2003; Swanson et al., 2006). It starts from a location just south of the Arizona, USA –Sonora, Mexico, border, and it extends 1800 km to the south until Guadalajara, in west-central Mexico. It differs in elevation from 200 m to about 3000 m.

Most of the surfaces of the SMO constitute two rock units which are the Lower Volcanic Series (LVS) and the Upper Volcanic Series (UVS).

LVS is an andesitic rock family formed above a subduction zone during compressive, tectonic events known as the Laramide, (Ferrari et al., 2000), which two regional pulses, 80 Ma, and 60 to 45 Ma (Aguirre-Díaz and McDowell, 1991; Ferrari et al., 2007).

The UVS is rhyolitic ash-flow tuffs issued from large calderas. They are emplaced during two pulses, one in the Oligocene (ca. 32–28 Ma) and the other in the Early Miocene (ca. 24–20 Ma) (Ferrari et al., 2007). The UVS is younger and formed through trans-tension, or transform - lateral, faulting, and extension (McDowell and Keizer, 1977; McDowell and Clabaugh, 1979; Aguirre-Díaz and McDowell, 1991, 1993).

Mineralization is superimposed upon these geologic features and the SMO as 1) porphyry Cu, Cu-Au, and Cu-Mo, in the LVS and of Laramide age, 2) skarns are associated with the porphyry episode, and 3) epithermal precious metal deposits in lateral and listric faults hosted in the LVS and UVS. Epithermal deposits are part of one of the larger precious metal mineral belts or zones of the world. It is known variously as the Northern Sierra Madre Precious Metal Belt (NSMPMB) (Wisser, 1966; Clark, 1982). Mineralization ages were from Eocene to Oligocene (Clark et al., 1982; Staude, 1995; Sellepack, 1997; Staude and Barton, 2001; Camprubí et al., 2003; Bryan et al., 2008).

3.3. Porphyry Copper and Epithermal Deposits

Porphyry copper and epithermal deposits are related to hydrothermal alteration and include minerals such as alunite, clays, and iron oxides (Sillitoe and Hedenquist, 2003; Robert et al., 2007). Porphyry copper deposits form at depths of 1–6 km below the surface due to magmatic-hydrothermal phenomena related to the emplacement of intermediate and felsic intrusive complexes (Seedorff et al., 2005).

Epithermal deposits are a type of hydrothermal deposit that occurs at shallow depths and low temperatures (50-300°C; Guilbert and Park, 2007). Epithermal deposits have the tendency to be eroded away because they occur at shallow depths in tectonically active regions (Guilbert and Park, 2007). The alteration in epithermal deposits can extend for long distances in high porosity and high permeability host rocks that allow hot meteoric fluids to flow readily.

Alunite, chlorite, sericite, zeolites, clays, adularia, and silica are the major alteration products in porphyry copper and epithermal deposits (Guilbert and Park, 2007). In both porphyry copper and epithermal deposits, these minerals are formed by potassic-propylitic; alkali metasomatic; and phyllic-argillic, hydrolytic alteration processes (Buchanan, 1981; Mars and Rowan, 2006; Figure 2).

3.4. Previous Satellite Remote-Sensing Studies

Mineral resource studies have been utilizing remote-sensing data analysis since the development of the multispectral imagery method after later, 1970s. The capability to study vast, previously unreachable areas was achieved in 1972, following the launch of the first Earth Resources Technology Satellite (ERTS-1), now known as Landsat 1. Landsat 1 provided the first widely-available satellite multispectral imagery, and a vast number of researchers have used data from the Landsat 1 Multispectral Scanner (MSS; 79 m/pixel) to map structures associated with porphyry copper deposits, such as regional structural lineaments and geomorphological manifestations of intrusive bodies (Raines, 1978; Rowan and Wetlaufer, 1981; Abrams and Brown, 1984; Abrams et al., 1983). However, the only mineralogical information that can be retrieved from MSS data is the spectral signatures of anomalously limonitic rocks (Figure 3A; Rowan et al., 1974; Schmidt, 1976; Krohn et al., 1978; Raines, 1978).

The introduction of the Landsat Thematic Mapper (TM) on the Landsat 4 spacecraft improved the available spatial resolution to 30 m/pixel and extended the spectral range further into the SWIR region by providing additional bands at 1.65 μm and 2.20 μm. The TM band centered at 2.20 μm (band 7) was included because field and laboratory reflectance measurements indicate that many hydrous, carbonate, clay, and sulfate minerals demonstrate spectral absorption qualities at this particular wavelength because of the vibrational processes that occur at the molecular level (Figure 4; Hunt and Salisbury, 1970).

An experiment that took place in Cuprite, Nevada (Abrams et al., 1977) proved that spectral absorption characteristics can be utilized for delineating exposed rocks that were affected by hydrothermal processes, such as bleaching and opalization, to form argillic and advanced argillic alteration (Abrams et al., 1977).

The prominent absorption at 2.20 μm due to this alteration can be highlighted in ratio images using TM band 7 and TM band 5 (7.65 μm) (Rowan and Mars, 2003). However, the width of TM band 7 can lead to critical ambiguities. For example, it is challenging to see the difference between hydrothermally altered rocks that include kaolinite and alunite (with absorption features at 2.17 and 2.2 μm, respectively) and carbonate rocks that contain minerals like dolomite and calcite (with absorption features at 2.33 and 2.32 μm, respectively) because they all manifest absorptions in TM band 7 (Mars and Rowan, 2006; Bishop, 2005; Figure 3A).

The ASTER SWIR subsystem has additional spectral bands (one at 1.65 μm and five in the 2.10–2.45 μm range) that afford the spectral resolution needed to discriminate between the absorption features diagnostic of CO_3^{2-}, Mg-OH, Al-OH, and H-O-H (Figure 3A; Rowan and Mars, 2003). Using ASTER, several researchers have managed to identify not only singular minerals, including dolomite, calcite, and muscovite, but also mineral groups (Rowan and Mars, 2003; Rowan et al., 2003).

3.5. Argillic Logical Operators

To regionally delineate hydrothermally altered rocks that are common in porphyry copper and epithermal deposits, Mars and Rowan (2006) utilized the method of logical operators. These are mathematical expressions that are used for comparing several band ratios to predetermined threshold values. The values and the ratios are selected following the examination of reflection/absorption strengths and/or the slopes of specific spectral characteristics associated with the target material in its reflectance spectra.

Single band-ratio-to-threshold comparisons get linked together by a sequence of Boolean operators, such as THEN, OR, IF, AND, and NOT. As a result, the operator makes a digital image consisting of ones and zeroes. A zero corresponds to cases when a pixel does not pass any of the Boolean tests, and a one emerges when a pixel passes all of them. In the final byte image, the zeroes are called "a mask" due to the absence of pixels in that location.

The ones mark the pixels that meet all the criteria of the logical operator and indicate pixels with spectra consistent with the target mineral. Mars and Rowan (2006) describe a logical operator that was created to mask shadows and vegetation and highlight argillic or phyllic alteration minerals, such as sericite, kaolinite, and alunite.

The following logical operator was used by Mars and Rowan (2006) to distinguish argillic from phyllic alterations:

$$\left(\left(\frac{band3}{band2}\right) \leq 1.35\right) \& (band4 > 260) \& \left(\left(\frac{band4}{band5}\right) > 1.25\right) \& \left(\left(\frac{band5}{band6}\right) \leq 1.05\right) \& \left(\left(\frac{band7}{band6}\right) \geq 1.03\right) \quad (1),$$

where the & symbol is the Boolean operator AND. In Equation (1), the first expression is the vegetation mask, and it utilizes the ratio of ASTER band 3 to ASTER band 2 to point out the "red edge", the distinct spectral signature of vegetation in the visible-near infrared (VNIR), (Birth and McVey, 1968; Cohen, 1991; Colombo et al., 2003; Mars and Rowan, 2006). The presence of the red edge indicates a steep increase in the reflectance of healthy photosynthesizing vegetation in the near infrared (~0.7 μm; ASTER band 3) compared to the visible red (~0.6 μm; ASTER band 2). By comparing image reflectance spectra to a spectral library, Mars and Rowan (2006) established that no vegetation is present in an area if the ASTER band 3/2 ratio value is less than 1.35.

In Equation (1), the second expression masks dark pixels, such as mafic rocks and shadows, by exploiting a defect in the ASTER instrument (Rowan and Mars, 2003; Mars and Rowan, 2006). An engineering defect allows light to leak from the ASTER band 4 optical path into the optical paths for ASTER bands 5 and 9 (Mars and Rowan, 2006). This

phenomenon is referred to as cross-talk, and results in pixels with a low ASTER band 4 reflectance will demonstrate unusually high reflectance values in ASTER bands 5 and 9 (Mars and Rowan, 2006). Although ASTER bands 6 and 8 are not directly affected by the cross-talk, high reflectance values in the bands 5 and 9 will lead them to demonstrate deceptively deep absorption characteristics (Mars and Rowan, 2006). Mars and Rowan (2006) empirically determined that ASTER band 4 values of less than 260 predict pixels that may be severely impacted by the cross-talk defect.

The third, fourth, and fifth expressions in Equation (1) were used by Mars and Rowan (2006) to delineate the 2.17-2.20 μm absorption that shows the presence of OH^- in kaolinite and alunite, as well as to distinguish between the argillic (kaolinite and alunite) and phyllic (sericite) alteration areas. Knowing that the OH^- absorption in the reflectance spectrum of sericite is within ~0.05 μm of that in the reflectance spectra of kaolinite and alunite (Figure 5), Mars and Rowan (2006) found the correct band ratio for distinguishing the three minerals. Mars and Rowan (2006) used the ASTER spectra of kaolinite and alunite (Figure 5) to establish that the presence of these argillic components makes the reflectance at ASTER band 4 25% higher than the reflectance at ASTER band 5. Thus, an ASTER band 4/5 ratio value greater than 1.25 will point out the 2.17 μm absorption feature associated with argillic alteration (Figure 5). In addition, Mars and Rowan (2006) also established that the reflectance at ASTER band 5 is 5% lower than that at ASTER band 6 in argillic rocks. Thus, an ASTER band 5/6 ratio value lower than 1.05 can distinguish argillic alterations from phyllic ones (Fig.5). Finally, Mars and Rowan (2006) discovered that reflectance at ASTER band 7 is 3% higher than that at ASTER band 6 for argillic rocks. Thus, an ASTER band 7/6 ratio value is greater than or equal to 1.03 will indicate the 2.20 μm absorption feature associated with argillic alteration (Figure 5).

The disadvantage of the argillic logical operator used by Mars and Rowan (2006) in Equation (1) has been its failure to discriminate between alunite and iron sulfates, clays, carbonates, iron oxides, and vegetation (Clark et al., 1993; Clark and Swayze, 1996; Rowan and Mars, 2003; Mars and Rowan, 2006; Standart, 2014). The reason for this is that the ~2.25-μm OH^- absorption in both limestone and jarosite is very similar to the 2.20-μm OH^- absorption in alunite (Rowan and Mars, 2003; Bishop and Murad, 2005). Apart from limestone and jarosite, the argillic operator might also erroneously indicate clays that have similar 2.20-μm absorptions, such as montmorillonite and illite, which are regularly found in alluvium, although, are not related to alunite. Knowing this, it is possible to use as an alternative a logical operator that is sensitive to the 9 μm (thermal infrared, TIR) absorption that indicates the presence of SO_4^{2-} in alunite (Bishop and Murad, 2005; Standart, 2014). However, using this logical operator might also result in the erroneous inclusion of quartz and carbonate because they also have prominent 9-μm absorptions (Figure 3B) (Rowan and Mars, 2003).

Another option is to focus on the SWIR spectral range between 0.8 μm and 1.65 μm, as shown in Figure 6. It is known that silicates and sulfates, such as goethite, hematite, limonite, and jarosite, demonstrate a positive spectral slope in the 0.8 μm to 1.65 μm range, while the spectral slope of alunite in this range is negative (Figure 6).

To minimize the risk of misidentification, it would be best to utilize a combination of alunite's unique spectral characteristics, such as the SWIR spectral slope, as well as the OH^- and SO_4^{2-} absorptions in the TIR (Standart, 2014).

4. DATA

The data used in this study comes from the the Advanced Spaceborne Thermal Emission and Reflection Radiometer (ASTER), an instrument on board the Terra satellite

(Abrams, 2002). ASTER is a multispectral instrument that includes 14 bands distributed among three subsystems (Table 1; Abrams, 2002; Mars and Rowan, 2006): the visible and near-infrared (VNIR) consisting of 3 bands ranging from 0.52-0.86 μm with a spatial resolution of 15 m per pixel; the shortwave infrared (SWIR) consisting of 6 bands ranging from 1.6-2.43 μm with a spatial resolution of 30 m per pixel; and the thermal infrared (TIR) consisting of 5 bands ranging from 8.125-11.65 μm with a spatial resolution of 90 m per pixel.

Two scenes were required due to the large area of interest: (ID#: 00308252005180903) and (ID#: 00308252005180912). They were both acquired by the ASTER instrument in August 2005 and are free of clouds. For these two scenes, the AST_07XT and AST_05 Level 2 image data products were obtained on-demand from https://search.earthdata.nasa.gov/search.

The AST_07XT product comprises two data files of surface reflectance in the both VNIR (3 bands; 15 m/pixel) and SWIR (6 bands; 30m/pixel) (Table 1)that are atmospherically corrected in addition to crosstalk-corrected (Thome et al., 1999; Iwasaki et al., 2002). The AST_05 product is a single data file containing surface emissivity in the TIR (5 bands; 90 m/pixel) obtained by performing both an atmospheric correction as well as temperature-emissivity separation (Gillespie et al., 1999).

5. METHODS

5.1. ASTER Preprocessing

The ASTER data first had to be "layer stacked" because the VNIR, SWIR, and TIR bands have different spatial resolutions (15 m/pixel, 30 m/pixel, and 90 m/pixel, respectively) (Fig.10). Because of this, they cannot be mathematically combined (i.e., band ratioed, etc.) without spatial resampling to a common resolution. Therefore, the AST_07XT SWIR bands and the AST_05 TIR bands were up sampled to match the 15-m resolution of the AST_07XT VNIR bands in order to preserve the original resolution of the data without loss. The spatial

resampling was done using the nearest neighbor method and the resulting stacked image file was projected to the WGS 84 datum and zone 12N in the Universal Transverse Mercator (UTM) coordinate system.

5.2. SO_4^{2-} Logical Operator

The deep and broad SO_4^{2-} absorption in alunite is present in the TIR at 9 μm ((Bishop and Murad, 2005; Standart, 2014); Figure 3A). This absorption can be used to distinguish alunite from clays which do not exhibit a 9-μm absorption. Nevertheless, carbonates and quartz also have 9-μm absorptions. Carbonates show a smaller 9 μm absorption compared to quartz and alunite (Rowan and Mars, 2003; Figure 3B). A band ratio targeting the deep 9-μm SO_4^{2-} aborption feature can avoid mapping carbonates. To map SO_4^{2-}, ASTER bands 12 (9.1 μm) and 13 (10.6 μm) are used in the following logical operator (the SO_4^{2-} operator) of Standart, (2014):

$$\left(\left(\frac{band3}{band2}\right) \leq 1.35\right) \& (band4 > 260) \& \left(\left(\frac{band13}{band12}\right) > 1.08\right) \qquad (2).$$

The first term in Equation (2) is the mask for vegetation. The second term is the cross-talk mask for dark pixels. The third term highlights alunite using the empirical observation that ASTER band 13 reflectance is ~8% greater than ASTER band 12 reflectance for pixels that contain alunite (Standart, 2014; Figure 7). Consequently, an ASTER band 13/12 ratio greater than 1.08 should determine sulfate-bearing minerals from carbonate and quartz (Mars and Rowan, 2006). However, the SO_4^{2-} logical operator will still map silicified rocks in addition to alunite and jarosite because quartz (Figure 7 and 8) also contains 9-μm absorption. The SO_{42-} operator is implemented in ENVI software using the "band math" function.

5. 3. OH^--FeO Logical Operator

To avoid mapping quartz, iron oxides (i.e., hematite, and limonite), and iron-sulfates (i.e., jarosite), an OH^--FeO logical operator of Standart, (2014) is used:

$$\left(\left(\frac{band3}{band2}\right) \leq 1.35\right) \& (band4 > 260) \& \left(\left(\frac{band4}{band3}\right) \leq 1\right) \& \left(\left(\frac{band4}{band5}\right) > 1.25\right) \& \left(\left(\frac{band5}{band6}\right) \leq 1.05\right) \& \left(\left(\frac{band7}{band6}\right) \geq 1.03\right) \quad (3).$$

The first two terms are the vegetation mask and dark pixel mask, respectively. The ASTER band 4/3 ratio in the third term is used to distinguish alunite from both iron oxides and sulfates by their spectral slope between ~1.65 μm and ~0.8 μm (Figure 5 and 6).

Hydrous iron sulfates and silicates (limonite, hematite, goethite, and jarosite) show a positive spectral slope between band 3 (0.8 μm) and band 4 (1.65 μm), whereas alunite displays as a negative slope (Figure 5 and 6) (Mars and Rowan, 2006). Therefore, pixels for which the ASTER band 4/3 ratio is less than or equal to 1 will have a spectral slope consistent with alunite (Standart, 2014).

The fourth, fifth and sixth expressions in Equation (3) map the 2.17-2.2-μm absorption associated with OH^- in alunite and kaolinite and differentiate argillic (i.e., alunite and kaolinite) alteration zones from phyllic (i.e., sericite) alteration zones (Mars and Rowan, 2006; Standart, 2014).

5.4. Alunite Map

The SO_4^{2-} and OH^--FeO logical operator maps are combined to produce an "alunite map." This is done by exporting the SO_4^{2-} and OH^--FeO logical operator maps from ENVI as TIFF image files (Figure 9). These TIFF files are then imported to ArcGIS and converted to shapefiles. The shapefiles preserve the locations that have binary 1 assignment in the SO_4^{2-} and OH^--FeO logical operator maps. The shapefiles are then logically combined with

the ArcGIS intersection tool to produce a single shapefile that shows the most probable locations of alunite (Figure 9).

5.5. Quartz Map

In some locations, the "alunite map" may erroneously target a mixture of quartz or jarosite with kaolinite in addition to (or instead of) alunite. To mitigate against this, a quartz index is used:

$$[band11/ (band 10 + band 12)] * (band 13 / band 12) \quad (4),$$

Equation (4) exploits the TIR emissivity features at ASTER bands 10 and 12 relative to bands 11 and 13. The index yields large values for pixels that have high emissivity in ASTER band 11 relative to the sum of the emissivities in ASTER bands 10 and 12, and it will large values for pixels that have high emissivity in ASTER band 13 relative to ASTER band 12 (Figure 8; Rockwell and Hofstra, 2008).

Equation (4) is implemented in ENVI using the "band math" function. The output is a floating point image, which is then converted into an unsigned 8 bit (0 to 255) image. Depending upon the histograms, the threshold value of a band ratio image can be defined using the equation (Fatima et al., 2017):

$$\text{Threshold} = \text{mean} + \text{standard deviation (confidence 92\%)} \quad (5).$$

Finally, the alunite map is subtracted from quartz map to be just alunite mineral.

5.6. Ground Truth Testing

Before targeting the alunite in the area of interest (Figure 1), two well-characterized areas that both contain alunite are used for quality control of this work. The ground truth sites are Cuprite Hills, Nevada (Rowan and Mars, 2003; Figure 10) and Chocolate Mountain, California (Zhang, 2007; Figure 11).

5.6.1 Cuprite Hills, Nevada, USA

The Cuprite Hills is a well-studied area that contains an abundance of hydrothermally-altered rocks that contain alunite (Ashley and Abram, 1980; Rowan and Mars, 2003; Mars and Rowan, 2006; Swayze et al., 2014). The Cuprite Hills are located 15 km south of Goldfield in southwestern Nevada (Figure 10). One ASTER scene was required to cover the whole Cuprite Hills area. It was acquired on August 24, 2001 (ID#: 00308242001185220). The result of the Standart (2014) method in this region as an alunite map is spatially correlative to alunite regions within the AVIRIS mineral map (Figure 10; Swayze et al., 2014).

5.6.2. Chocolate Mountain, California, USA

Chocolate Mountain (32.9°N, 115.1° W) is located in the southeast Chocolate Mountains in the eastern part of Imperial County, California, USA (Figure 11). It has been studied for mineral alteration, including alunite (Zhang, 2007), and is a significant gold province.One ASTER scene was required to cover the entire Chocolate Mountains. It was acquired on October 13, 2001 (ID#:00310132001183930). The alunite map produced with the technique described in this paper is spatially correlative to alunite regions within the ASTER minerals map (Zhang, 2007) (Figure 11). Several additional targets have been identified in the northwest of the map (Figure 11).

6. RESULTS AND DISCUSSION

After applying the method at Cuprite Hills and Chocolate Mountain as ground truth, we moved to area of interest at Northern Sierra Madre Occidental, Sonora, Mexico (Figure 1) and applied the alunite method. The result of the SO_4^{2-} logical operator in the area of interest is 5,257 polygons, which covers a total of 4.9 km2 (Figure 12). It could be alunite, jarosite or quartz. On the other hand, the OH^--FeO logical operator results in 892 polygons which cover a total of 0.76 km2 (Figure 12). This result shows the alunite, kaolinite or mixing of alunite

with kaolinite. The intersection of these two logical operators results in 735 polygons that cover a total of 0.67 km2 (Figure 13). The number of the results of alunite is close to the OH^--FeO logical operator results.

We map quartz to reduce the number of mixing of quartz with kaolinite, if they are present in the alunite result (Figure 14). Alunite polygons are subtracted from the quartz polygons if they are at the same location. The result of the alunite polygons after subtracting from quartz polygons is 509 polygons. The result of alunite polygons is reduced 31% from mixing of kaolinite, quartz or both (Figure 15). In the area of interest, some of the alunite is located at or nearby five mines and prospects: La Caridad, Pilares, San Nicolas (Nacozari), La Blanca mines, and La Bamboya prospect (Figure 15). Several locations of alunite are encouraging for exploration in this region, especially when they are nearby the mines or prospects or they are in higher elevation (Figure 15).

7. CONCLUSION

Several alunite locations will be explored in the area of interest where there are no actual mines or claims. These techniques will lead to more discoveries of epithermal and porphyry deposits as a result of increased regional exploration efforts enabled by new remote-sensing techniques. This is important for mining companies since ASTER is a cheap and widely available dataset. Using ASTER imagery and the method for finding alunite presented here as an initial platform for exploration projects will help junior and major mining companies alike plan sampling missions that may lead to the discovery of the next major porphyry or epithermal deposit.

Table 1: ASTER instrument characteristics (Abrams, 2002).

Subsystem	Band Number	Spectral Range (μm)	Spatial Resolution (m)
VNIR	1	0.52-0.60	15
	2	0.63-0.69	
	3N	0.78-0.86	
	3B	0.78-0.86	
SWIR	4	1.6-1.7	30
	5	2.145-2.185	
	6	2.185-2.225	
	7	2.235-2.285	
	8	2.295-2.365	
	9	2.360-2.430	
TIR	10	8.125-8.475	90
	11	8.475-8.825	
	12	8.925-9.275	
	13	10.25-10.95	
	14	10.95-11.65	

Figure 1: Map of the area of interest (120 x 60 km).

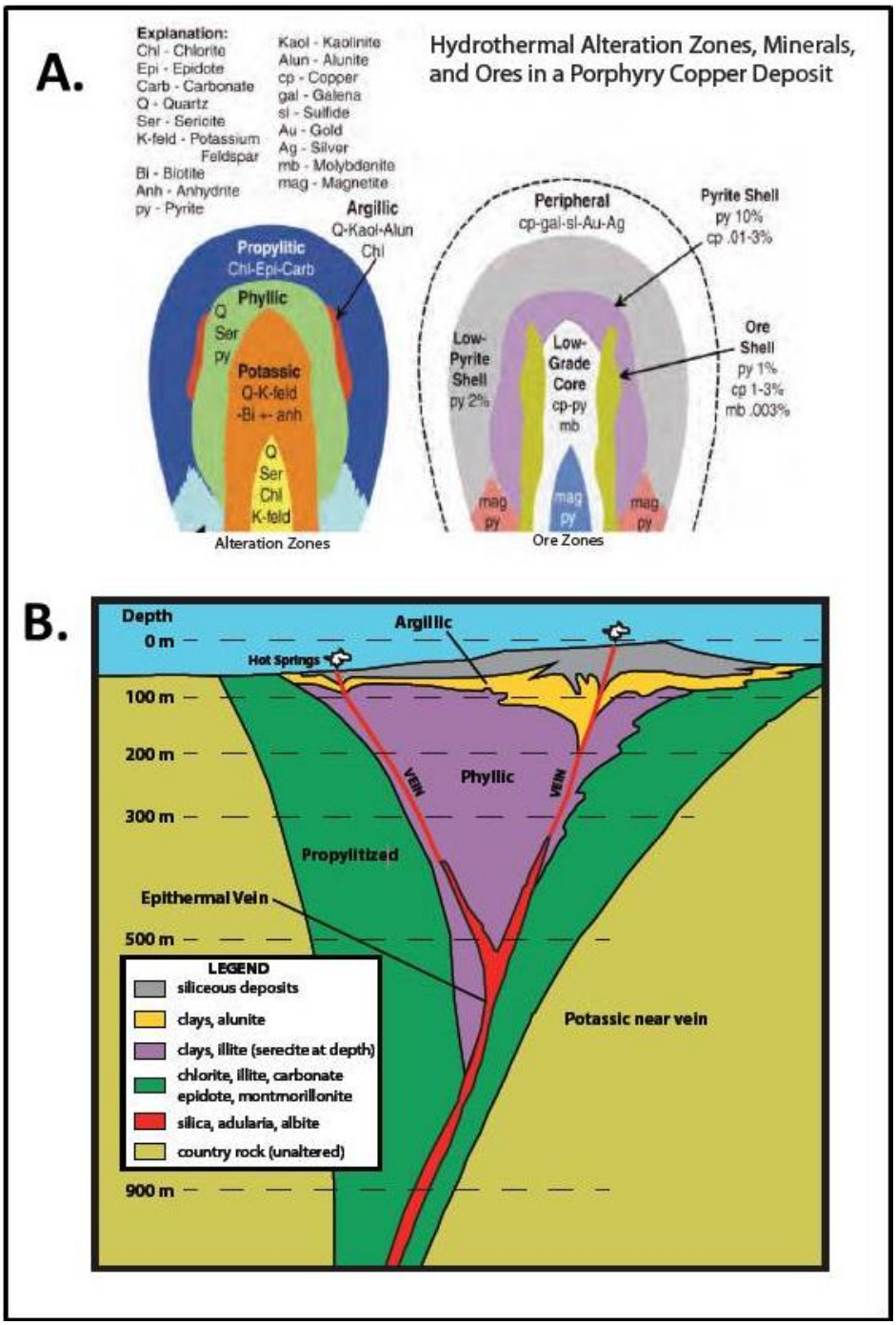

Figure 2: (A) Cross section of ores (right) associated with alteration zones (left) in a porphyry copper deposit (Mars and Rowan, 2006).(B) Cross section of epithermal deposit showing hydrothermal alteration minerals and types, including propylitic, phyllic, argillic, and potassic. Modified from Buchanan (1981).

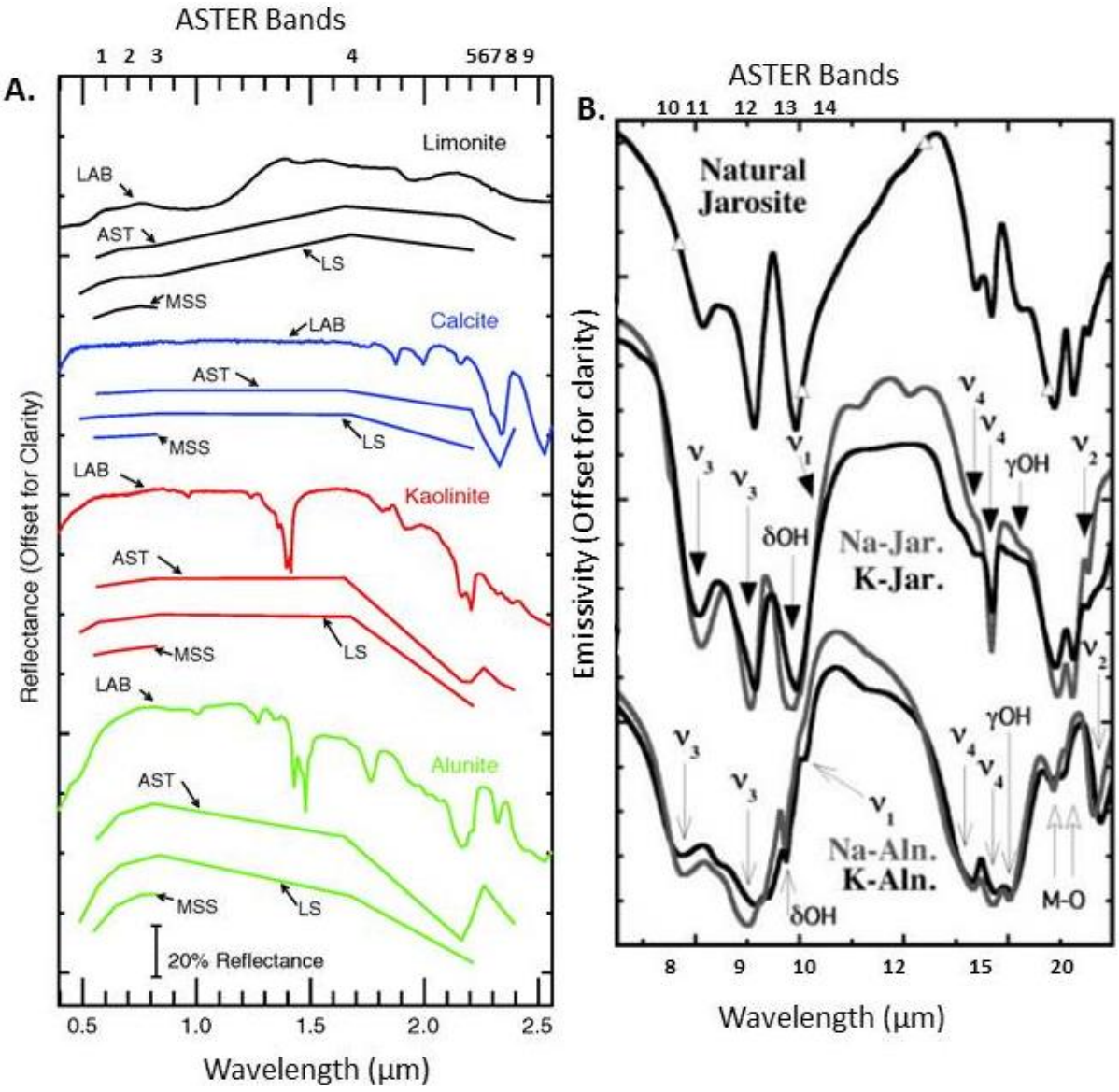

Figure 3: (A) laboratory reflectance spectra (LAB) of key minerals (Mars and Rowan, 2006). The doublet feature at 2.2 μm in alunite and kaolinite is used to distinguish it from other hydrous minerals. The spectra shown have been resampled to ASTER (AST), Landsat Thematic Mapper (LS) and Landsat Multispectral Scanner (MSS) bandpasses. The numbers across the top indicate ASTER band center positions. Modified from Mars and Rowan (2006). (B) Transmittance spectra of jarosite and alunite. SO_4^{2-} modes (ν_1, ν_2, ν_3, and ν_4) and OH- modes are displayed. Modified from Bishop (2005).

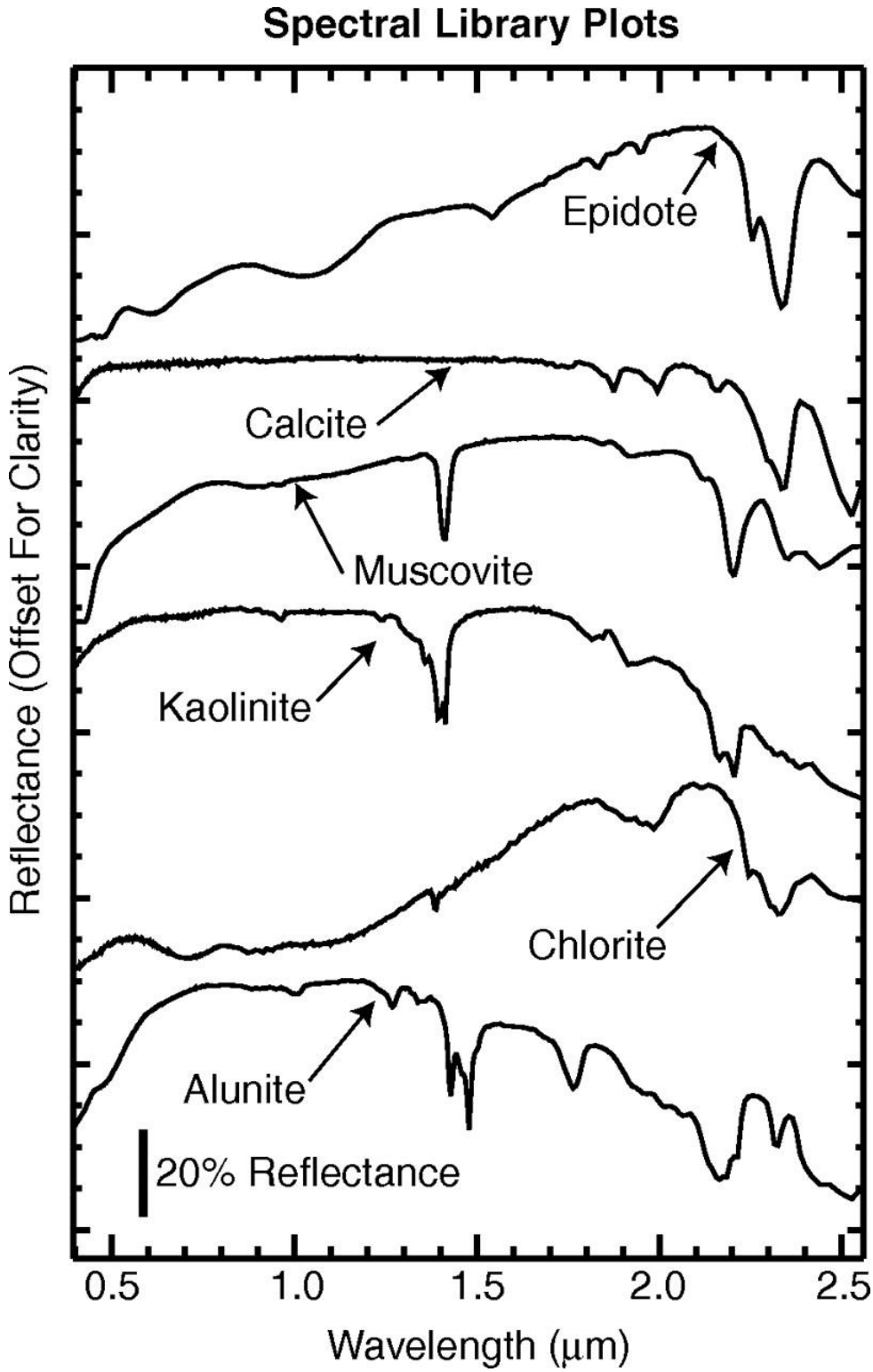

Figure 4: Laboratory spectra of epidote, calcite, muscovite, kaolinite, chlorite, and alunite, which are common hydrothermal alteration minerals (Clark et al., 1993b). Alunite and kaolinite have Al-O-H absorption features at 2.17 and 2.20 μm. Muscovite has a prominent Al-O-H absorption feature at 2.20 μm and a secondary 2.35 μm absorption feature. Chlorite and epidote have an Fe-Mg-O-H absorption feature at 2.32 μm and a broad Fe^{2+} feature from 0.6 μm to 1.65 μm. Calcite has a prominent CO_3^{2-} absorption feature at 2.33 μm. From Hunt and Salisbury (1970).

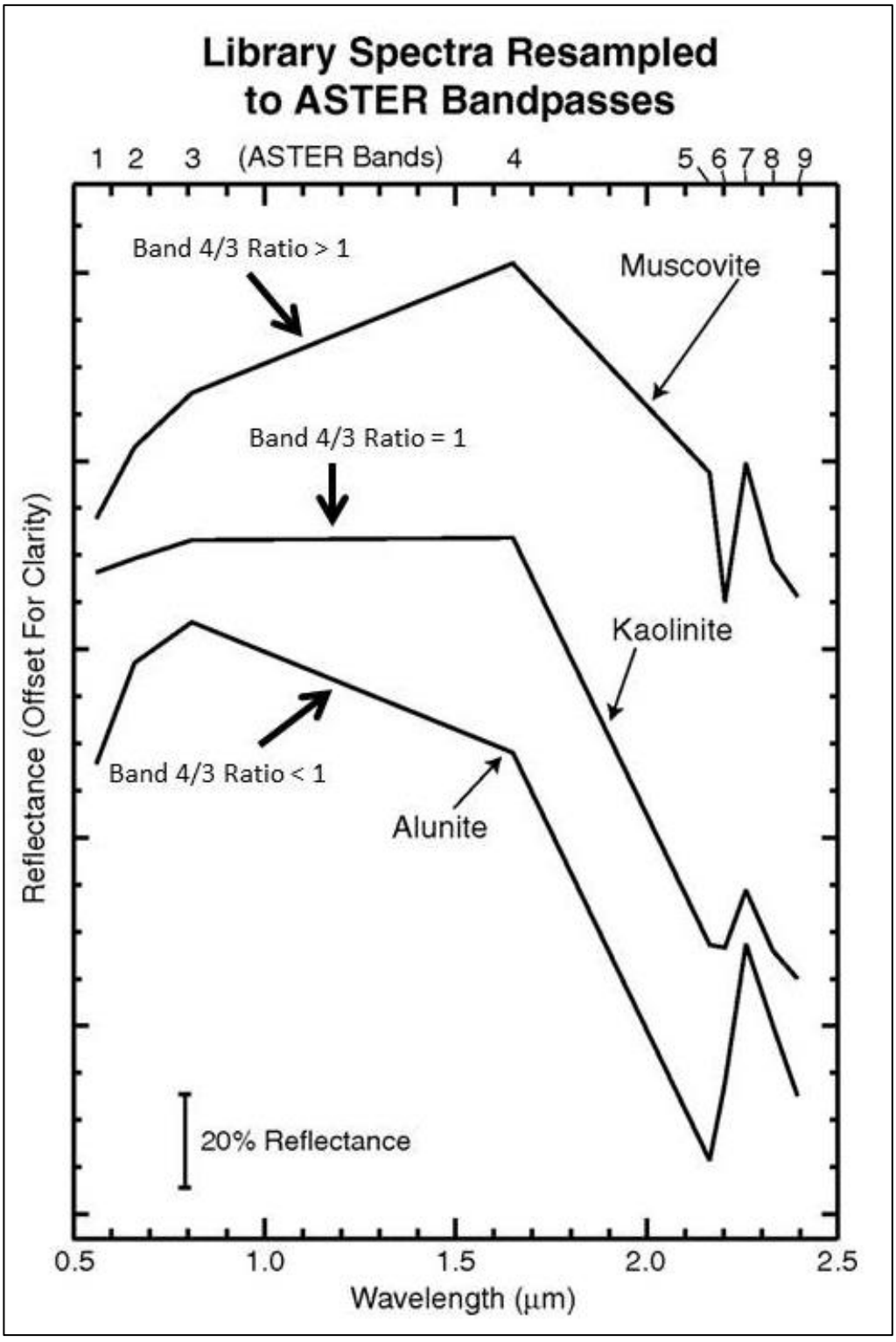

Figure 5: Laboratory reflectance spectra of alunite, kaolinite, and muscovite. The spectra have been resampled to ASTER bandpasses. Numbers across the top indicate ASTER band center positions. The spectral slopes estimated using the ASTER band 4/3 ratio shows how a band threshold can be determined from ASTER spectra. These spectral slopes allow us to distinguish minerals from one another. Modified from Mars and Rowan (2006).

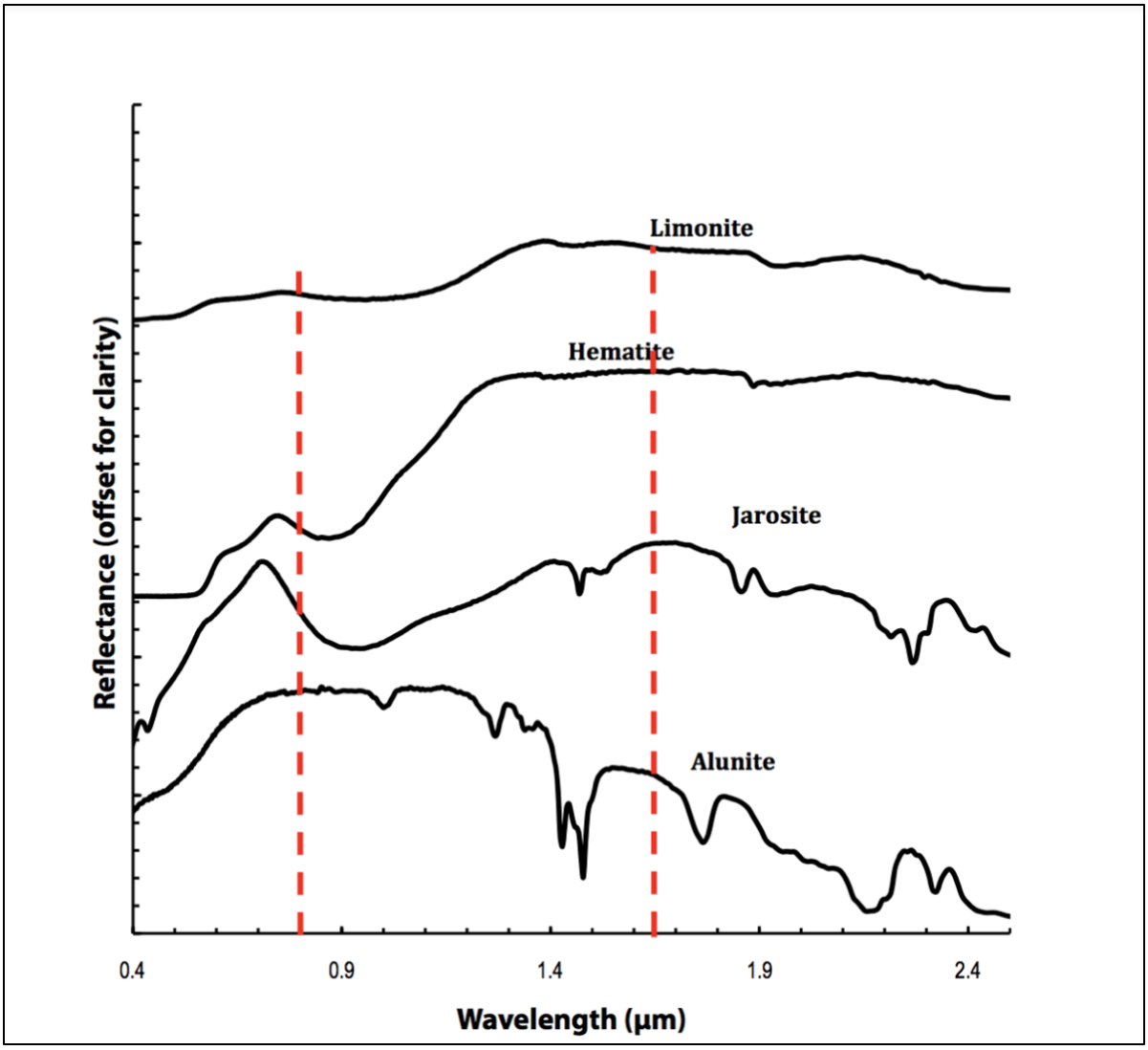

Figure 6: Spectra of alunite, jarosite, hematite, and limonite from the USGS spectral library. Notice the negative slope in alunite between ~0.8 µm (ASTER band 3) and ~1.65 µm (ASTER band 4) compared to the positive slope in jarosite, hematite, and limonite. The red dished lines show the negative slope for alunite between ~0.8 µm and ~1.65 µm. Modified from Clark et al. (1993).

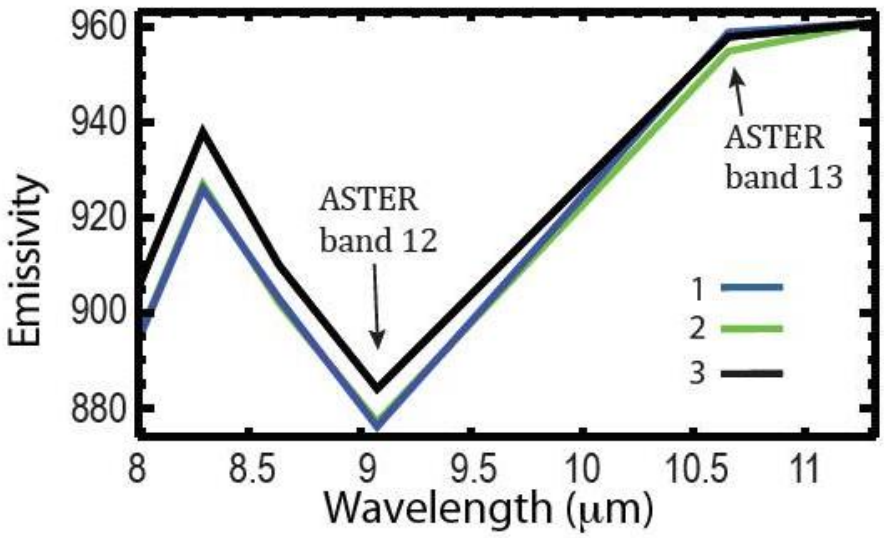

Figure 7: TIR emissivity spectra 1, 2 and 3 are from three locations in the Cuprite Hills that contain alunite according to the AVIRIS mineral map presented by Swayze et al. (2014). The ASTER band 13/12 ratio threshold value was estimated by noting that emissivity in ASTER band 13 is 8% greater than that in ASTER band 12. The Swayze et al (2014) AVIRIS mineral map is used to verify the effectiveness of our logical operator to map alunite.

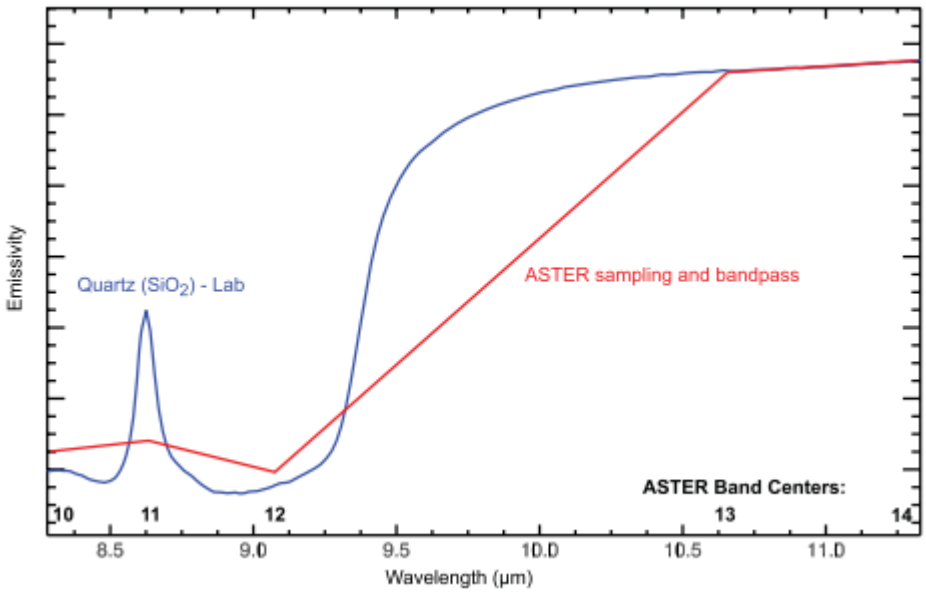

Figure 8: Plot of reference laboratory spectrum of quartz from Salisbury et al. (1991), converted to qualitative emissivity using Kirchoff's Law. The spectrum at original resolution is shown in blue. The spectrum convolved to ASTER bandpasses is shown in red. ASTER band centers are also shown along the bottom of the plot. Note the quartz Reststrahlen features at bands 10 and 12. From Rockwell and Hofstra (2008).

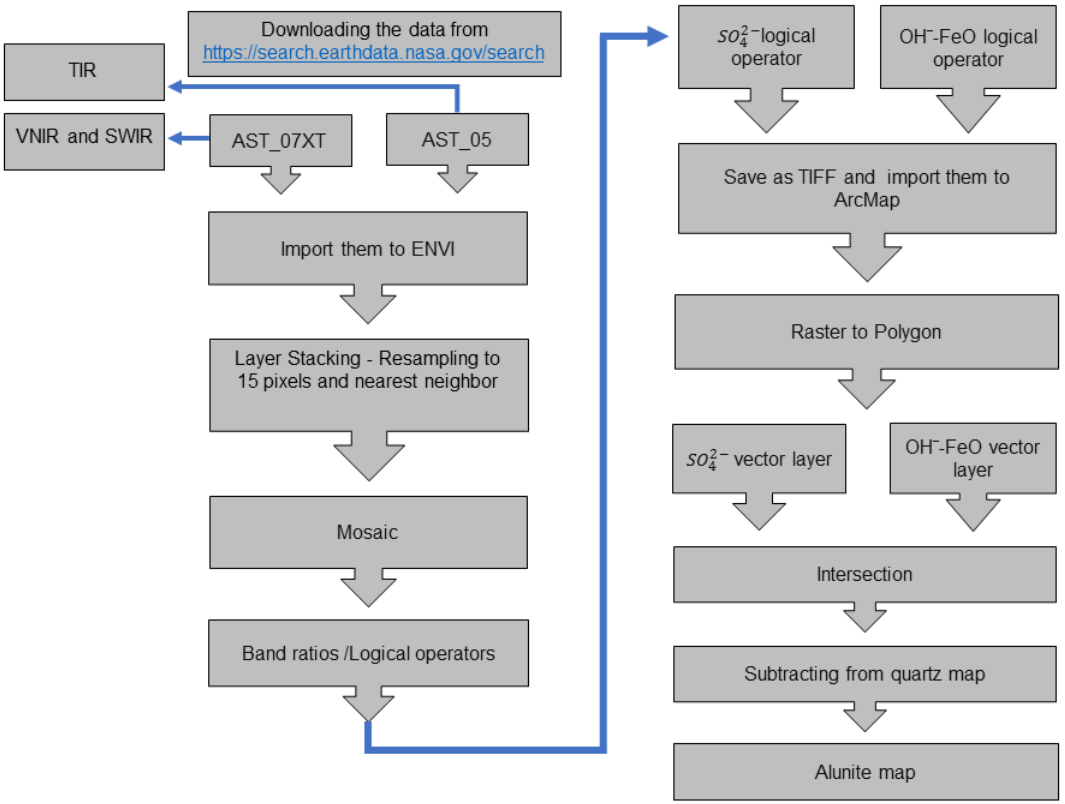

Figure 9: The workflow used to target alunite using ENVI and ArcMap software.

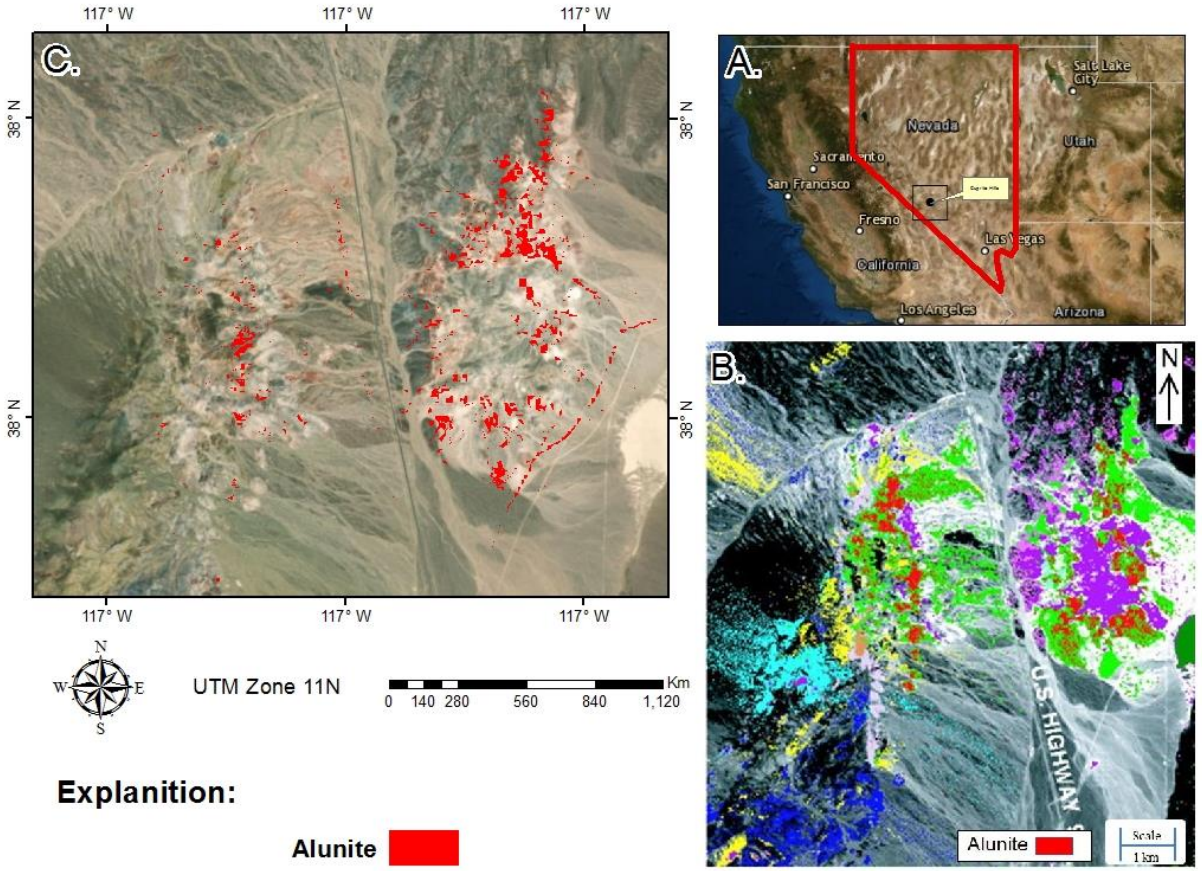

Figure 10: A. Location of Cuprite Hills, Nevada, USA. B. Mineral alteration results from Rowan and Mars (2003). C. Alunite map result from the work presented in this paper.

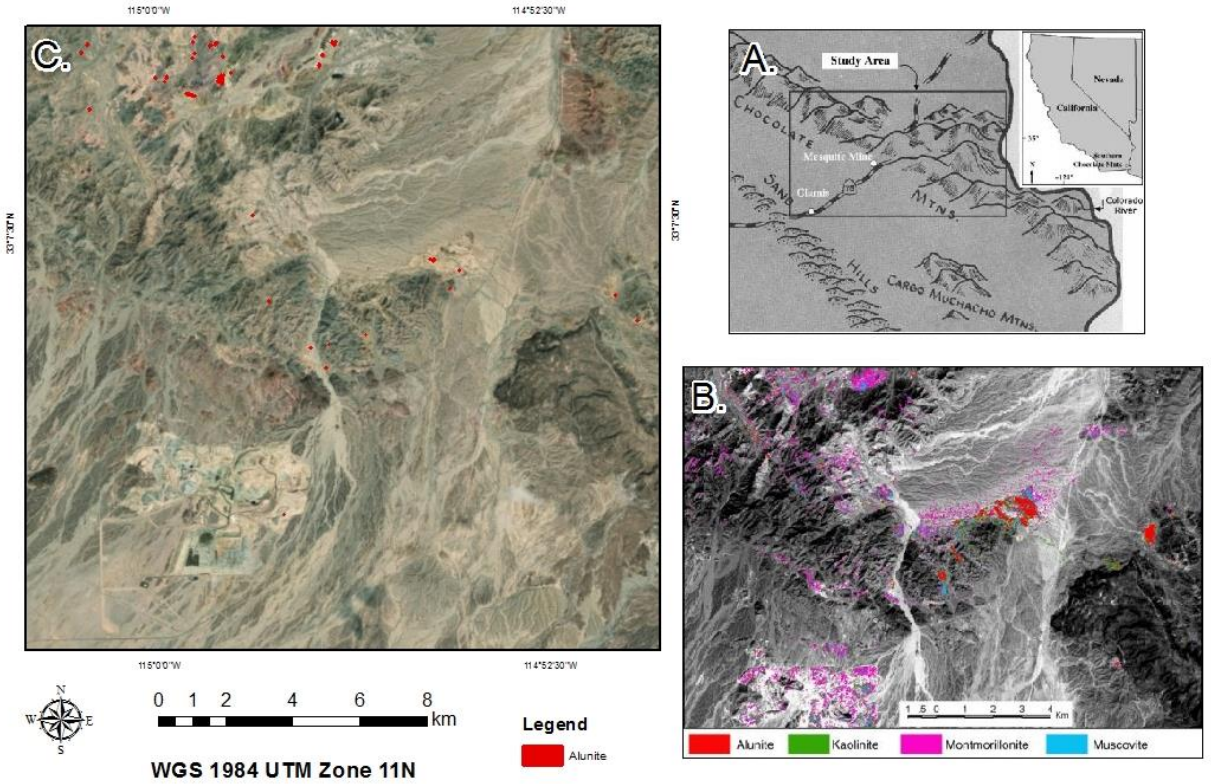

Figure 11: A. Location of the Chocolate Mountains, Imperial County, California, USA. B. Mineral alteration results from Zhang (2007). C Alunite map result from the work presented in this paper.

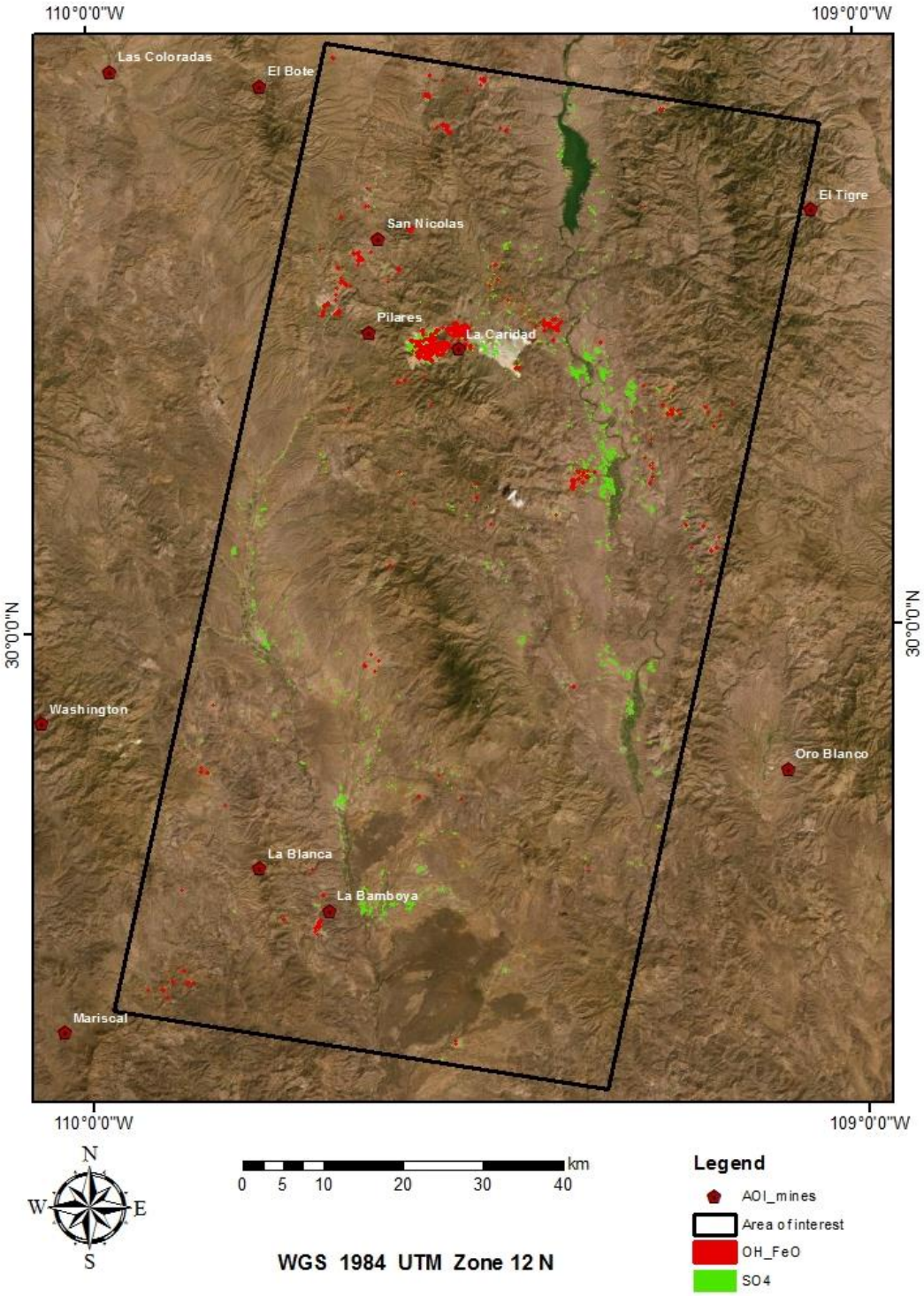

Figure 12: This map shows the results of the OH^--FeO logical operator and the SO_4^{2-} logical operator in the northern Sierra Madre Occidental, Sonora, Mexico. Also plotted are the locations of mines or prospects.

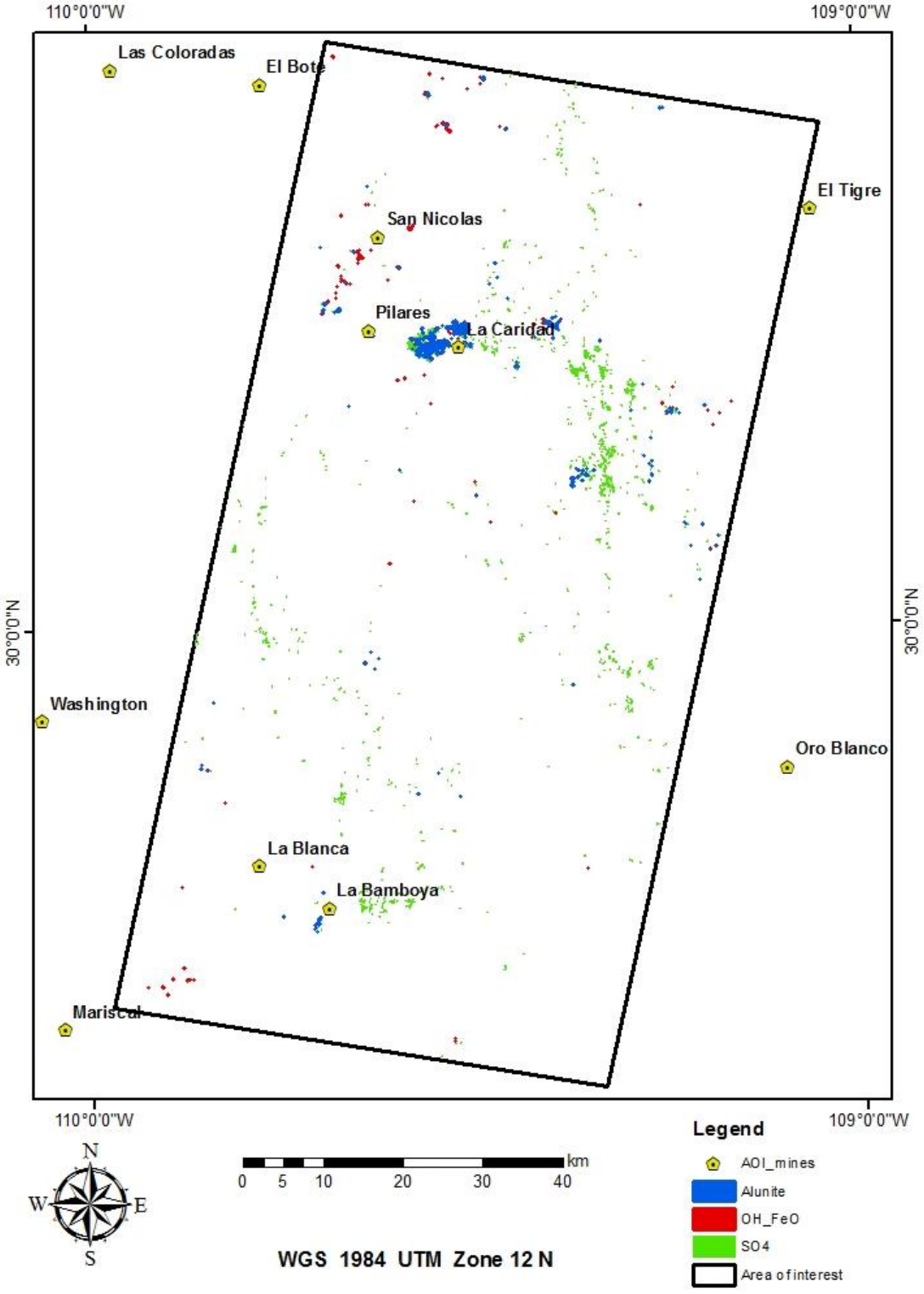

Figure 13: This map shows the results of the OH^--FeO logical operator and the SO_4^{2-} logical operator and the resulting alunite map in the northern Sierra Madre Occidental, Sonora, Mexico. Also plotted are the locations of mines or prospects.

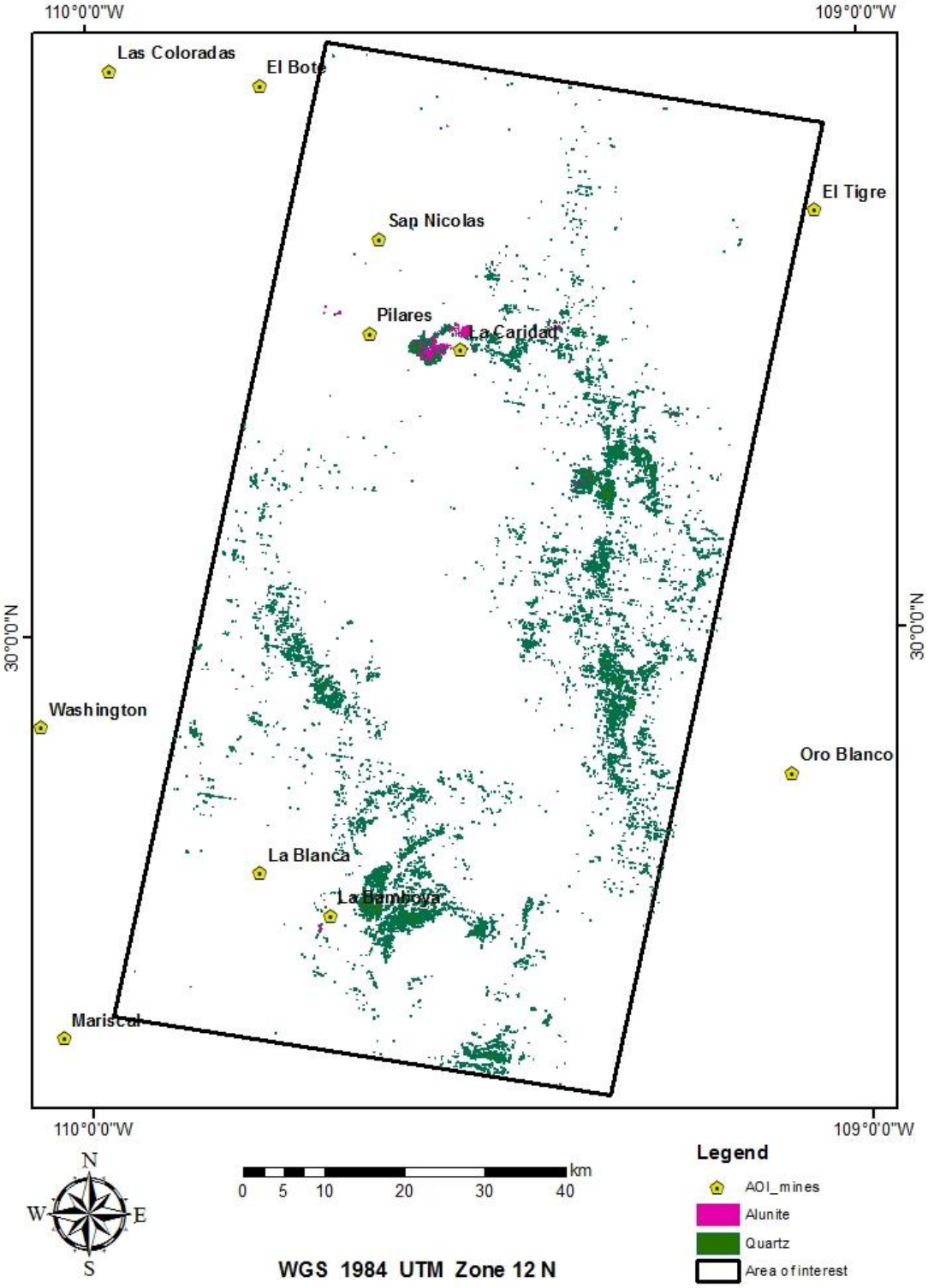

Figure 14: This map shows alunite before subtracting quartz in the northern Sierra Madre Occidental, Sonora, Mexico. Also shown are mines or prospects.

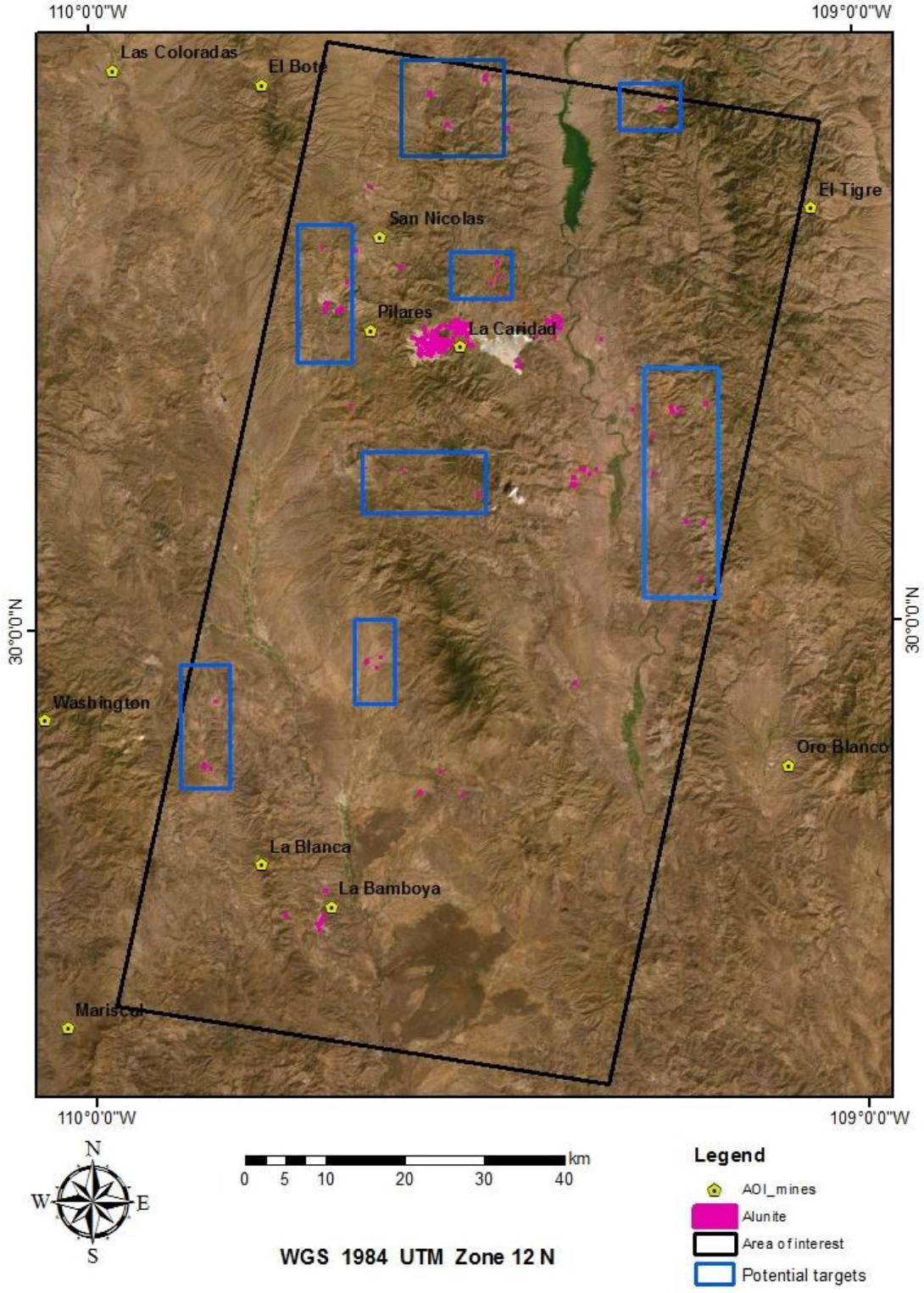

Figure 15: This map shows the alunite polygons, potential targets, and mines or prospects in the northern Sierra Madre Occidental, Sonora, Mexico.

CHAPTER 3: STATISTICAL DATA ANALYSIS OF AG-AU EPITHERMAL VEIN SYSTEMS IN THE GREATER TEMORIS MINING DISTRICT, PALMAREJO, CHIHUAHUA, MEXICO

ABSTRACT

Statistical data analyses are applied into three different deposits in the greater Temoris Mining District: Guerra al Tirano (100 samples), Guadalupe (2,985 samples) and La Millonaria (30 samples).Univariate, bivariate, and multivariate data distributions are analyzed to characterize the elemental geochemistry of the epithermal deposits. The precious metals (Au and Ag) at Guerra al Tirano are correlated with the base metals (Cu, Pb and Zn). However, the precious metals (Au and Ag) at Guadalupe and La Millonaria behave independently of the base metals (Cu, Pb and Zn). They were deposited in different paragenetic periods. The use of Ag/Au values is useful in exploration. The use of base metal ratio is not useful.

1. INTRODUCTION

Mineral exploration is the process of locating resources by the application of remote sensing, geological, geophysical, and geochemical methods, with a view to mine the mineral of interest. Analyzing satellite imagery is the first stage of mineral exploration to make interpretations of possible target areas (Moon et al., 2006). The geophysical methods are used to define any anomalies at the target area. The following stage includes a geochemical survey of outcrop, soil, and stream sediment samples to find areas anomalous in the commodity of interest, or elements related to a specific deposit type. Drilling programs can return large geochemical data sets.

Exploratory Data Analysis (EDA) techniques aid in the understanding and visualization by statistical data distribution with the use of graphical outputs, as explained by Reimann et al.

(2008). The statistical distribution of data may provide insights about geochemical processes or vector helpful in exploration.

In this study, statistical data analysis is performed in the Guerra al Tirano, Guadalupe and La Millonaria Ag-Au epithermal vein systems located in Palmarejo, Chihuahua, Mexico. Multi-element data analysis has been completed for 100 samples from surface and underground from Guerra al Tirano (Cleary, 2005), 2985 samples from 292 drill core sites from the Guadalupe vein (Molina, 2016), and 30 samples from La Millonria (Hernandez and Charest, 2013). Univariate, bivariate, and multivariate data distributions are analyzed in order to evaluate the geochemistry, detect trends, and define zonation patterns within the data.

2. OBJECTIVES

The goal of this research is to observe the relationship between the chemical elements of the epithermal deposits, in order to evaluate the geochemical properties of the mineralized deposit. Spatial variations (vectors) can provide information about where to explore next, and the genesis or origin of the deposit.

3. BACKGROUND

3.1 Study Area

The Palmarejo District is located 420 km by road southwest of the city of Chihuahua in the state of Chihuahua in northern Mexico. It is on the western edge of the Sierra Madre Occidental, in the Greater Temoris Mining District (Figure 1).

3.2 Regional Geology

The Sierra Madre Occidental (SMO) geologic province experienced different magmatic and tectonic episodes during Cretaceous-Cenozoic times associated with the subduction of the Farallon plate beneath the western North American plate, and to the plate tectonic opening of the

Gulf of California, the Baja rift (McDowell and Clabaugh, 1979; Atwater, 1988; Aguirre-Dıaz and McDowell, 1991; Aguirre-Dıaz and Labarthe-Hernandez, 2003; Swanson et al., 2006).

The SMO starts from a location just south of the Arizona-Sonora, Mexico, border, and it extends 1800 km to the south until Guadalajara in west-central Mexico. It is composed of volcanic rocks which overly a Precambrian- through Jurassic-ageD basement complex. Also, it is one of the major metallogenic provinces of gold and silver bearing epithermal deposits in Mexico ((Ferrari et al., 2007; Cather et al., 2009; Jicha et al., 2009; Bryan et al., 2008; Murray et al. 2013).

The Lower Volcanic Series (LVS) and the Upper Volcanic Series (UVS) are rock units which constitute most of the surface of the SMO. A few small windows exist showing older rocks. The LVS is an andesitic rock family formed above a subduction zone during compression, during tectonic events known as the Laramide (Ferrari et al., 2000). It regionally had two pulses, 80 Ma, and 60 to 45Ma. The UVS is mostly rhyolitic ash-flow tuffs issued from large calderas. They are mainly emplaced during two pulses in the Oligocene (ca. 32–28 Ma) and Early Miocene (ca. 24–20 Ma) (Ferrari et al., 2007).

3.3 Palmarejo District Geology

In the Palmarejo District, the lowest exposed unit of the LVS consists of rhyolitic flows, volcaniclastic units, and related shallow intrusions. These are overlain by andesitic flows and epiclastic rocks with related andesitic porphyry intrusions. Local pillow lavas and limestone within the andesitic sequence attest to their deposition in a subaqueous environment (Corbett, 2004).

Dacitic and rhyolitic intrusions in some areas are altered that are interpreted to be contemporaneous with the LVS. Cliff-forming rhyolitic ignimbrites of the UVS are well exposed in the eastern and southern parts of the project area.

Mineralization in the district, which is hosted largely in the LVS as well as in the UVS (Bryan et al., 2008) may be synchronous with the upper dacite and rhyolite intrusions (Laurent, 2004). Mineralized veins are commonly within 500 m of the unconformity with the Upper Volcanic Series (Masterman et al., 2005).

The LVS exhibits regional propylitic alteration. Structural extension in the district takes the form of what are interpreted to be listric normal faults striking north-northwest with west-northwest-trending flexures, as well as dilation of west-northwest-trending fractures caused by strike-slip faulting (Corbett, 2004).

Native silver is reported at Guerra al Tirano (Cleary, 2005). The mineralization of Guadalupe is comprised of quartz veins, quartz-vein breccias, hydrothermal breccias, and hematitic tectonic breccias. The dominant sulfide minerals in unoxidized portions of the vein include silver sulfosalts, pyrite, sphalerite, galena chalcopyrite, and argentite/acanthite (Laurent, 2004; Wilson et al., 2013). La Millonaria, gold rich mineralization structure consists of quartz – rich epithermal vein, breccias and stockworks displaying chalcedonic quartz fracture - filling and cocks comp texture. Occasionally, small pyrite grains are present in the matrix (Hernandez and Charest, 2013).

4. DATA AND METHODS

4.1 Data Processing

Guerra al Tirano data are surface, and underground geochemical results. One hundred samples have been collected for chemistry analysis of eight elements, which are Au, Ag, Cu, Pb,

Zn, As Sb, and Hg. The data contain the sample number, location, elevation, and width of vein (Cleary, 2005).

The data set for the Guadalupe deposit was obtained from a previous study (Molina, 2016). It consists of 2,985 samples collected at selected intervals from 292 drill core sites obtain from Coeur Mining exploration campaigns at Guadalupe. For the geostatistical analysis, 14 elements were explicitly analyzed Ag, Au, Sr, Pb, As, Zn, Fe, Mn, Ba, Sb, Cu, Cr, Mo, and Rb. The last five elements have more than 25% of their samples below the detection limit. Consequently they are not used in this study. Sb has 43% of its data below the detection limit. However, Sb was included in the multi-element analysis due to its importance in the precious metal deposits.

La Millonria data is for five elements, which are Au, Ag, Cu, Pb, and Zn for 30 samples (Hernandez and Charest, 2013).

The statistical analysis was done using R. All elements of the data are unified to be in ppm unit. The zeroes and negative values, which are less than 2 % of the data, are replaced with ½ of the smallest value > 0 (Helsel and Cohn, 1988). Cleaning the data was done in Microsoft Excel and the results converted to CSV format files and imported to R studio (version 1.0.153) for the statistics study and to do mapping in ArcMap (version 10.5).

4.2 Methods

For univariate analysis, a combination of histograms, one-dimensional scatter plots, and box plots are used to depict the distribution of each element (Reimann et al., 2008). A log transformation was applied to data where the distribution was heavily skewed in the univariate treatment. A univariate descriptive statistics data table (Table 1) was made to summarize the extensive data and understand it quickly.

A variation matrix (Reimann et al., 2008) and pairwise correlation table (Table 2) were constructed in order to analyze and discover special features related to composition. Principal Component Analysis (PCA) was used to reduce the number of dimensions of centered log-ratio clr-transformed data (Reimann et al., 2008) in order to interpret trends and variations in the data set (Levitan et al., 2014). The results of the PCA are represented with a robust biplot of compositional data.

Analysis of metal ratios is helpful for the quantitative description of chemical zoning in ore deposits. The rate of change of particular ratios along various paths can vary, reflecting changes in depositional factors (Goodell and Petersen, 1974; Titley, 1987).

5. RESULTS

5.1 Statistical Data Analysis

5.1.1 Summary Statistics

The measure for central value is represented with the mean and median. The measure for the spread is represented with the standard deviation (SD). These values, along with other statistical parameters, are summarized in Table 2A for Guerra al Tirano, Table 2B for Guadalupe, and Table 2C for La Millonaria.

5.1.2 Univariate

The statistical data of Guerra al Tirano is expressed by removing outliers (nugget effects) to all variables. Overall, the elements show a normal distribution after applying a log transformation to all variables. Au (Figure 2A), Cu (Figure 4A), Pb (Figure 5A), Zn (Figure 6A), Sb (Figure 8A), and Hg (Figure 9A) have at least three major families, while Ag (Figure 3A) and As (Figure 7A) have two significant families (Figure 2B-C). The box-plots for Au, Cu, Zn, As, Sb and Hg indicate which values are considered outliers.

The statistical analysis of Guadalupe data is expressed by applying a log transformation to all variables. Most of the data has two major families of distributions, which are Au (Figure 2B), Ag (Figure 3B), Pb (Figure 5B), Zn (Figure 6B), As (Figure 7B), Sb (Figure 8B), Ba (Figure 10A), and Mn (Figure 10D). The reaming elements, which are Sr (Figure 10B) and Fe (Figure 10C), have just one major family.

Univariate data of La Millonaria, after applying a log transformation to all variables, show normal distributions with two bimodal peaks (Figure 2C; Figure 3C; Figure 4C; Figure 5C; Figure 6C).

5.1.3 Bivariate

The pairwise comparison table of Guerra al Tirano deposit shows a strong relation between Ag with Au (0.9), Cu with Au (0.8), Cu with Ag (0.8), Pb with Ag (0.8), Pb with Au (0.7), and Hg with As (0.6), whereas negative relations between As with Ag (-0.02) and a strong negative relation between Zn with Hg (-0.1) (Table 2A and Figure 11).

The pairwise compression table of Guadalupe mine show strong positive relations between Pb with Zn (0.8), As with Fe (0.7), Sr with Mn (0.7), Au with Ag (0.6) and Ag with Pb (0.5) while Ba with Ag (-0.04), Sr with Pb (-0.04), Ba with Au (-0.03), Ag with As (-0.02) and Ag with Fe (-0.02) (Table 2. B) and (Figure 11)

The pairwise compression table of La Millonaria shows that Zn with Cu (0.6) and Zn with Pb (0.4) are the highest strong positive relation, whereas Zn with Au (-0.3) and Zn with Ag (-0.2) are the highest negative relation (Table 2C and Figure 11).

In order to observe proportional relationships between element log-ratios, variation matrices on clr-transformed data are constructed for the eight variables from Guerra al Tirano, ten variables from Guadalupe, and five variables from La Millonaria, geochemical data sets. The

log-ratios between the variables are calculated in each variation matrix using the robust median absolute deviation (MAD) of the log-ratios (upper triangle), as well as the variables log-ratio mean (lower triangle) (Table 4A-D). High values show high variance between the ratios of two elements, indicating disproportional relationships. Low values indicate low variability suggesting the two elements are proportional (Levitan et al., 2014).

Results from the variation matrix for the Guerra al Tirano indicate proportional relationships by the relative low log-ratio variances, of values below two, between Au/Ag, As/Hg, Cu/Hg, Cu/Pb, Cu/Sb, Cu/Zn, Hg/Zn, Pb/Zn, As/Cu, Au/Pb, As/Zn, As/Sb, and Sb/Zn. The highest proportionalities are between Cu/Pb and Hg/Sb with variation coefficients of 0.53 and 0.6, respectively. The highest log-ratio variances are between Au/As, Ag/As, Ag/Hg and Ag/Sb with coefficients above 5. The highest dispersion is seen in Ag and Au, which show high clr-MAD coefficients of 1.45 and 1.71, respectively (Table 4A).

Variation matrix results of Guadalupe indicate proportional relationships by the relative low log-ratio variances, of values below 1.5, between Pb/Zn, Sr/Fe, Sr/Mn, As/Fe, Ag/Au, Au/Sr, Au/Fe, Sr/Ba, Ar/Ba, and Zn/Fe. The highest log-ratio variances are between Ag/As, Ag/Ba and Pb/Mn with coefficients above 3.5. The highest dispersion in this data is seen in Ag and Sb, which show high clr-MAD coefficients of 1.22 and 1.33, respectively (Table 4B).

La Millonaria results show proportional relationships by the relative low log-ratio variances between Au/Ag, Cu/Zn, and Pb/Zn with variation coefficients of 1.86, 1.35, and 1.19, correspondingly. This result shows disproportional relationships between Au/Pb and Au/Zn with variation coefficients of 3.1 and 3.09, respectively. Zn and Au are the highest dispersion in this data with a value of 1.14 and 1.06, individually (Table 4C).

5.1.4 Multivariate

The main goal of a Principal Component Analysis (PCA) is to reduce dimensionality, as described by Reimann et al. (2008). Three compositional biplots of clr-transformed data are constructed for the PCA (Figure 5A-C). The principal components (PC) plotted from the Guerra al Tirano, Guadalupe, and La Millonaria prospect data are represented as loading vectors (arrows). Since the PCA is done with clr-transformed data, links between vectors can be used to interpret processes as explaind in Levitan et al. (2008). Short links suggest a low log-ratio variance between two elements, whereas, long links suggest disproportional relationships. Links can also be compared to one another. Parallel links or links with low angles between them indicate a correlation between the pairs of elements. Perpendicular links suggest independence between the pairs of elements, which may be verified with the variation matrix (Levitan et al., 2014).

For instance, Guerra al Tirano data shows low angle and short links between Cu- Pb which a low log-ratio variance between these two elements. Ag and Au show proportional relationships between them because of the low angle. Zn seems disassociated within the data as its loading vector points towards the negative PC 2 (Figure 2AC). These observations are consistent with results from the variation matrix (Table 4A).

Fe, Ba and As of Guadalupe PCA show low variability because of the low angles and short links between them. Moreover, low variability between Zn and Pb exists as illustrated by the links between the element pairs that are short and of low angle. The low angle between Sr and Mn shows the low variability between them (Figure 13AC).

Finally, Cu-Zn and Pb-Zn show low variability while Au and Ag show high variability with the rest of this data of La Millonaria prospect (Figure 1AC).

5.2 Metal Spatial Distributions

According to Guerra al Tirano data, high values of Au diagram in the central part of the area, and in deeper portions (Figure 15A). The high value of Ag is concentration in the center (Figure 15B). Cu, Pb, and Zn are similar and concentrated in the center, and the values decrease going north and south (Figure 15C-E).

Guadalupe spatial distributions are not systematic because they have a lot of scatter. Au in Guadalupe data shows higher values deeper, in the center, south, and north (Figure 16A), whereas the high values of Ag, Zn, and Pb are in some places north deep, center deep and top, and south deep (Figure 16B-D).

5.3 Metal Ratio Spatial Distribution

The log (Ag/Au) vs. log (Au) diagram of Guerra a Tirano (Figure 17A) range between 10 to 1000 of log (Ag/Au), and 0.01 to 300 ppm of Au values. The lower limit of Au detection is 0.01 ppm, which it has different analytical method than Guadalupe data.

With respect to Guadalupe data, it contains a large number of samples and data points (2,985) (Figure 17). The results range from 2,620 down to 0.8, which is the concentration of the ratio. 0.1 ppm is the lower limit detection for Au, and the values extend to 300 ppm. The result of Guerra al Tirano and Guadalupe overlap (Figure 17).

La Millonaria data varies from less than 1 ppm up to 20 ppm of Au, and it is compared a degree of variability of log(Ag/Au) from 0.2 to 30 (Figure 17).

According to the statistic results of Guerra al Tirano, metal ratios should be mapped because of the good opportunity to look for vectors, for instance Ag/Au, Cu/Ag, Cu/Au, Pb/Ag and Pb/Au. Ag/Au and Pb/Au show two locations of high values, the center and the far south.

The values decrease away from the center (Figure 18A). Cu/Ag, Cu/Au, and Pb/Ag show the high value in the center and the values decrease going away from the center (Figure 18B-D).

In another region, Guadalupe data is complicated because of the large number of samples. They are drill holes, and some points overlap. Pb/Zn, Ag/Au, and Ag/Pb (Figure 1A-C) are the most important metal ratios, and they have strong positive relations in this data. To make Guadalupe data more understandable, the date is divided to north and south region.

In the north, the majority of the high values of Ag/Au are located near to the surface while Pb/Zn and Ag/Pb are deeper and near the center. In the south, Ag/Au and Ag/Pb show many of high values and are located in the center to the surface.

6. DISCUSSION

The highest values of Zn, Pb and Ag are in Guadalupe mine with 225.8, 117.3 and 108.8 ppm respectively. Guerra al Tirano is the second highest values of Zn, Pb and Ag with 84.5, 57 and 70 ppm respectively (Figure 20) and is highest value of Cu (59.5 ppm) (Figure 20). La Millnoaria prospect has the highest value of Au of 4.8 ppm. The statistical data provide clues about the geochemical processes or trends involved in the mineralization. Results integrated from Table 4, Figure 11 and Figure 20, are distinct paragenetic groups. Their actual time or crustification relations have not been observed. They were deposited as a group but separate from other groups.

The bivariate and multivariate analyses of the three regions show the behavior of elements within the ore fluids as they were being deposited. In Guerra al Tirano, (Au+Ag), (Cu+Pb), (Hg+As) were depositing together (Table 4), and Sb and Zn were been deposited individually. Guadalupe results show that (Ag+Au), (Pb+Zn), (Sr+Mn) and (As+Fe) deposited together, and Ba and Sb were been deposited separately (Table 4). In La Millonaria, (Cu+Zn)

were each deposited together in this region, and Au, Pb, and Ag were been deposited individually.

7. CONCLUSION

PCA based on log-ratio transformation techniques showed significant potential in drawing conclusions in Guerra al Tirano, Guadalupe and La Millonaria. The precious metals (Au and Ag) at Guerra al Tirano are correlated with the base metals (Cu, Pb and Zn). However, the precious metals (Au and Ag) at Guadalupe and La Millonaria behave independently of the base metals (Cu, Pb and Zn). They were deposited with different times for instance Pb/Cu or Pb/Zn will not give correlation values with Ag/Au. Even though Figure 17 shows that Guerra al Tirano and Guadalupe data overlap, and they may be part of the same genetic system, and they are separately by 3 km.

Traditionally geochemical analysis of multi elements association leads to the conclusion that is As and Sb are intimately associated with precious metal, However, in this particle case where they do not seem to be correlated with Au or Ag.

REFERENCES

Aguirre-Díaz, G.J., and McDowell, F.W. 1991. The volcanic section at Nazas, Durango, Mexico, and the possibility of widespread Eocene volcanism within the Sierra Madre Occidental: Journal of Geophysical Research, v. 96, p. 13373–13388.

Aguirre-Díaz. G.J., and Labarthe, H. G. 2003. Fissure ignimbrites: fissure source origin for voluminous ignimbrites of the Sierra Madre Occidental and its relationship with Basin and Range faulting: Geology, 31, 773–776.

Atwater, T., and Stock, J.M. 1988. Pacific-North America plate tectonics of the Neogene southwestern United States: An update: International Geology Review, v. 40, p. 375–402.

Bryan, S.E., Ferrari, L., Reiners, P.W., Allen, C.M., Petrone, C.M., Rosique, A.R., and Campbell, I.H. 2008. New Insight into Crustal Contributions to Large-volume Rhyolite Genenration in the Mid Tertiary Sierra Madre Occidental Province, Mexico, Revealed by U-Pb Geochronology: Journal of Petrology, v. 49, p. 47-77.

Cather, S.M., Dunbar, N.W., McDowell, F.W., McIntosh, W.C., and Scholle, P. A. 2009.Climate forcing by iron fertilization from repeated ignimbrite eruptions: The icehouse–silicic large igneous province (SLIP) hypothesis: Geosphere, v. 5, no. 3, p. 315–324.

Corbett, G. 2004. Comments on Palmarejo, El Realito and Yecora Exploration Projects, Northern Mexico, private report for Planet Gold SA de CV., p. 37.

Ferrari, L., and Valencia-Moreno, M. 2007. Magmatism and tectonics of the Sierra Madre Occidental and its relation with the evolution of the western margin of North America, in Alaniz- Álvarez, S.A., and Nieto-Samaniego, Á.F., eds., Geology of México: Celebrating the Centenary of the Geological Society of México: Geological Society of America Special Paper 422, p. 1–39.

Ferrari, L., Pasquarè, G., Venegas, S., and Romero, F. 2000.Geology of the Western Mexican Volcanic Belt and Adjacent Sierra Madre Occidental and Jalisco Block, in Delgado-Granados, H., Aguirre-Díaz, G.J., and Stock, J.M., eds., Cenozoic Tectonics and Volcanism of Mexico: Geological Society of America Special Paper 334, p. 65–84.

Cleary, J.G. 2006. Report on the Geology and Current Status of the Guerra al Tirano Silver-Gold Property, Temoris District, Chihuahua, Mexico; NI-43-101 Technical Report prepared for Hansa Corporation, Calgary, Alberta, Canada. Durgin, D., 2007, Technical Report San Miguel Project, Chihuahua, Mexico; NI-43-101 Technical Report prepared for Paramount Gold Mining Corp.

Helsel, D. R. and Cohn, T. 1988. Estimation of Descriptive Statistics for Multiply Censored Water Quality Data. Water Resource. Res. 24, 1997–2004.

Hernandez, M. H and Charest, A. R. 2013. The La Millinoria gold project, Chihuahua, Mexico. Arcelia Gold Crop, Vancouver.

Jicha, B.R., Scholl, D.W., and Rea, D.K. 2009. Circum- Pacific arc flare-ups and global cool- ing near the Eocene-Oligocene boundary: Geology, v. 37, p. 303– 306.

Laurent, I. 2004. Palmarejo/Trogan Project: Annual Technical Report, internal report of Planet Gold, S.A. de C.V.

Levitan, D.M., Zipper, C. E., Donovan, P., Schreiber, M. E., Seal II, R. R., Engle, M. A., Chermak, J. A., Bodnar, R. J., Johnson, D. K., Aylor Jr., J. G. 2014. Statistical analysis of soil geochemical data to identify pathfinders associated with mineral deposits: An example from the Coles Hill uranium deposit, Virginia, USA. Journal of Geochemical Exploration, http://dx.doi.org/10.1016/j.gexplo.2014.12.012.

Masterman, G., Phillips, K., Stewart, H., Laurent, I., Beckton, J., Cordery, J., Skeet J. 2005. Palmarejo Silver-Gold Project, Chihuahua, México: Discovery of a Ag-Au Deposit in The Mexican Sierra.

McDowell, F.W., and Clabaugh, S.E. 1979. Ignimbrites of the Sierra Madre Occidental and their relation to the tectonic history of western Mexico, Geological Society of Amerce, Special Paper 180, p. 113 – 124,.

Molina, C., 2016. Geology and Mineralization Controls Surrounding the Palmerejo Mining District - A Compilation of Remote and Hands-on Exploration Techniques: PhD Dissertation. University of Texas at El Paso, p.114.

Moon, C., Whateley, M. K. G., Evans, A. M. 2006. Introduction to Mineral Exploration. Textbook, P. 496 .

Murray, B., Busby, C., Ferrari, L., Solari, L. 2013. Synvolcanic crustal extension during the mid-Cenezoic ignimbrite flare-up in the northern Sierra Madre Occidental, Mexico: Evidence from the Guazapares Mining District region, western Chihuahua, Geosphere, v. 9, n. 5, p. 1-35.

Reimann, C., Filzmoser, P., Garrett, R.G., Dutter, R. 2008. Statistical data analysis explained: applied environmental statistics with R. John Wiley & Sons, Chichester, UK., P. 362.

Swanson, E.R., Kempter, K.A., McDowell, F.W., McIntosh, W.C. 2006. Major ignimbrites and volcanic centers of the Copper Canyon area: A view into the core of Mexico's Sierra Madre Occidental: Geosphere, v.2, no. 3, p. 125-141.

Titley, S. R. 1987. The crustal heritage of silver and gold ratios in Arizona ores. GSA Bulletin (1987), 99(6), 814–826.

Wilson, S. E., Gustin, M. M., Brechtel, C., George, T., Pennstrom, W. J., Aguayo, P. 2013. Technical Report and Preliminary Economic Assessment for the San Miguel Project, Guazapares Mining District, Chihuahua, Mexico. Private report, Prepared for Paramount Gold and Silver Corp.

Table 1A-C: Summary statistics of geochemical data for the Guerra al Tirano, Guadalupe, and La Millnoaria. MIN - Minimum; MED - median; MAX – maximum and SD - standard deviation.

A. Guerra al Tirano

Elements	MIN	MED	MEAN	MAX	SD
Au	0.01	0.35	1.49	20.00	3.20
Ag	0.50	33.00	70.55	200.00	76.99
Cu	10.00	59.50	108.60	2160.00	250.50
Pb	14.00	57.00	186.60	6800.00	684.50
Zn	13.00	84.50	159.80	1755.00	223.90
As	1.00	26.50	36.58	463.00	50.79
Sb	1.00	3.00	8.23	254.00	26.86
Hg	0.01	0.06	0.10	1.00	0.13

B. Guadalupe

Elements	MIN	MED	MEAN	MAX	SD
Au	0.5	0.5	1.667	300	7.909
Ag	5	58	108.8	4420	200.9
Pb	1.7	44.96	117.3	11010	380.2
Zn	3.15	102.4	225.8	17020	592.9
As	3.1	30.73	47.57	798.5	57.44
Sb	5	17.35	23.01	170	22.36
Fe	360	9476	13350	74010	10920
Mn	37.5	1579	2251	23050	2239
Ba	18.9	278.3	495	28110	849.1
Sr	1.5	40.12	54.16	1178	49.81

C. La Millnoaria

Elements	MIN	MED	MEAN	MAX	SD
Au	0.64	2.805	4.817	22.8	5.881
Ag	1.2	6.55	13.759	59.2	15.712
Cu	0.001	0.004	0.0367	0.628	0.11931
Pb	0.001	0.004	0.009666	0.126	0.022441
Zn	0.001	0.008	0.0106	0.028	0.008938

Table 2A-C: Pairwise Comparison of geochemical data from the three deposits to investigate proportional relationship between variables (Reimann et al., 2008).

A. Guerra al Tirano

Elements	Au	Ag	Cu	Pb	Zn	As	Sb	Hg
Au	1	0.9	0.8	0.8	0.4	0.2	0.3	0.2
Ag	0.9	1	0.8	0.8	0.4	-0.02	0.3	0.1
Cu	0.8	0.8	1	0.7	0.4	0.1	0.3	0.1
Pb	0.8	0.8	0.7	1	0.5	0.2	0.4	0.2
Zn	0.4	0.4	0.4	0.5	1	0.1	0.06	-0.1
As	0.2	-0.02	0.1	0.2	0.1	1	0.4	0.6
Sb	0.3	0.3	0.3	0.4	0.06	0.4	1	0.4
Hg	0.2	0.1	0.1	0.2	-0.1	0.6	0.4	1

B. Guadalupe

Elements	Au	Ag	Pb	Zn	As	Sb	Fe	Mn	Ba	Sr
Au	1	0.6	0.3	0.2	-0.1	-0.1	-0.1	0.2	-0.3	-0.01
Ag	0.6	1	0.5	0.4	-0.2	0.09	-0.2	0.1	-0.4	-0.2
Pb	0.3	0.5	1	0.8	0.05	0.07	0.2	-0.03	0.1	-0.1
Zn	0.2	0.4	0.8	1	0.2	0.03	0.4	0.04	0.2	-0.02
As	-0.1	-0.2	0.05	0.2	1	-0.05	0.7	0.06	0.5	0.2
Sb	-0.1	0.09	0.07	0.03	-0.05	1	-0.1	-0.3	-0.3	-0.4
Fe	-0.1	-0.2	0.2	0.4	0.7	-0.1	1	0.03	0.6	0.2
Mn	0.2	0.1	-0.03	0.04	0.06	-0.3	0.03	1	-0.1	0.7
Ba	-0.3	-0.4	0.1	0.2	0.5	-0.3	0.6	-0.1	1	0.3
Sr	-0.01	-0.2	-0.1	-0.02	0.2	-0.4	0.2	0.7	0.3	1

C. La Millnoaria

Elements	Au	Ag	Cu	Pb	Zn
Au	1	0.3	0.02	-0.2	-0.3
Ag	0.3	1	0.4	0.04	-0.2
Cu	0.02	0.4	1	0.2	0.6
Pb	-0.2	0.04	0.2	1	0.4
Zn	-0.3	-0.2	0.6	0.4	1

Table 3A-C: Variation matrices of centered-log ratio (clr) transformed geochemical data from the three deposits to investigate proportional relationship between variables (Reimann et al., 2008).

A. Guerra al Tirano

Elements	Au	Ag	As	Cu	Hg	Pb	Sb	Zn	clr.MAD
Au	0	0.96	5.21	2.49	4.01	1.62	3.86	3.04	1.45
Ag	-4.21	0	6.86	2.92	5.54	2.11	5.26	4.08	1.71
As	-4.3	-0.04	0	1.8	0.94	2.02	1.22	1.89	1.22
Cu	-5.39	-1.12	-1.05	0	0.95	0.53	0.82	0.72	0.45
Hg	1.44	5.75	5.78	6.86	0	1.63	0.6	1.58	0.93
Pb	-5.51	-1.27	-1.18	-0.1	-6.95	0	1.38	0.69	0.62
Sb	-2.54	1.75	1.81	2.92	-3.99	2.98	0	1.49	0.87
Zn	-5.83	-1.6	-1.52	-0.45	-7.3	-0.31	-3.36	0	0.89

B. Guadalupe

Elements	Au	Ag	Pb	Zn	As	Sb	Fe	Mn	Ba	Sr	clr.MAD
Au	0	1.12	2.16	1.49	2.27	1.88	1.37	1.79	2.35	1.13	0.7
Ag	-4.14	0	1.73	1.75	3.94	2.45	2.76	2.85	4.1	2.58	1.22
Pb	-3.92	0.23	0	0.54	3.07	2.79	2.04	3.55	2.93	2.5	0.92
Zn	-4.89	-0.72	-0.92	0	1.98	2.18	1.1	2.33	2.19	1.64	0.66
As	-3.55	0.63	0.39	1.3	0	2.57	0.56	2.82	1.48	1.56	0.91
Sb	-2.94	1.25	1.07	2.01	0.62	0	1.76	3.14	2.84	2.16	1.33
Fe	-9.49	-5.27	-5.46	-4.58	-5.9	-6.55	0	2.05	0.84	0.66	0.63
Mn	-7.43	-3.26	-3.47	-2.52	-3.89	-4.56	2.05	0	3.19	0.6	0.95
Ba	-5.9	-1.71	-1.87	-0.96	-2.34	-2.99	3.58	1.57	0	1.3	1.12
Sr	-3.99	0.22	0.02	0.95	-0.41	-1.07	5.56	3.49	1.94	0	0.67

C. La Millonaria

Elements	Au	Ag	Cu	Pb	Zn	clr.MAD
Au	0	1.86	2.29	3.1	3.09	1.06
Ag	-1.01	0	2.31	2.95	2.73	1.01
Cu	6.29	7.29	0	2.07	1.35	0.44
Pb	6.44	7.41	0.12	0	1.19	0.91
Zn	5.96	6.99	-0.34	-0.46	0	1.14

Variables Log-ratio variances Log-ratio mean Clr-median absolute deviation

Table 4: Paragenetic groups for the three regions.

Groups	Guerra al Tirano	Guadalupe	La Millonaria
1	Ag + Au	Ag + Au	Au
2	Cu + Pb	Pb + Zn	Zn + Cu
3	Zn	Ba	Pb
4			Ag
5	Hg + As	As + Fe	
6	Sb	Sb	
7		Sr + Mn	

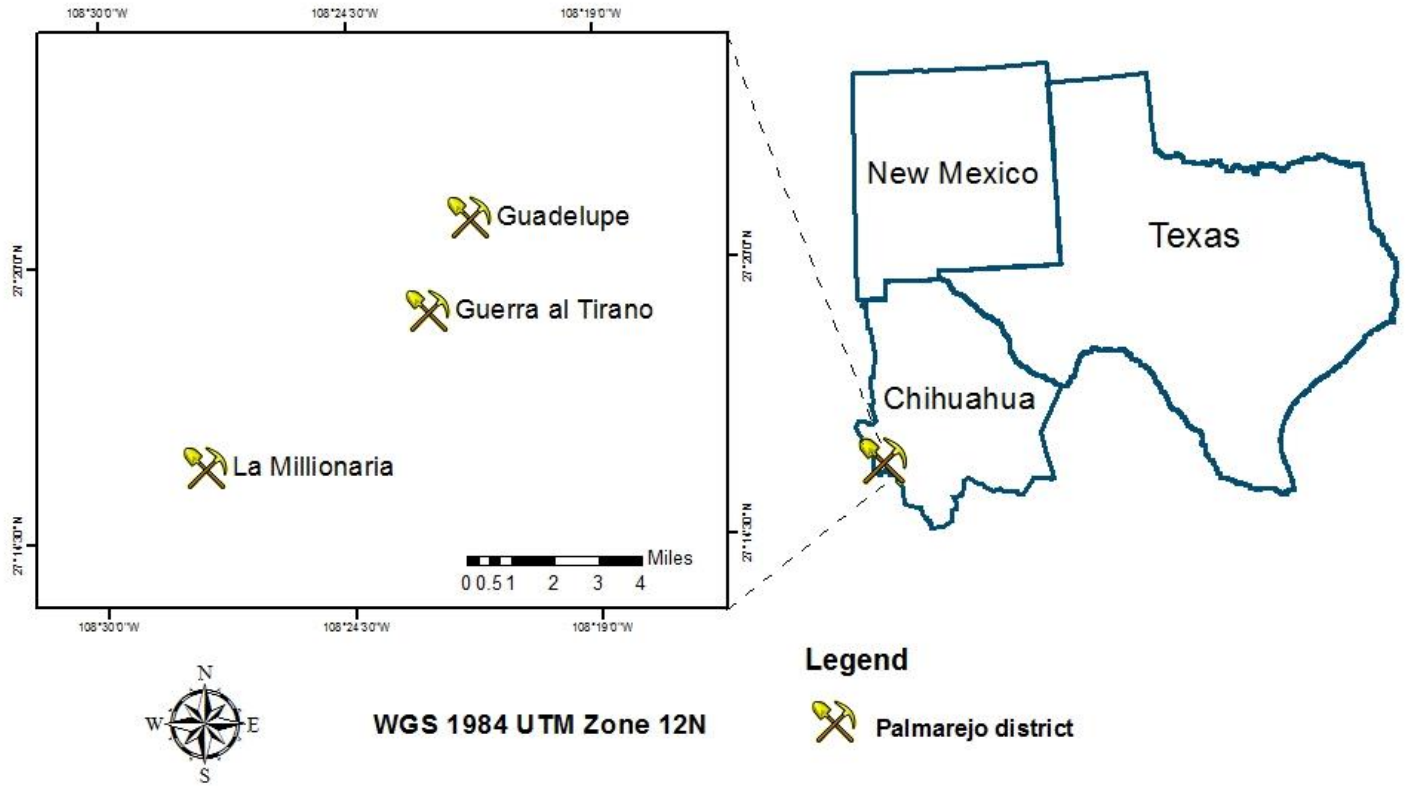

Figure 1: Location map showing the three regions of interest.

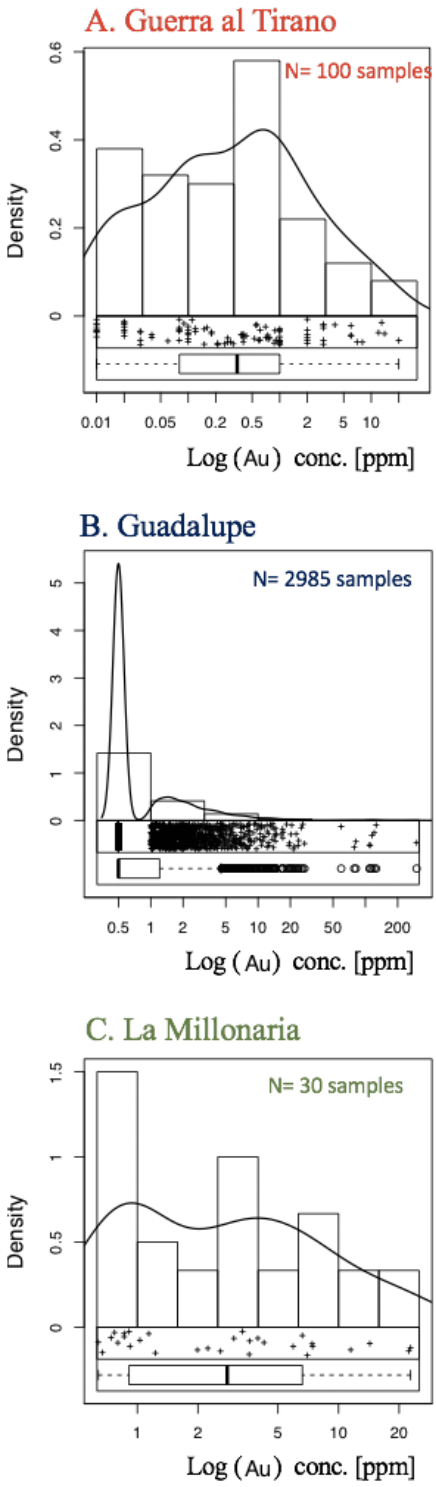

Figure 2A-C: Univariate density histograms, one-dimension density plots and box plots for Au concentration data for the three regions (Reimann et al., 2008). Note differences in scale in x axes.

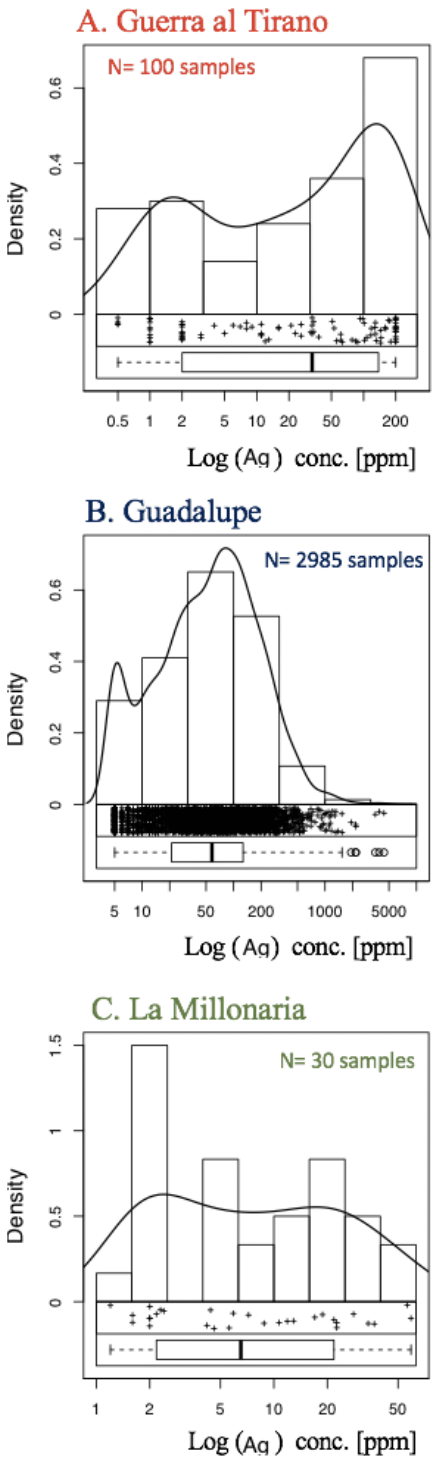

Figure 3A-C: Univariate density histograms, one-dimension density plots and box plots for Ag concentration data for the three regions (Reimann et al., 2008). Note differences in scale in x axes.

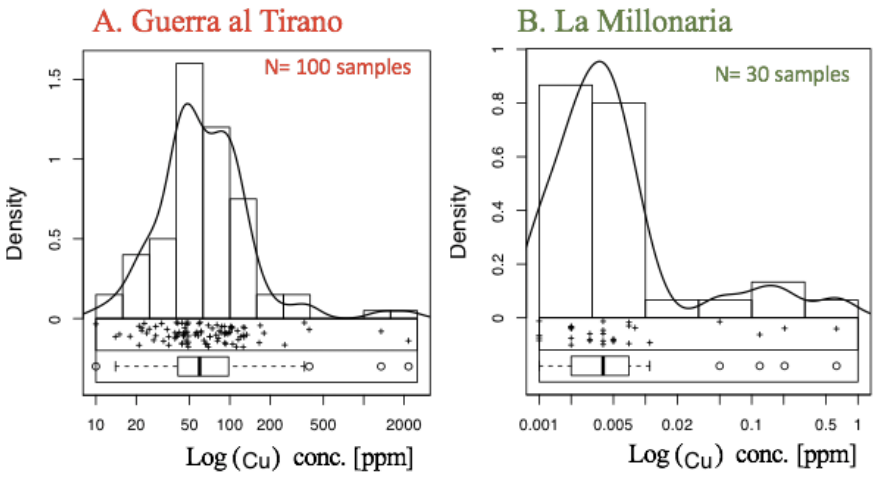

Figure 4A-B: Univariate density histograms, one-dimension density plots and box plots for Cu concentration data for the two regions (Reimann et al., 2008). Note differences in scale in x axes.

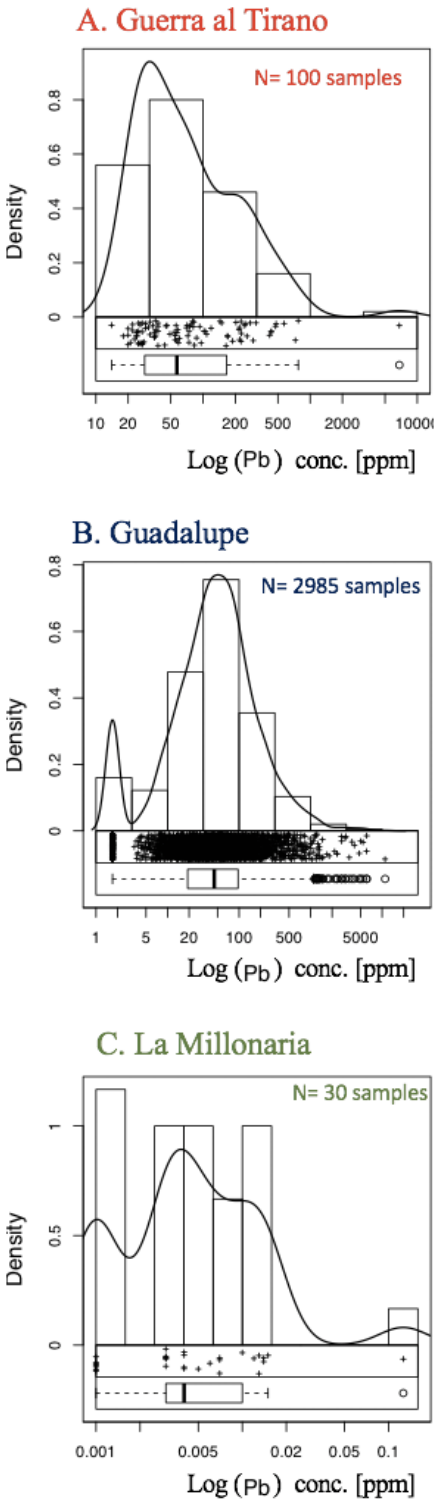

Figure 5A-C: Univariate density histograms, one-dimension density plots and box plots for Pb concentration data for the three regions (Reimann et al., 2008). Note differences in scale in x axes.

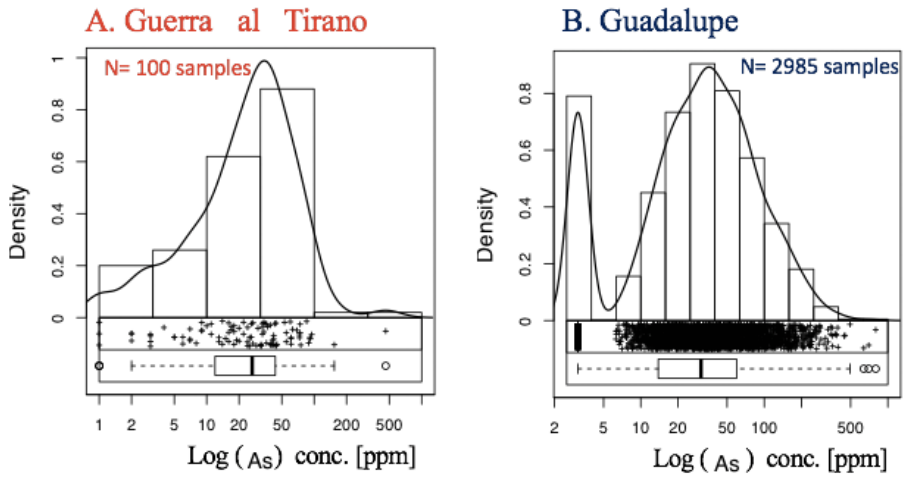

Figure 7A-B: Univariate density histograms, one-dimension density plots and box plots for As concentration data for the two regions (Reimann et al., 2008). Note differences in scale in x axes.

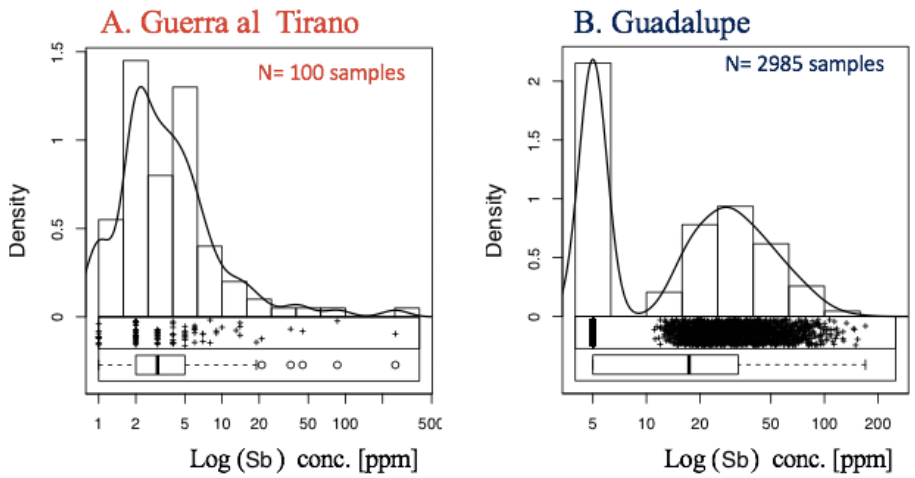

Figure 8A-B: Univariate density histograms, one-dimension density plots and box plots for Sb concentration data for the three regions (Reimann et al., 2008). Note differences in scale in x axes.

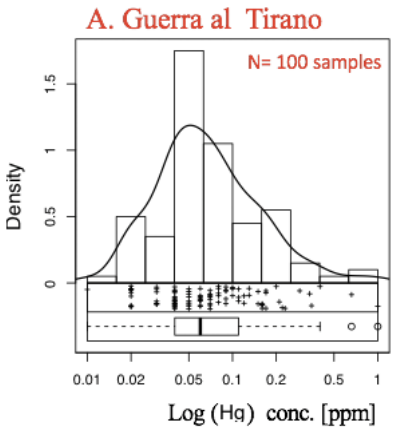

Figure 9A: Univariate density histograms, one-dimension density plots and box plots for Hg concentration data for the Guerra al Tirano (Reimann et al., 2008). Note differences in scale in x axes.

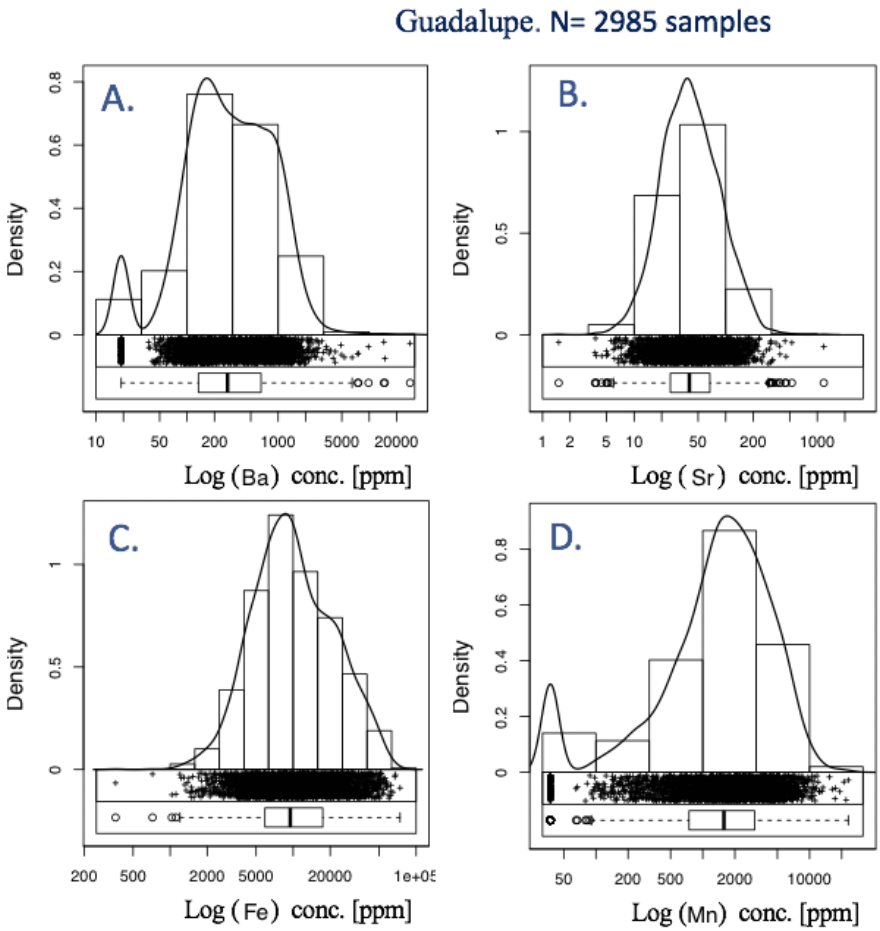

Figure10A-D: Univariate density histograms, one-dimension density plots and box plots for Ba, Sr, Fe and Mn concentration data for the Guadalupe (Reimann et al., 2008). Note differences in scale in x axes.

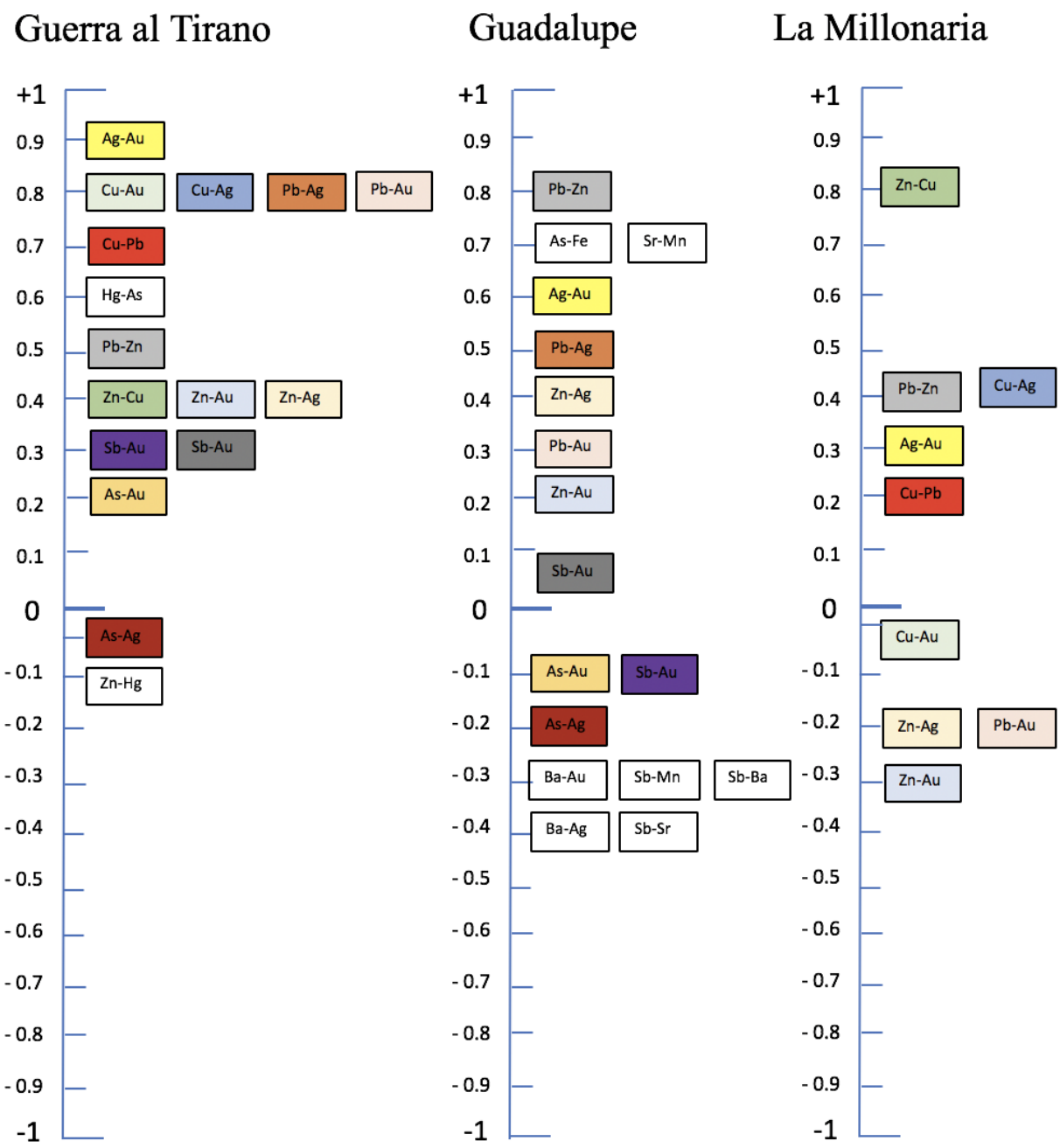

Figure 11: Color coding correlation coefficients listed in vertical from +1 to -1, for the three areas studied. Results are from Table 2A-C.

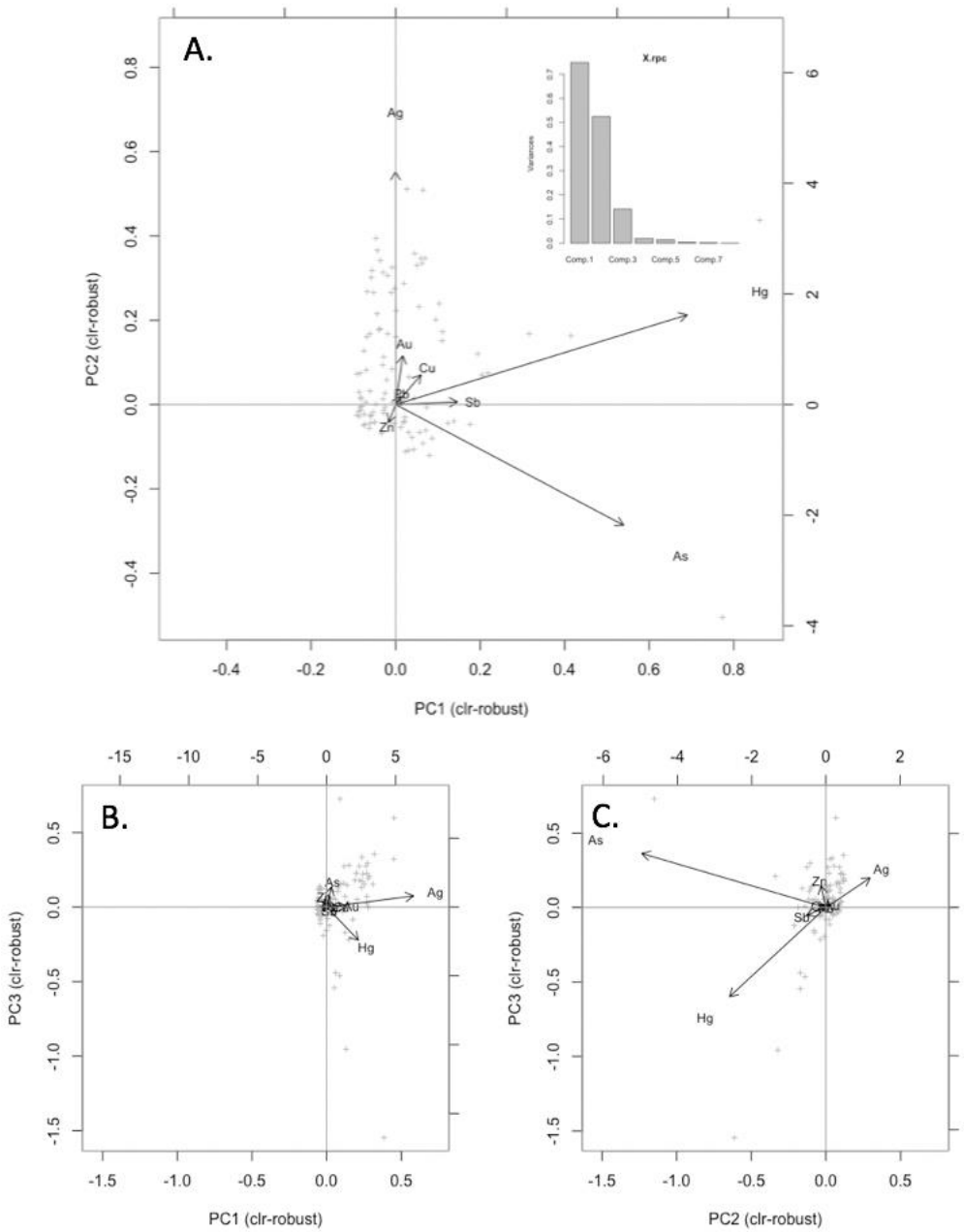

Figure 12A-C : Robust Principal Component Analysis (PCA) compositional biplots of centered-log ratio (clr) transformed data from the Guerr al Tirano deposit showing loading vectors (arrows) and scores (gray + signs) (Reimann et al., 2008).

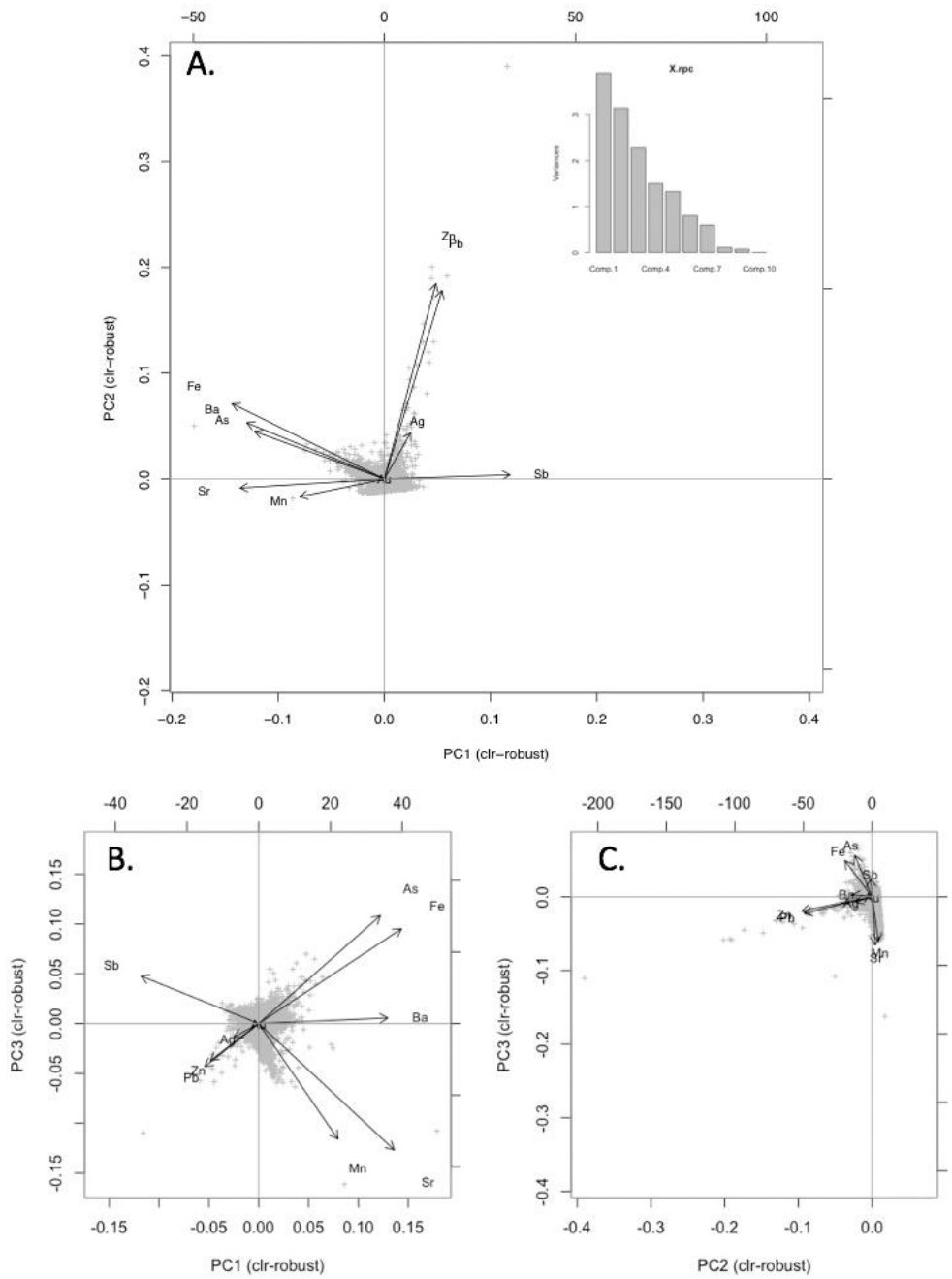

Figure 13. A-C: Robust Principal Component Analysis (PCA) compositional biplots of centered-log ratio (clr) transformed data from Guadalupe deposit showing loading vectors (arrows) and scores (gray + signs) (Reimann et al., 2008).

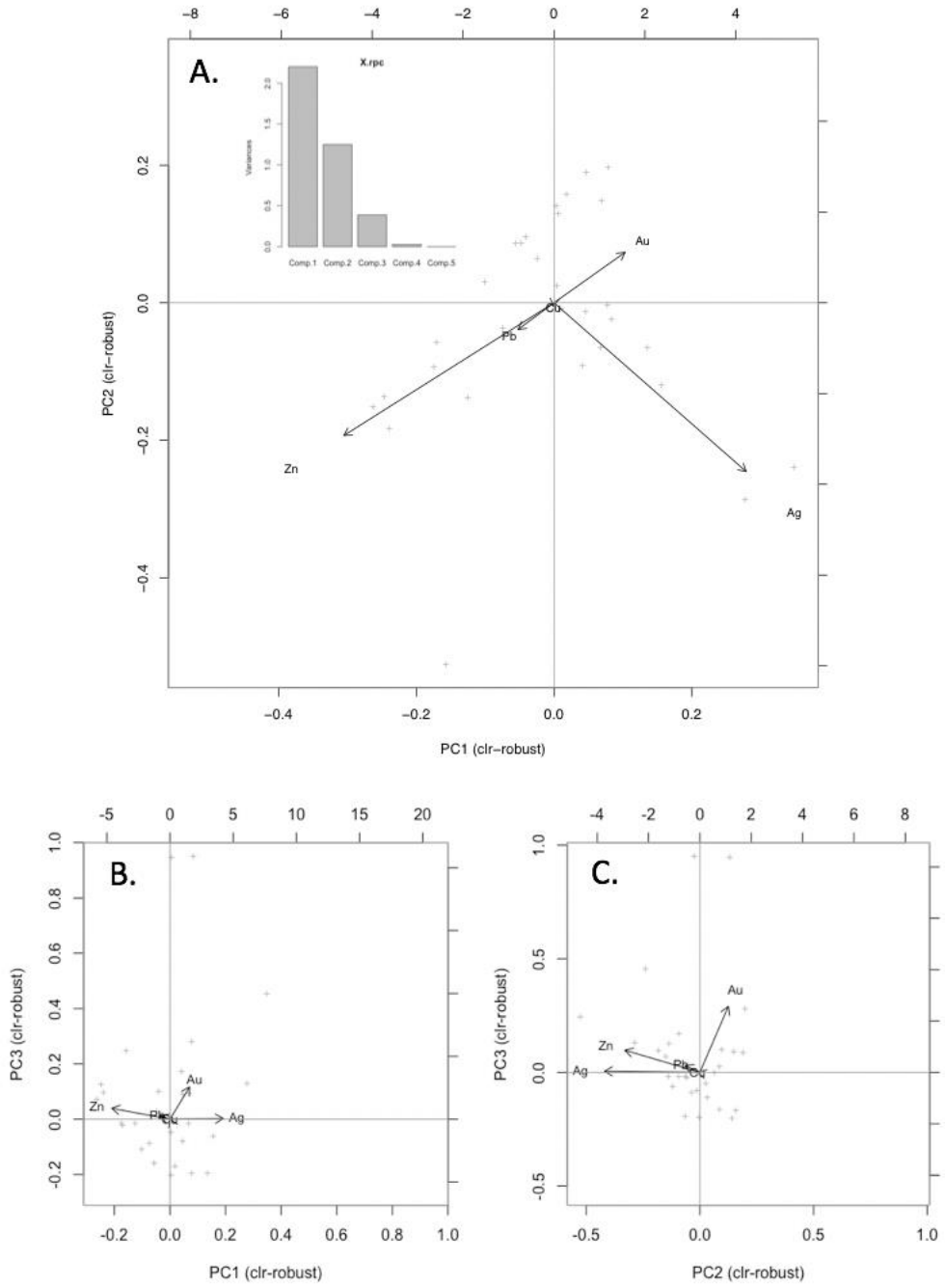

Figure 14. A-C: Robust Principal Component Analysis (PCA) compositional biplots of centered-log ratio (clr) transformed data from La Millonaria deposit showing loading vectors (arrows) and scores (gray + signs) (Reimann et al., 2008).

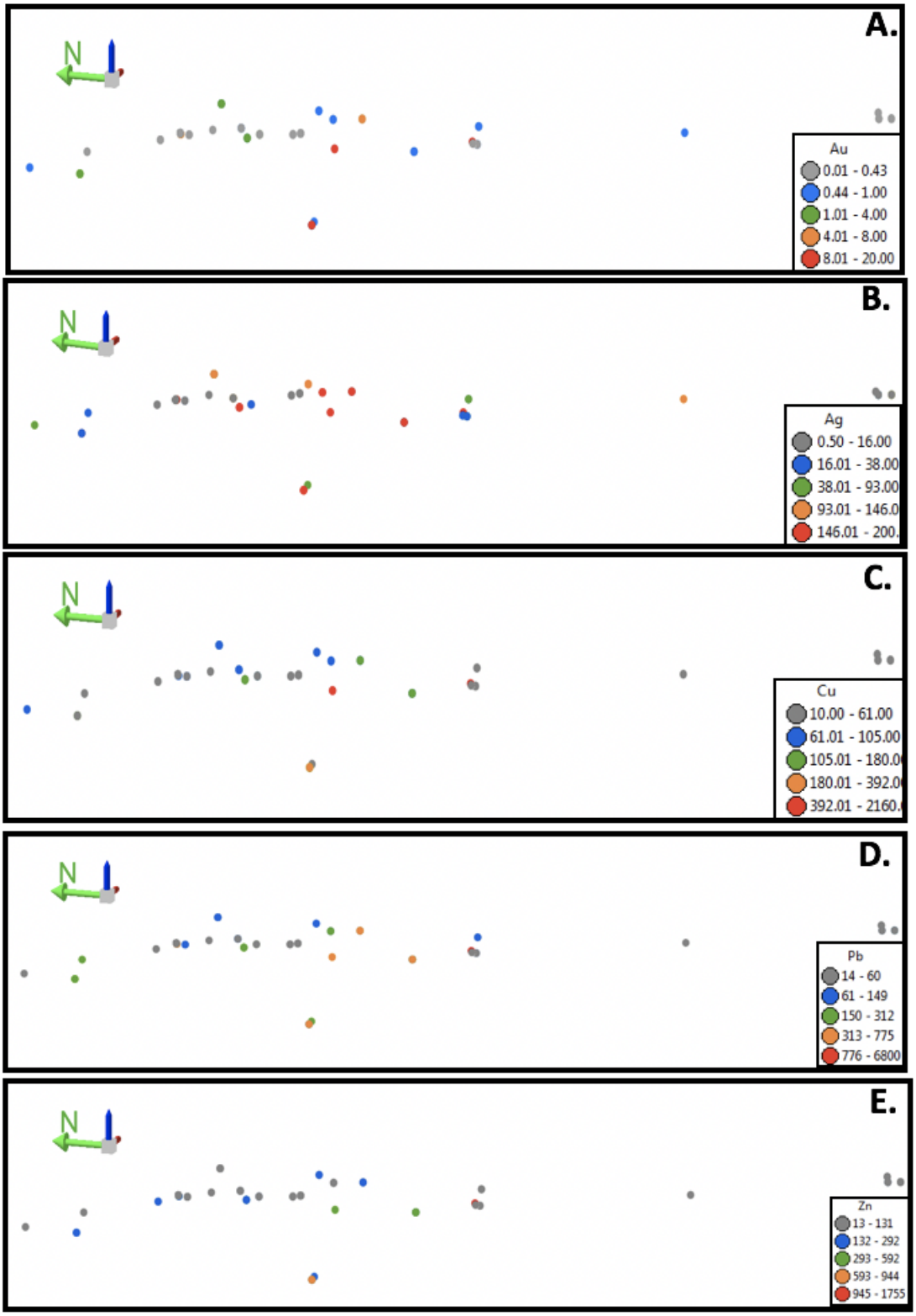

Figure15. A-E: 3 D modeling for Guerra al Tirano shows spatial distribution of Au, Ag, Cu, Pb and Zn.

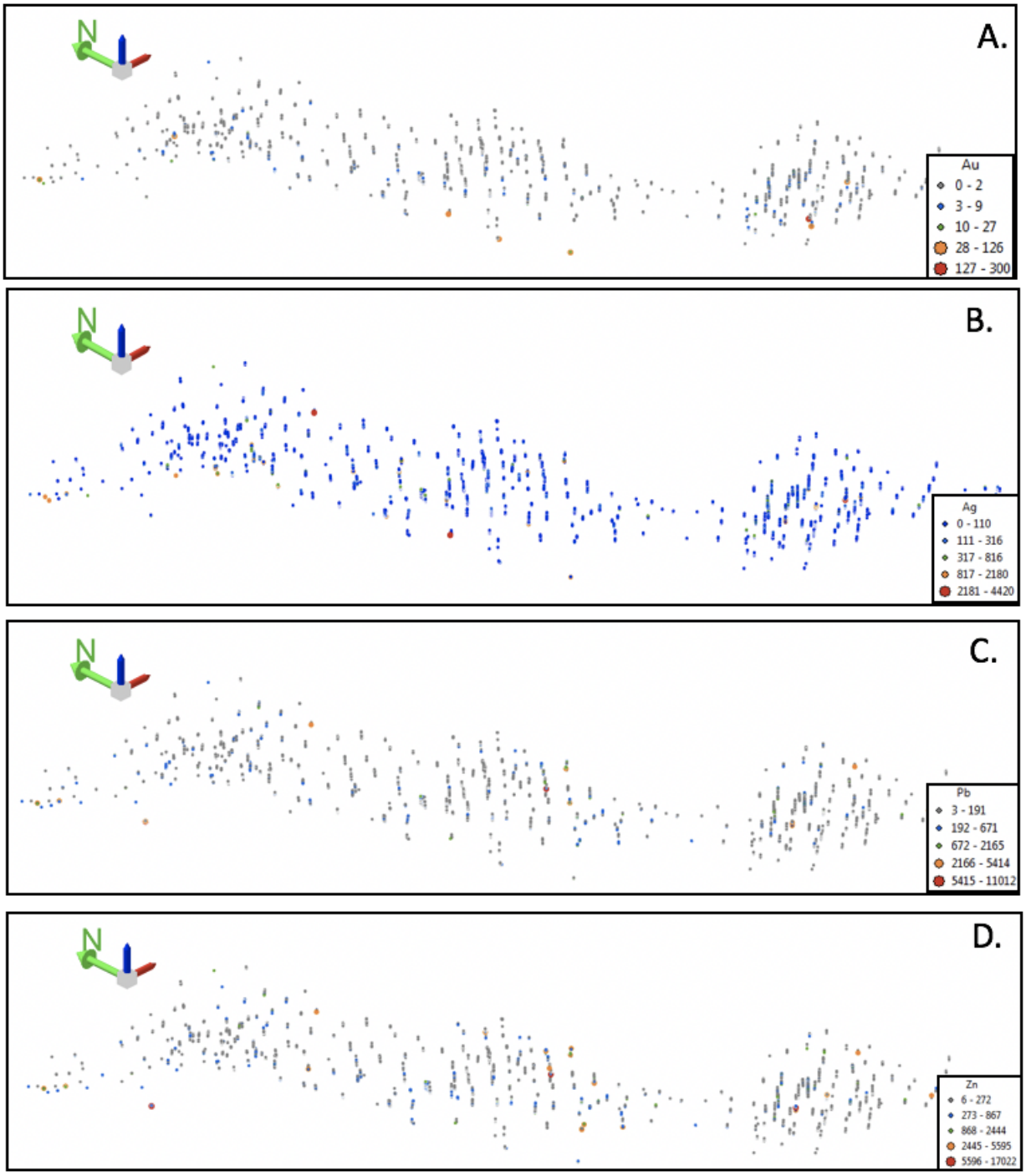

Figure16. A-D: 3 D modeling for Guadalupe shows spatial distribution Au, Ag, Pb, and Zn.

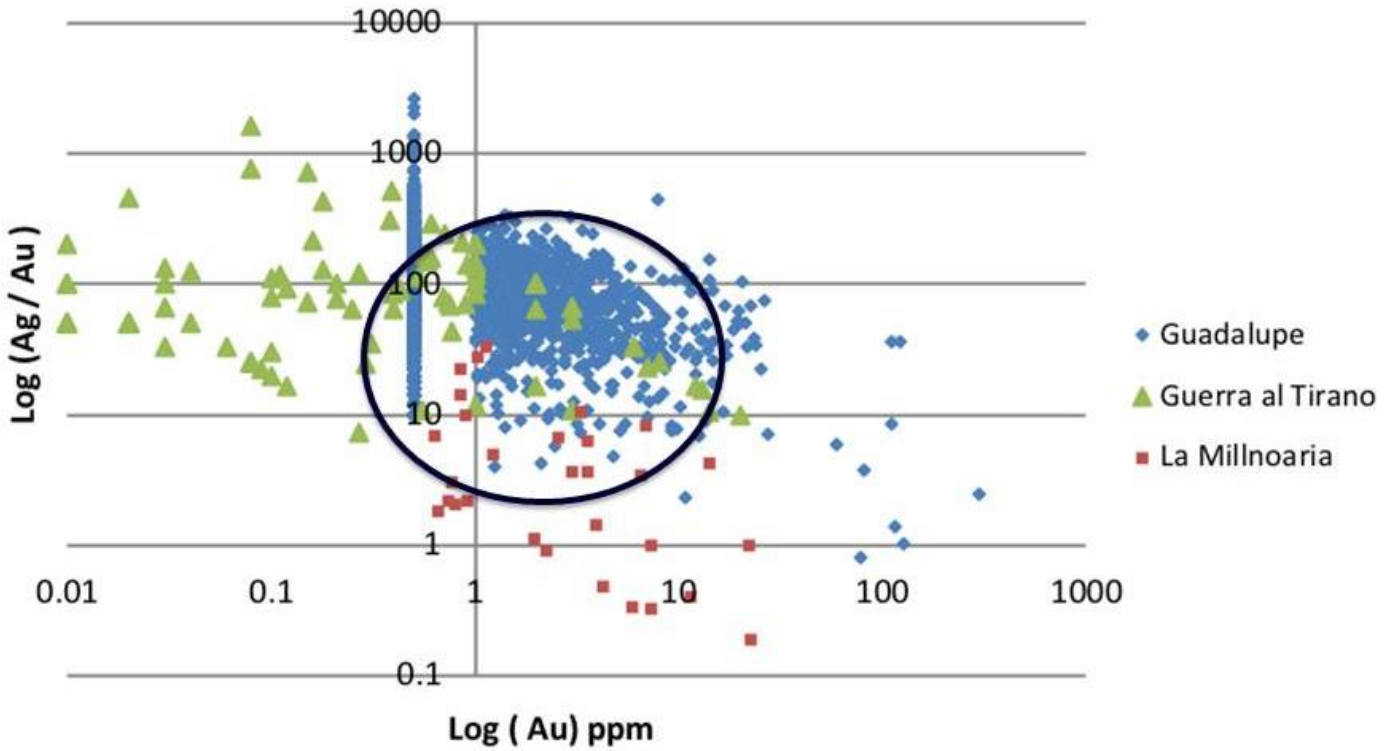

Figure 17: Scatter plots of Ag/Au with Au for the three regions (Guerra al Tirano, Guadalupe and La Millnoaria). The black circle shows that the data overlap.

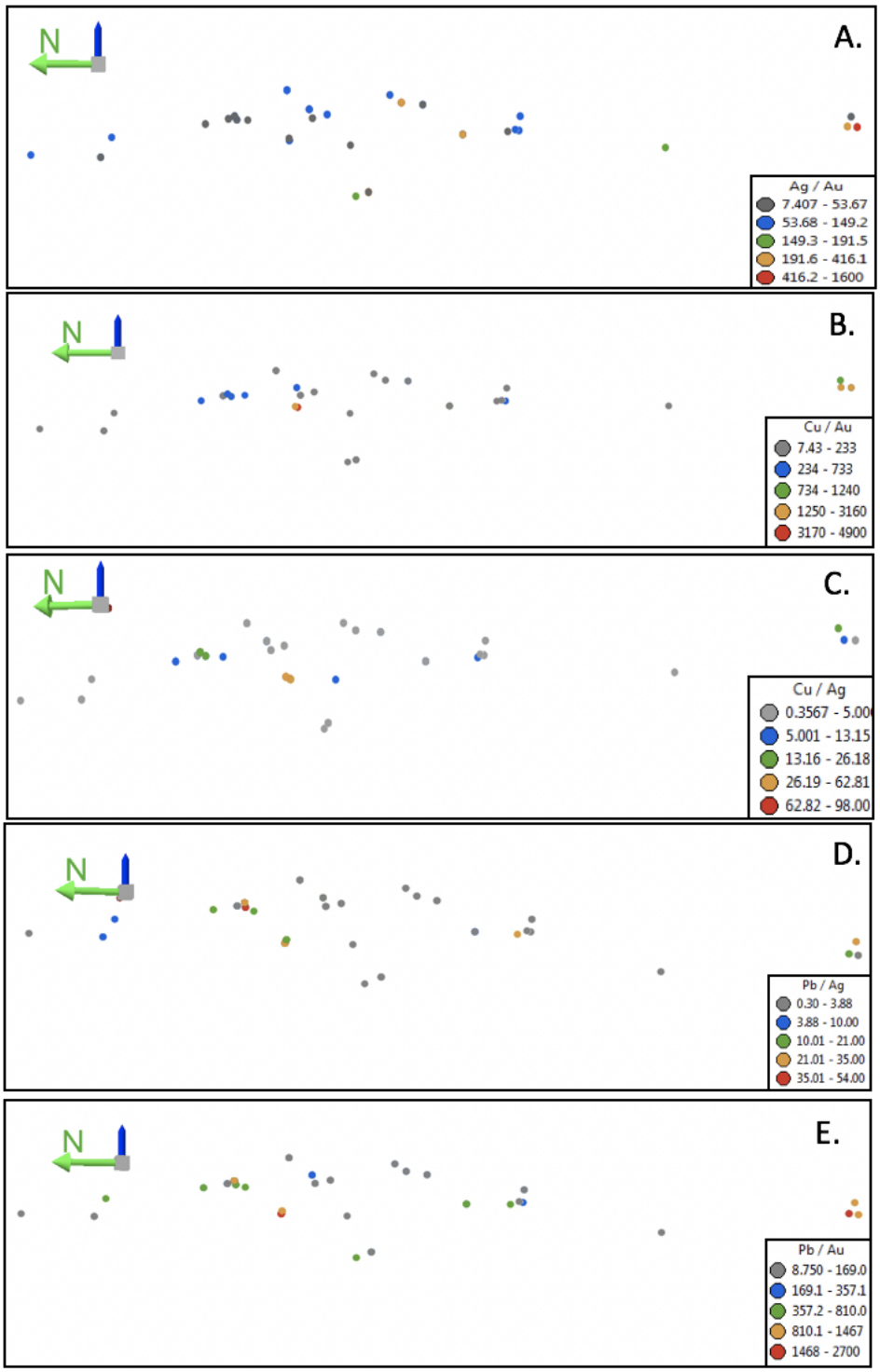

Figure 18A-E: 3 D modeling for Guerra al Tirano shows spatial distribution of Au/Ag, Cu/Au, Cu/Ag, Pb/Ag and Pb/Au.

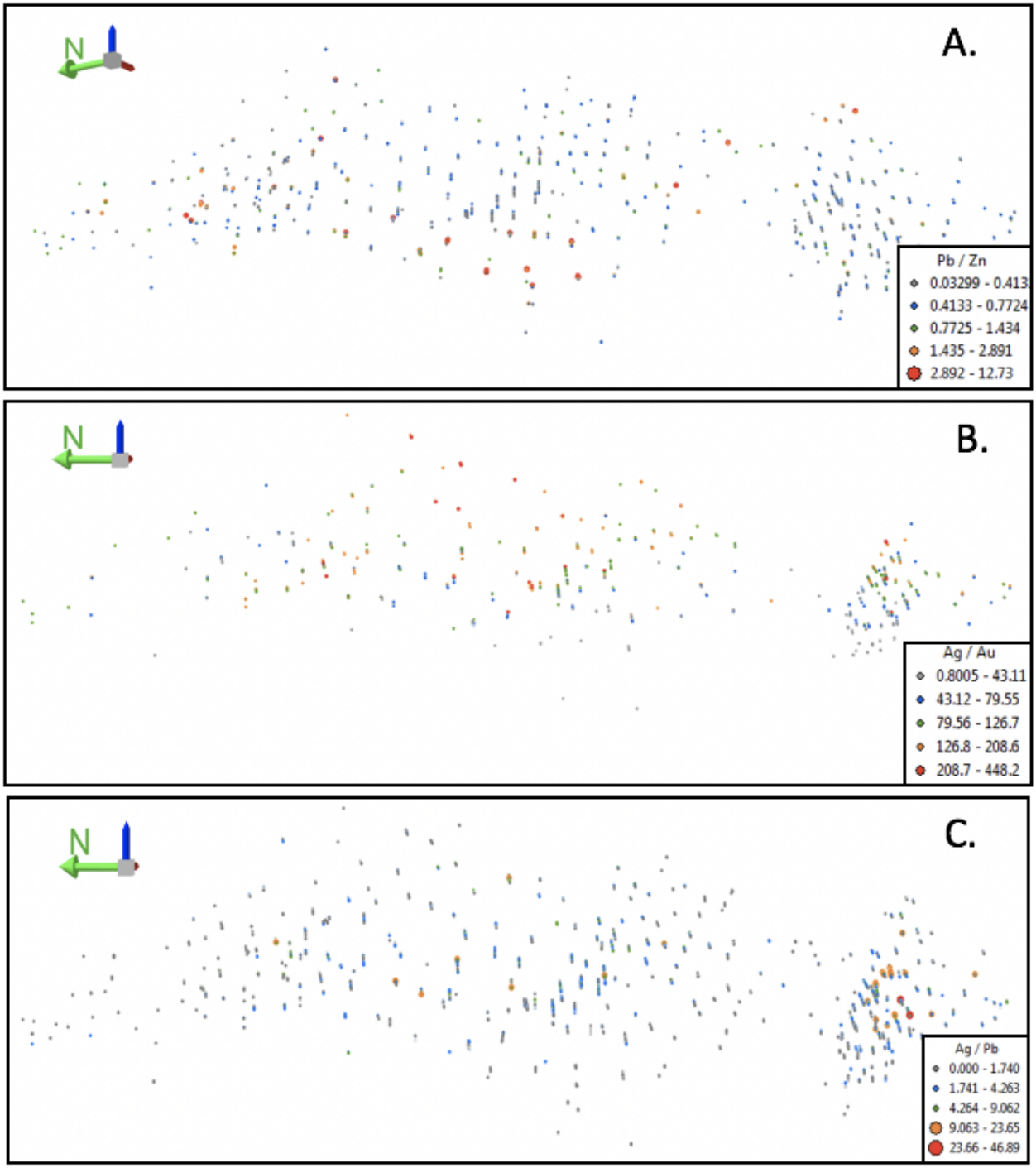

Figure 19A-C: 3 D modeling for Guadalupe shows spatial distribution for Pb/Zn, Ag/Au and Ag/Pb.

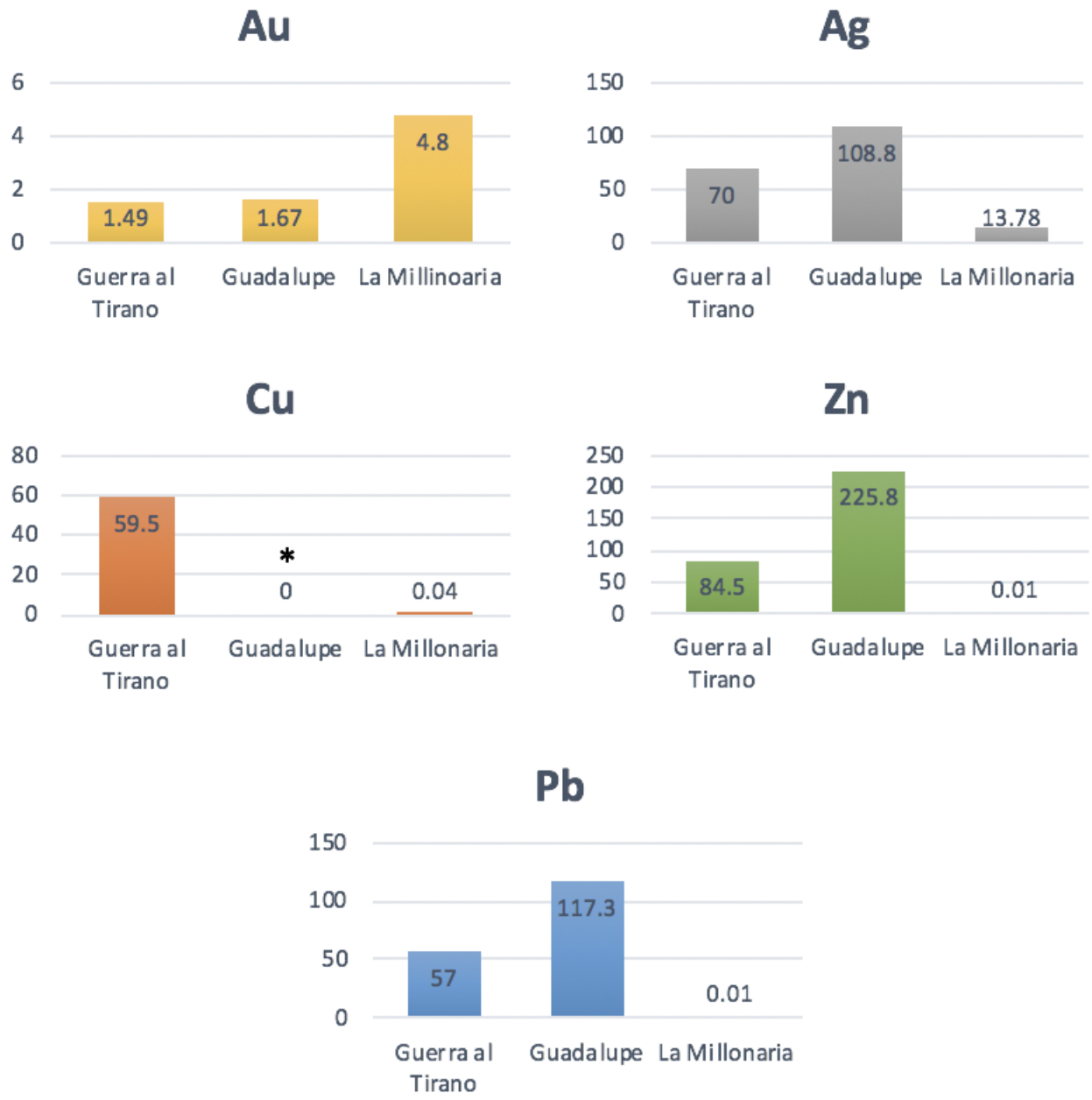

Figure 20: Magnitude metal concentration for the three different deposits. Y axis is the mean value for each deposit.* Cu is not analyzed in Guadalupe.

VITA

Labdan Nijr Alqahtani, was born in Riyadh city, Saudi Arabia. He earned his bachelor degree in Geology from the King Saud University; Riyadh in 2008. He attended the graduate school at the King Saud University and got his MS degree in Economic Geology in 2012. He used to work with Saudi Ceramics Company as a geologist from 2008 to 2010. Alqahtani had the privilege to teach courses on geology at high schools with Ministry of Education from 2010 to 2012.

Alqahtani got the opportunity to learn English language at the University of Alabama from 2013 to 2015. He joined the doctoral program in Geological Science in spring 2016 at The University of Texas at El Paso.

Alqahtani has presented his research at several conferences, including the 2018 Society of Economic Geology, the American Geological Union 2018 as well as two researches at Geological Society of America 2019.

While pursuing his degree, Alqahtani was the president and founder of the Saudi Student Association and the president of Society of Economic Geology at UTEP.

Contact Information: dr.labdan@gmail.com